

# Effects of residual stresses on the fatigue crack propagation of an orthotropic steel bridge deck

N.J.H. van den Berg





# Effects of residual stresses on the fatigue crack propagation of an orthotropic steel bridge deck

by

N.J.H. van den Berg

to obtain the degree of Master of Science  
at the Delft University of Technology,  
to be defended publicly on Friday May 15, 2020 at 10:00 AM.

Student number:	4616758	
Project duration:	July 5, 2019 – May 15, 2020	
Thesis committee:	Prof. M. Veljkovic,	TU Delft, Chairman
	Dr. H. Xin,	TU Delft
	Dr. P. C. J. Hoogenboom,	TU Delft
	MSEng O. Joostensz,	Rijkswaterstaat
	Ir. L. J. M. Houben,	TU Delft

An electronic version of this thesis is available at <http://repository.tudelft.nl/>.



# Preface

This thesis represents the conclusion of my educational career at Delft University of Technology. I started in Delft in 2016 on the pre-master programme for structural engineering. In December 2017, I started my master focussing on the track Steel, Timber and Composite structures. Looking back to my journey in Delft, it was a great experience becoming an engineer and obtaining a lot of knowledge about structural engineering.

Firstly, I would like to express my gratitude to Prof. M. Veljkovic for finding an interesting and challenging research topic. He has always supported me during the research project and motivated me to make improvements to the research. His door is always open to help and educate students.

Secondly, I would like to thank Dr. H. Xin for his guidance and support during my research project as daily supervisor. Especially for the help with the finite element modelling and the guidance in the research project.

Thirdly, my best regards to MsEng. O. Joostensz for giving support and practical advice to both my research project and case study of the Suurhoffbridge.

Fourthly, I would like to thank Dr. P.J.M. Hoogenboom for the helpful feedback on this thesis.

At last, I would like to thank my family for supporting the past 4 years during my study in Delft. Also, I would like to thank my girlfriend, Dian, for supporting and giving advice during my thesis.

*N.J.H. van den Berg  
Beek, May 2020*



# Summary

Orthotropic steel decks (OSDs) are susceptible to fatigue failure due to cyclic loading by heavy traffic passing the deck. These cyclic loads can cause fatigue cracks in the rib-to-deck joint. In and around the joint residual stresses are present due to the welding process. In this thesis, the effects of residual stresses on the fatigue crack propagation rate is evaluated. This research is based on finite element analysis and verified against experimental data. First, a thermomechanical weld simulation analysis is made in order to define and verify the residual stress field of the OSD-specimen. This analysis consists of two parts starting with a thermal model in which the temperature field during the welding process is analysed. This temperature field output is introduced into the mechanical model in which the residual stress field is modelled and verified. This data is subsequently used in a crack propagation model based on the extended finite element method (XFEM) in which the effect of the residual stresses on fatigue crack propagation is quantified. Next to that the residual stress component in each direction is analysed separately to obtain the effect of the residual stress per stress direction. The fatigue crack simulation including residual stress field shows good correlation ( $R^2 = 99\%$ ) compared to the experimental data. The simulation without residual stress field shows less correlation ( $R^2 = 95\%$ ), which shows that including the residual stresses improves the results significantly. Introducing only one residual stress component does not significantly improve the results compared to the model without the residual stresses. The effects of the residual stresses are relatively large as the tensile transversal residual stresses increase the crack propagation, while the tensile longitudinal residual stresses decrease the crack propagation rate.

In the case study the obtained knowledge from the research will be applied on the Suurhoffbridge of Rijkswaterstaat. On this highway bridge fatigue cracks occurred and these are measured using Time Of Flight Diffraction (TOFD) measurements. Firstly, the geometry and boundary conditions of FEM-model are verified using literature data based on hot-spot stresses. Secondly, the critical load position of the truck load is determined by obtaining influence lines based on the stress intensity factor. These lines show that critical position is reached when the wheel load is positioned between the webs of the stiffener. Also, from the influence lines can be concluded that the residual stresses in the transverse direction increase the stress intensity factors, while the influence of the residual stresses in longitudinal direction is negligible. At last, a fatigue crack propagation simulation with and without residual stresses is performed. The transversal tensile residual stresses are essential to initiate crack propagation, as at the weld root, compressive transversal stresses are present due to the traffic load which prevent crack propagation. Overall, the fatigue crack simulation including the transverse residual stresses corresponds relatively well compared to the measured data as the difference is approximately 14% also considering that two wheel load that have limited effect have been ignored in the analysis. If these two wheel loads would be included the results will improve. However, there are many assumptions made that can effect the result, such as the Paris law properties and load parameters. A slight change in these parameters would effect the results greatly. In order to verify the results, the assumptions made in the case study, should be verified using measurement data of the structure.



# Contents

List of Figures	ix
List of Tables	xiii
List of Abbreviations	xv
1 Introduction	1
1.1 Motivation for research . . . . .	1
1.2 Research questions . . . . .	2
1.3 Research structure . . . . .	2
2 Literature review	3
2.1 General information . . . . .	3
2.1.1 Fatigue cracks . . . . .	4
2.1.2 Crack phases . . . . .	5
2.2 Residual stresses . . . . .	5
2.2.1 Formation of residual stresses . . . . .	5
2.2.2 Welding process OSD . . . . .	6
2.2.3 Effects of residual stresses on the fatigue life . . . . .	7
2.3 Fracture mechanics . . . . .	7
2.3.1 Linear elastic fracture mechanics . . . . .	8
2.4 Abaqus crack propagation method . . . . .	9
3 Welding simulation analysis	15
3.1 Thermal model . . . . .	15
3.1.1 Geometry of the model . . . . .	15
3.1.2 Units . . . . .	16
3.1.3 Material properties . . . . .	17
3.1.4 Element activation . . . . .	17
3.1.5 Welding simulation . . . . .	17
3.1.6 Mesh . . . . .	21
3.1.7 Results . . . . .	21
3.2 Mechanical model . . . . .	22
3.2.1 Mechanical analysis . . . . .	22
3.2.2 Boundary conditions . . . . .	22
3.2.3 Mesh . . . . .	24
3.2.4 Stress discontinuations . . . . .	24
3.2.5 Results . . . . .	26
3.2.6 Verifying results . . . . .	28
3.2.7 Simplified residual stress field based on FEA . . . . .	34
4 Fatigue crack propagation simulation	37
4.1 Model properties . . . . .	37
4.1.1 Geometry of the model . . . . .	37
4.1.2 Loading model . . . . .	38
4.1.3 Boundary conditions . . . . .	39
4.1.4 Material Properties . . . . .	40
4.2 Comparison FE results with the static test data . . . . .	40
4.2.1 Deformation . . . . .	40
4.2.2 Strain comparison . . . . .	40
4.2.3 Hot spot stresses . . . . .	42

4.3	Parameter study. . . . .	42
4.3.1	Base model . . . . .	42
4.3.2	$C_3$ -parameter . . . . .	43
4.3.3	$C_4$ -parameter . . . . .	43
4.3.4	G-parameter . . . . .	43
4.3.5	Element type. . . . .	44
4.3.6	Element size . . . . .	44
4.4	Fatigue crack propagation simulation. . . . .	46
4.4.1	BC2-variant . . . . .	46
4.4.2	Mesh. . . . .	46
4.4.3	Residual stresses . . . . .	47
4.4.4	Results . . . . .	47
5	Case study Suurhoffbridge	53
5.1	Suurhoffbridge bridge description . . . . .	53
5.1.1	Fatigue problems . . . . .	55
5.1.2	Fatigue analysis procedure. . . . .	55
5.1.3	Material properties . . . . .	56
5.2	Hot-Spot Stress (HSS) analysis . . . . .	56
5.2.1	Load parameters. . . . .	57
5.2.2	Boundary conditions. . . . .	57
5.2.3	Results . . . . .	57
5.3	Analysis critical load position . . . . .	58
5.3.1	XFEM-model. . . . .	58
5.3.2	Load model . . . . .	58
5.3.3	Results . . . . .	59
5.4	Fatigue crack propagation simulation. . . . .	61
5.4.1	XFEM-model. . . . .	61
5.4.2	Load parameters. . . . .	61
5.4.3	Results . . . . .	62
5.5	Discussion . . . . .	64
6	Conclusions & Recommendations	67
6.1	Conclusions. . . . .	67
6.2	Recommendations . . . . .	68
	Bibliography	69
A	Appendix A - Subroutine DFlux	73
B	Appendix B - Sequence birth and death principle	75
C	Appendix C - transversal DLOAD-subroutine	77

# List of Figures

1.1	Crack through deck [12]	1
2.1	OSD example [12]	3
2.2	Wheel loading on OSD [36]	4
2.3	Rib-to-deck joint fatigue cracks [18]	4
2.4	Fatigue crack modes [32]	5
2.5	Fatigue crack phases [10]	5
2.6	Process of heating and cooling [23]	6
2.7	Distribution of residual stresses [30]	7
2.8	Effective stresses [22]	7
2.9	Fatigue crack growth [21]	9
2.10	Additional functions XFEM [45]	9
2.11	Normal and tangential coordinates additional functions XFEM [2]	10
2.12	Crack XFEM enriched nodes [43]	10
2.13	Crack propagation XFEM [33]	11
2.14	Amplitude direct cyclic loading	11
2.15	Fatigue Crack growth Paris law[9]	13
2.16	Procedure XFEM Abaqus [38]	13
3.1	Geometry OSD-specimen [25]	16
3.2	3D model OSD-specimen	16
3.3	Image weld [25]	16
3.4	Weld geometry in millimeters	16
3.5	Material properties [26]	18
3.6	Stress-strain diagram	19
3.7	Thermal process during welding	19
3.8	Heat source model [19]	20
3.9	Welding properties	20
3.10	Origin FEM-model	21
3.11	Rotated coordinate system	21
3.12	Overview mesh	21
3.13	Mesh detailed view	21
3.14	Weld experiment [25]	22
3.15	Heat model weld	22
3.16	Comparison between experiment[25] and FEM-model	22
3.17	Overview welding process boundary conditions [25]	23
3.18	Boundary conditions	23
3.19	Thermal expansion mechanical model	24
3.20	Overview mesh mechanical model	24
3.21	Cross-section mesh mechanical model	24
3.22	Stress discontinuities	25
3.23	Revised stress discontinuities	26
3.24	$\sigma_z$ along deck plate	27
3.25	$\sigma_z$ Right position outside	27
3.26	$\sigma_z$ right position inside and $\sigma_z$ left position outside	27
3.27	$\sigma_z$ left position inside	28
3.28	Principle of IHD measurement with tensile stress [25] (a) 3D-model with drill and SGR (b) cross-section before drilling (c) cross-section after drilling, stress/strain release	28

3.29 OSD-specimen residual stresses[25] (a) Location strain gauges (b) Close-up setup strain gauges (c) Overview strain gauges . . . . .	29
3.30 Comparison results weld deck plate [25] . . . . .	31
3.31 Comparison results weld toe deck and deck plate [25] . . . . .	32
3.32 Comparison results weld toe stiffener [25] . . . . .	33
3.33 Results Chapter 4 longitudinal stresses top deck[25] . . . . .	33
3.34 Comparison between FEA results and literature data [20] . . . . .	34
3.35 Simplified residual stress component S11 (x-direction) . . . . .	35
3.36 FEA residual stress component S11 (x-direction) . . . . .	35
3.37 Simplified residual stress component S22 (y-direction) . . . . .	35
3.38 FEA residual stress component S22 (y-direction) . . . . .	36
3.39 Simplified residual stress component S33 (z-direction) . . . . .	36
3.40 FEA residual stress component S33 (z-direction) . . . . .	36
4.1 Experiment set-up OSD-specimen [25] . . . . .	38
4.2 Loading condition OSD-specimen [25] . . . . .	38
4.3 Clamped support OSD-specimen[25] . . . . .	38
4.4 Pinned support OSD-specimen[25] . . . . .	38
4.5 Direct cyclic load . . . . .	39
4.6 Boundary condition variant 1 (BC1) . . . . .	40
4.7 Boundary condition variant 2 (BC2) . . . . .	40
4.8 Deformation . . . . .	41
4.9 Strain deck . . . . .	41
4.10 Strain stiffener . . . . .	41
4.11 Hot spot stress weld toe deck . . . . .	42
4.12 Hot spot stress weld toe stiffener . . . . .	42
4.13 Crack geometry parameter study . . . . .	43
4.14 Crack location parameter study . . . . .	43
4.15 Elements parameter study . . . . .	44
4.16 Parameter study $C_3$ and $C_4$ parameters . . . . .	44
4.17 Parameter study $G$ -parameter and element types . . . . .	45
4.18 Parametric study element size . . . . .	45
4.19 geometry initial crack . . . . .	46
4.20 Shape and position initial crack [25] . . . . .	46
4.21 Mesh fatigue crack simulation model [25] . . . . .	46
4.22 Initial crack depth Specimen 10 [25] . . . . .	47
4.23 Initial crack length Specimen 10 [25] . . . . .	47
4.24 Results fracture models crack depth . . . . .	48
4.25 Results fracture models crack width . . . . .	49
4.26 Comparison beachmark measurements and XFEM-results . . . . .	49
4.27 Results fracture models energy release rate mode K1 . . . . .	50
4.28 Results fracture models energy release rate mode K2 . . . . .	50
4.29 Results fracture models energy release rate mode K3 . . . . .	51
5.1 Overview Suurhoffbridge[24] . . . . .	53
5.2 Lay-out Suurhoffbridge[15] . . . . .	54
5.3 Cross-section (SV01 & SV02) Suurhoffbridge[15] . . . . .	54
5.4 Geometry Suurhoffbridge[15] . . . . .	54
5.5 Fatigue analysis Suurhoffbridge [15] . . . . .	55
5.6 Fatigue analysis procedure case study . . . . .	55
5.7 Hot Spot Stress (HSS) FEM-model . . . . .	56
5.8 Geometry HSS FEM-model Suurhoffbridge . . . . .	57
5.9 Cross-section results HSS-analysis (deformation scale 25x) . . . . .	57
5.10 Hot spot stress weld root . . . . .	58
5.11 Overview solid part XFEM-model . . . . .	58
5.12 Mesh solid part XFEM-model . . . . .	58

---

5.13 Loading scheme lorry number T1103 (type 4) NEN 8701 . . . . .	59
5.14 Transversal influence line fatigue crack mode 1 . . . . .	59
5.15 Longitudinal influence line fatigue crack mode 1 . . . . .	59
5.16 Maximum SIF transversal influence lines fatigue crack mode 1 . . . . .	60
5.17 SIF middle element transversal influence lines fatigue crack mode 1 . . . . .	60
5.18 SIF along crack surface FEA S11 crack mode 1 . . . . .	60
5.19 Wheel load position . . . . .	61
5.20 Direct cyclic wheel load . . . . .	61
5.21 Base FEA transversal stresses S11 (X-direction) . . . . .	62
5.22 Simplified residual stress component S11 . . . . .	62
5.23 Simplified residual stress component S33 . . . . .	62
5.24 Results FEA S11 transverse stress field . . . . .	63
5.25 Results FEA S11 crack phases . . . . .	63
5.26 Results fatigue crack simulation FEA S11 crack length 2C . . . . .	64
5.27 FEA crack propagation residual stress components S11 & S33 . . . . .	64
5.28 FEA residual stresses (X-direction) . . . . .	64



# List of Tables

3.1	Units heat input model . . . . .	17
3.2	parametric study boundary conditions . . . . .	23
4.1	Load and Paris law parameters [4, 25] . . . . .	40
4.2	Paris Law parameters . . . . .	43
4.3	Average percentage differences between experiments and FEA crack height . . . . .	52
4.4	Squared correlation between experiments and FEA crack height . . . . .	52
5.1	Load and Paris law parameters case study [4, 25] . . . . .	56



# List of Abbreviations

<b>BC</b>	Boundary Conditions
<b>C.T.C.</b>	Center-To-Center
<b>FE</b>	Finite Element
<b>FEM</b>	Finite Element Model
<b>HAZ</b>	Heat Affected Zone
<b>HSS</b>	Hot Spot Stresses
<b>IHD</b>	Incremental Hole Drilling
<b>LEFM</b>	Linear Elastic Fracture Mechanics
<b>OSD</b>	Orthotropic steel deck
<b>RWS</b>	Rijkswaterstaat
<b>SAW</b>	Submerged Arc Welding
<b>SGR</b>	Strain Gauge Rosette
<b>SIF</b>	Stress Intensity Factor
<b>TOFD</b>	Time Of Flight Diffraction
<b>VCCT</b>	Virtual Crack Closure Technique
<b>XFEM</b>	eXtended Finite Element Analysis



# Introduction

## 1.1. Motivation for research

In the 1960s and 1970s the amount of traffic in the Netherlands increased [31], resulting in a lot of bridges being constructed. During the lifetime of these bridges the maximum weight of the heavy trucks has been increased from 30 tons, in the '60s, to 50 tons nowadays [31]. Highways have the highest number of passes of this heavy traffic due to the high traffic intensity. This heavier traffic mainly causes fatigue problems for steel bridges with highways on top of them.

Many steel bridges use orthotropic steel decks (OSDs) as deck construction. These decks mostly consist of a stiffened deck plate that is supported by main girders. At a certain interval cross-girders are positioned in order to ensure that the bridge has enough torsional rigidity. All the different members are welded together to one integral deck. With this type of construction, a lightweight deck construction can be realised. These lightweight bridges are often used in long span highway bridges. Nowadays the weakest link in these constructions are the welded connections. The orthotropic deck can resist high loads, and thus heavy traffic, due to the low self-weight. However the stress range of the traffic passing the bridge is relatively high due to the low self weight. The increase in load, due to the heavier traffic, causes higher stress ranges within the structure of the bridge. Although the bridge can easily cope with the increase in stress the cyclic loading of the heavy traffic can cause fatigue cracks in certain joints of the deck. The rib-to-deck joint, which is the focus of this MSc-thesis, is susceptible for fatigue cracks around the weld region. These cracks are shown in Figure 1.1.

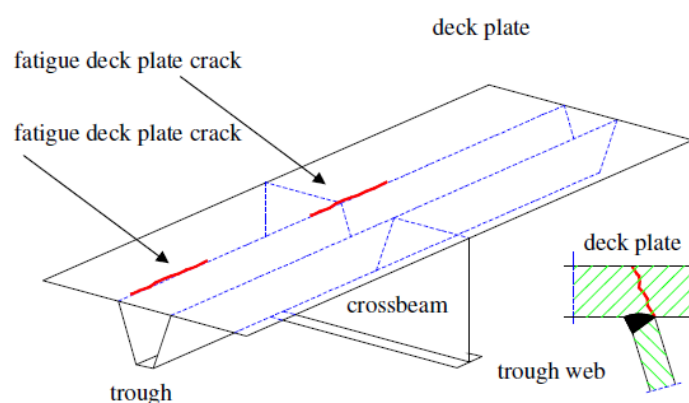


Figure 1.1: Crack through deck [12]

During the manufacturing of these welds residual stresses and distortions are induced in the joint. Residual stresses are caused due to thermal expansion by the heat initiation of the welding process. These residual stresses can influence the fatigue life of a structure as these stresses are primarily in tension around the weld zone of the rib-to-deck joint [34].

## 1.2. Research questions

Research around the prediction of residual stress of an orthotropic plate due to welding is performed in a previous MSc-thesis of K. Spyridoni [34]. These residual stresses can influence the crack propagation through the rib-to-deck joint. In the MSc-thesis of R. Shankar Gupta [15], the rate of crack propagation of a rib-to-deck joint has been analysed using eXtended Finite Element Method (XFEM) in Abaqus®. The XFEM model uses Linear Elastic Fracture Mechanics (LEFM) and Virtual Crack Closure Technique (VCCT) to determine the crack propagation. The residual stresses were not taken into consideration in the research of R. Shankar Gupta. In this MSc-thesis the residual stresses due to the welding will be incorporated in the XFEM model. The crack propagation will result in a number of cycles which can represent a fatigue life of the joint. This leads to the following research question:

### **What is the effect of residual stresses on the crack propagation of a rib-to-deck joint using XFEM?**

The research question is answered using the following sub questions:

1. How can the residual stress field of the OSD-specimen be determined?
2. How can the residual stresses be implemented in an extended finite element model?
3. What is the effect of the residual stresses on the crack propagation using XFEM?
4. How can the effect of the residual stresses be quantified?
5. How can the results of the XFEM analysis be implemented in a case study?

## 1.3. Research structure

In order to keep the thesis organised the thesis is divided into six chapters. The structure of the thesis is described below.

In chapter 2, a literature review is presented. This literature review holds the fundamental theory that is applied in the research. The chapter starts with some general information about orthotropic steel decks and the fatigue problems on the connections of these type of structures. It continues with fundamental information about residual stresses concerning welded connections. At last, the theory about the fracture mechanics applied in the research will be elaborated.

In chapter 3, the welding simulation model is described. This chapter consist of two parts. In the first part the thermal analysis model will be described. In the second part a mechanical analysis is performed. In this analysis the residual stresses will be defined using the temperature data field obtained by the thermal analysis. These residual stresses will be used in Chapter 4.

In chapter 4, the fatigue crack simulation is described. In this chapter a crack propagation analysis is performed with and without residual stresses. This will be done in order to obtain the effect of the residual stresses on the crack propagation. The results of the model will be compared with experimental data from literature.

In chapter 5, the case study will be presented. The knowledge gained from the research in the previous chapters will be applied to a greater scale. In this case study the methodology of the research will be compared to an existing structure.

At last, chapter 6 presents the conclusions of the total work and recommendations for further research.

# 2

## Literature review

This chapter can be divided into four parts. In section 2.1, general information about orthotropic steel decks (OSDs) and fatigue is given. In section 2.2, the influence of residual stresses will be elaborated. In section 2.3, all the necessary information of linear elastic fracture mechanics will be described. At last, the technical background of the XFEM package in Abaqus® will be elaborated in section 2.4.

### 2.1. General information

Orthotropic steel decks (OSDs) are one of the most common deck systems in steel bridges construction. An orthotropic steel deck mostly consist of a stiffened deck plate that is supported by main girders. At a certain interval, cross-girders are positioned in order to ensure that the bridge has enough torsional rigidity. In most OSDs, closed stiffeners are used for their torsional rigidity, which leads to an increase in transversal stiffness of the OSD. Although these stiffeners are more difficult to manufacture and maintain compared to open stiffeners the structural benefits outweigh the practical disadvantages. All the different members are welded together to one integral deck. With this type of construction a lightweight deck construction can be realized. An example of an OSD is shown in Figure 2.1.

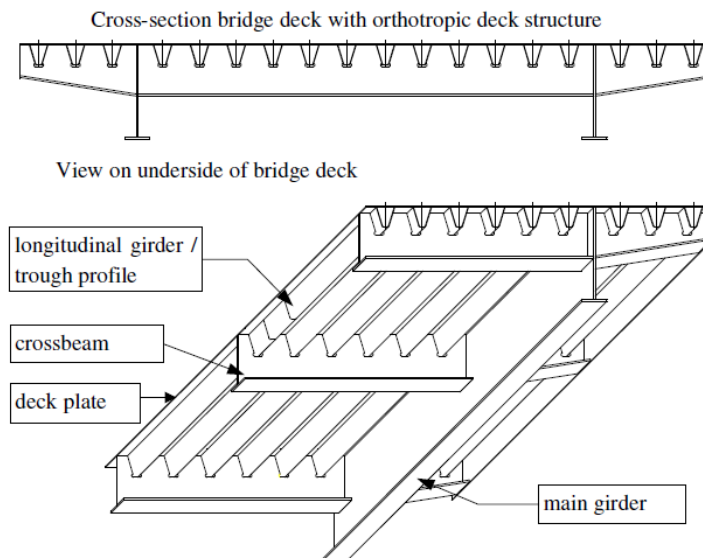


Figure 2.1: OSD example [12]

The orthotropic deck is often loaded with heavy traffic load in the form of trucks. The localized loads of the wheels cause local deformations of the deck. When a wheel load passes the bridge deck between two stiffeners or in the middle of the stiffener, the deck will deform locally and causes high stresses on the

connection between the deck and the stiffener. The localized stresses of the wheel loads can cause fatigue issues in the structure. The loading of the deck plate is shown in Figure 2.2.

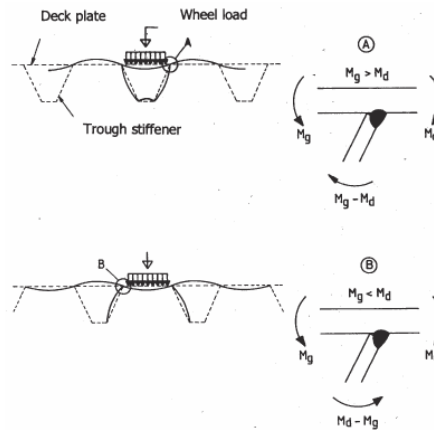


Figure 2.2: Wheel loading on OSD [36]

### 2.1.1. Fatigue cracks

On a bridge the load of heavy traffic is not always present. The structure is loaded in a cyclic manner as many heavy trucks pass the bridge during the use of the bridge. In fatigue engineering a pass of a truck wheel corresponds to a load cycle as a part of the structure is loaded and unloaded once. These cyclic loads can cause fatigue problems on OSDs although these stresses are well below the yield stress of the material. Eventually this cyclic loading can cause the material to fail, which ultimately leads to failure of the structure after a number of load cycles.

The change in stress during the load cycle is called the stress range. The magnitude of these stress ranges is one of the most important factors in determining the fatigue life of the structure. The combination of the magnitude and the number of cycles per stress range can determine the damage of the loading on the structure using S/N-curves described in the Eurocode [28]. If the cumulative damage of each stress range with the corresponding number cycles is higher than 1, the structure is considered failed according to the Eurocode [28].

Fatigue cracks can occur when OSDs are exposed to cyclic loads in the form of passing heavy traffic. The localised stresses due to the cyclic wheel loads of heavy traffic can cause fatigue cracks in the welded connections of the OSD. The cracks are often initiated at the welds, which often have weld imperfections that can initiate fatigue cracks in the different joints of the OSD. At these joints, stress concentrations are present due to the change in geometry and weld imperfections. These increased stresses can both initiate and accelerate the growth of a fatigue crack.

In this thesis, only the rib-to-deck joint will be considered. The possible crack locations within this joint are represented in Figure 2.3. In this research the toe-deck crack and the root-deck crack will be considered. The root-deck joint is particularly difficult to detect as this crack occurs within the stiffener. Also these cracks can propagate due to different stresses in any direction in three distinct fracture modes: crack opening, in-plane shear and out-of-plane shear, shown in Figure 2.4.

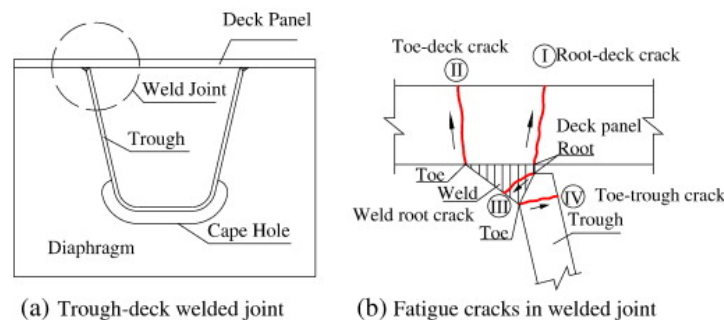


Figure 2.3: Rib-to-deck joint fatigue cracks [18]

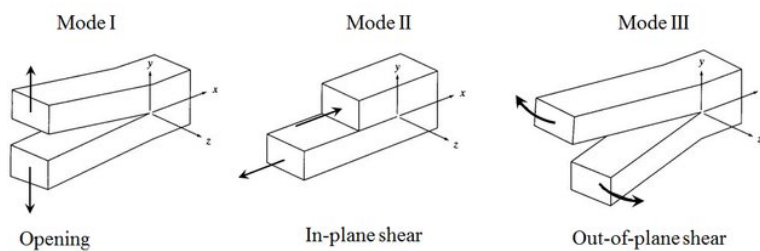


Figure 2.4: Fatigue crack modes [32]

### 2.1.2. Crack phases

The fatigue life of OSDs can be described in two phases namely fatigue crack initiation and fatigue crack propagation [44]. This thesis will focus on the crack propagation of a fatigue crack of a rib-to-deck joint. The crack propagation phase is followed by final failure of the structure. The three phases are shown in Figure 2.5.

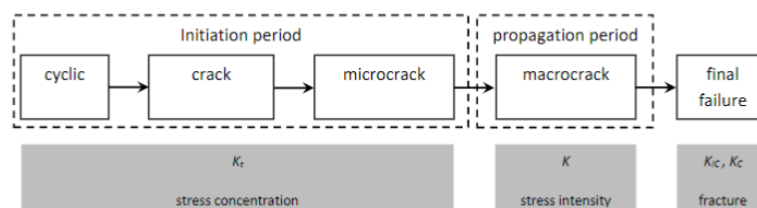


Figure 2.5: Fatigue crack phases [10]

In welded connections crack initiation often occurs due to welding defects and tensile residual stresses. Defects that occur during the manufacturing of the welds such as lack of penetration/fusion, slag inclusion, gas holes, overlap or excess of weld material. Next to that the quality of the workmanship can influence the fatigue life of the joint. There are several weld improving methods like peening, grinding or coining. These methods reduce the stress concentration around the weld and reduce the effect of tensile residual stresses. These microcracks often start at a size of a grain [15].

However compared to the crack propagation phase the crack initiation phase is relatively short due to the weld defects. In modelling this phase might be neglected, as it can be assumed that initial defects are already present [15]. For non-weld connections the crack initiation phase is much longer, due to the lack of those imperfections.

In the crack propagation state the macrocrack will propagate through the material. In this crack phase the stress intensity factor, denoted as  $K$ , is used to determine the crack propagation. The research in this thesis will be mostly focused on this phase.

At final failure the fracture toughness, denoted as  $K_{C_c}$ , can be used to determine the critical crack length at which a specimen fails.

## 2.2. Residual stresses

During the manufacturing process of steel often residual stresses are introduced into the material. In welding, these stresses occur due to the thermal gradient within the specimen generated during the weld process [35, 41]. First the specimen is heated, due to the weld arc, and the filler material is added to the specimen in order to connect the deck plate and the stiffener. During the heating phase the material acts almost like a liquid as the stiffness of the material is very low at these elevated temperatures. Next, the filler material and the material surrounding the weld cools down. During this cooling phase the material shrinks, however as the material stiffens it cannot deform freely. Due to these restrained shrinkage tensile residual stresses occur in the weld region. These tensile residual stresses are compensated compressive residual stresses in the surrounding material.

### 2.2.1. Formation of residual stresses

As mentioned in the previous paragraph, the residual stresses are formed during the manufacturing process of the component. There can be different reasons behind the occurrence of residual stresses during manu-

facturing. According to Withers [40] there are three main causes behind the occurrence of residual stresses during manufacturing:

1. Plastic deformation

The permanent deformation of a component induce residual stresses when the component is deformed beyond the elastic limit of the ductile material. In practical applications these stresses exist at the corners of cold formed steel sections. At these corners the material has been deformed beyond the elastic limit in such way that the material is permanently deformed.

2. Phase transformation

Rapid changes of the crystal lattice structure of the material can induce distortions to nearby regions which can induce residual stresses [40].

3. Thermal gradient

This cause of residual stresses can be found in welded connections, as the welding process involves heating the welding material and rapid cooling of the material. During the welding process the welding material heats up and expands, after the welding material is positioned the material cools. In the process during the temperature rise, the material expands, while during cooling the material shrinks. This heating and shrinking of the material does not induce residual stresses. Only when the deformation of the material is restricted, residual stresses occur. In the following section this phenomena will be described when welding a rib-to-deck joint.

### 2.2.2. Welding process OSD

During the welding process the material is heated which causes the material to expand. When the weld material is placed on its position the material cools down and will shrink. Only when the deformation of the material is restricted do residual stresses occur. During the welding process some elements are heated more than others. Most of the time the heated elements are restricted by the less-heated elements. This restrained deformation results in compressive stresses of these heated elements. When the heat source is removed the heated elements cools down and shrinks at the same time. During this cooling phase the deformation is restrained by the surrounding material. This restrained deformation will result in longitudinal tensile stresses that can be up to the yield stress for mild steel [30]. This distribution of stress will be present in the material when the structure is in use. Around the welded material compressive residual stresses occur to compensate for the tensile residual stresses. The process of heating and cooling is shown in Figure 2.6 and the distribution of residual stresses is shown in Figure 2.7.

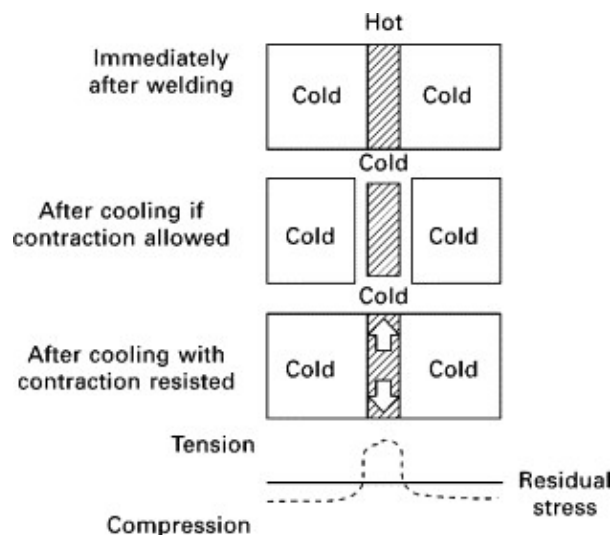


Figure 2.6: Process of heating and cooling [23]

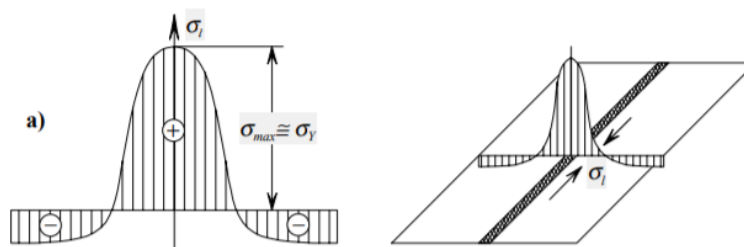


Figure 2.7: Distribution of residual stresses [30]

### 2.2.3. Effects of residual stresses on the fatigue life

As described in section 2.1.1, fatigue cracks in OSDs can be a problem when these are subjected to cyclic loading. Nowadays the stresses within the cross-section caused by heavy traffic can be accurately obtained with numerical models. However, it is more difficult to obtain the residual stress field around a welded joint. The additional residual stresses can have a negative influence when determining the fatigue life.

The cyclic loading by heavy traffic can cause fatigue problems with OSDs. The cyclic loading can cause crack propagation of microcracks within the structure. Often these cracks are present around welded connection between the deck and the stiffener of the OSD. During the welding process initial imperfections are introduced in the weld area. Due to the imperfections, microcracks around the weld area can grow to fatigue cracks that can cause the connection to fail. The residual stresses in the weld area influence the crack propagation of these microcracks caused by the initial imperfections.

The residual stresses can either accelerate or decelerate the crack growth as the stress caused by the cyclic loading will be the same. Compressive residual stresses can increase the fatigue life by reducing the crack propagation rate, while tensile stresses are unfavourable in terms of fatigue life as these stresses increase the crack propagation rate [6, 39]. However, in the case of orthotropic steel decks, cracks have been observed in regions where the stress field due to external loads is normally in compression. These compressive stresses should prevent crack propagation as the compressive stress closes the crack. Therefore, in cases where residual stresses were excluded from numerical models of OSDs under cyclic loading, fatigue life may be overestimated [11]. The effective stress of both the residual and live stresses is most important when calculating the fatigue life of the structure. The influence of tensile residual stresses is shown in Figure 2.8. Therefore the influence of the residual stresses on the crack propagation of microcracks can not be underestimated as the results are greatly dependant on the combination of external stresses and residual stresses.

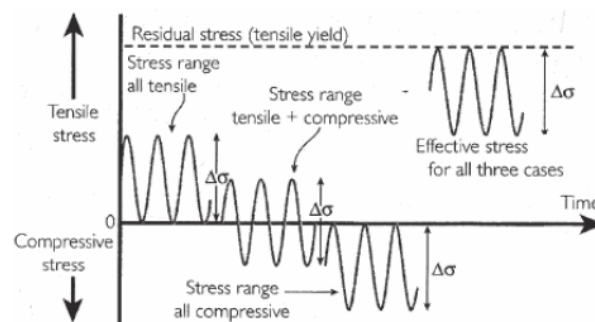


Figure 2.8: Effective stresses [22]

## 2.3. Fracture mechanics

A study towards fracture mechanics will be the main part of this research. LEFM will be used to predict the crack propagation through the specimen. The LEFM method will be described in section 2.3.1. The crack propagation will be modelled using eXtended Finite Element Method (XFEM) with Abaqus®, which uses LEFM and virtual crack closure technique (VCCT) to model the crack propagation in the model.

### 2.3.1. Linear elastic fracture mechanics

In this section the Linear Elastic Fracture Mechanics (LEFM) used for the crack propagation in XFEM will be described. At the end of this section the justification for using this method is described.

LEFM started in 1921 with Griffith criterion [14]. Griffith criterion states that crack propagation of a crack with a length  $\Delta a$  in a plate with a certain thickness  $t$  is only possible: "if the work done by the applied force is more than or equal to the summation of the change in the elastic energy and the energy absorbed at the crack tip, then it will lead to unstable fracture" [16]. Equation 2.1 coincides with the previous statement:

$$\delta W \geq \delta U^{el} + G_c t \delta a \quad (2.1)$$

Where the  $\delta W$  is the work done by the crack propagation, the  $\delta U^{el}$  is the change in elastic energy and  $G_c$  is the critical energy release rate. The  $G_c$  is a material factor that represents how easily the material cracks. A very brittle material has a low  $G_c$ , while a very tough material has a very high  $G_c$ . The unit of the critical energy release rate is energy per area [ $\frac{J}{m^2}$ ]. There is a relation between the critical energy release rate and the critical stress. This relation is represented by equations 2.2 and 2.3.

$$\sigma_c \sqrt{\pi a} = \sqrt{E G_c} = K_{IC} \quad (2.2)$$

Where  $K_{IC}$  is the fracture toughness. The first formula is related to the formula for the Stress Intensity Factor (SIF)  $K = \sigma \sqrt{\pi a}$  [ $MPa\sqrt{m}$ ].

$$G_c = \frac{\sigma_c^2 \pi a}{E} \quad (2.3)$$

Later Irwin [17] proposed a solution, shown in the equation 2.4, that relates the Potential Energy  $P$  with the crack growth  $da$ .

$$G = -\frac{dP}{da} \quad (2.4)$$

Using equations 2.2, 2.3 and 2.4 an important relation within the LEFM can be derived. The change in potential energy  $P$  is considered to act on closing a small part of the crack, equating this energy to the work necessary to close the crack segment without any external work variation [16]. Equation 2.5 is obtained for plain stress and equation 2.6 for plain strain.

$$G = \frac{1}{E} (K_I^2 + K_{II}^2) + \frac{1+\nu}{E} K_{III}^2 \quad (2.5)$$

$$G = \frac{1-\nu^2}{E} (K_I^2 + K_{II}^2) + \frac{1+\nu}{E} K_{III}^2 \quad (2.6)$$

In this research, the crack propagation phase is of most importance as the initiation phase is relatively short. Paris and Erdogan [29] have been studying the fatigue crack growth in many experiments. They have found a Log-Log relation between the range of Stress Intensity  $\Delta K$  and the crack growth rate  $\frac{da}{dN}$ . After more experiments they also found two asymptotes on either side of the  $\frac{da}{dN} - \Delta K$ -relation. The  $\frac{da}{dN} - \Delta K$ -relation is shown in Figure 2.9. The left region of the graph is called the threshold region, denoted by  $\Delta K_{\text{threshold}}$ . Below this level no crack growth will exist. While the right asymptote, denoted by  $\Delta K_{IC}$  is the point at which the crack will propagate so fast that it will lead to failure. In the middle region also called the "Paris region" the crack growth is linear and stable crack growth occurs. This region can be represented by equation 2.7. Where  $C$  and  $m$  are both dependant on the material properties of the specimen. The research described in this thesis will be focussed on the 'Paris region' as this phase is the dominant phase in fatigue cracks occurring in OSDs.

$$\frac{da}{dN} = C \Delta K^m \quad (2.7)$$

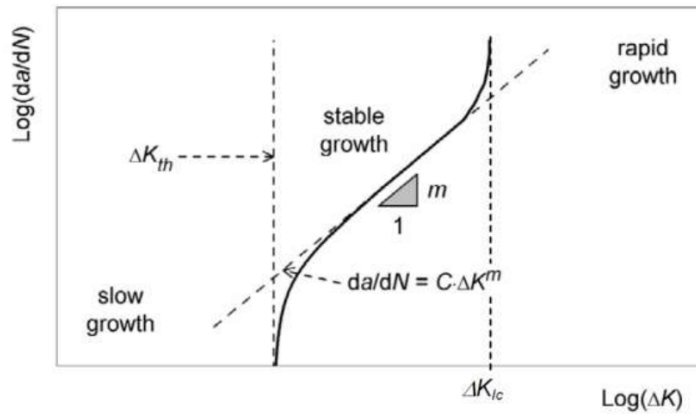


Figure 2.9: Fatigue crack growth [21]

## 2.4. Abaqus crack propagation method

In this section the methods used in Abaqus® will be elaborated. In this thesis Abaqus® version 6.14 and 6.17 of Dassault Systèmes Simulia Corp [8] have been used to model the specimen.

The following part is written using the document made by Zhen-zhong Du [45] of Dassault Systèmes Simulia Corp. Abaqus® has included a module to model the crack propagation using XFEM. The eXtended Finite Element Method has first been developed by Belyschko and Black [3]. Next to the regular finite element method two additional enrichment functions have been added to the displacement vector. These functions are used for the nodes at the crack-tip and around the crack opening. The region in which the crack can propagate and thus these two additional functions are applied are called the enriched region. The nodes around the crack are located in the enriched region. The two additional functions apply to the nodes in this enriched region. The equation 2.8 [45] applies for the enriched nodes.

$$u = \sum_{I=1}^N N_I(x)[u_I + H(x) \cdot a_I + \sum_{\alpha=1}^4 F_{\alpha}(x) \cdot b_I^{\alpha}] \quad (2.8)$$

Where:

$u$  = Displacement vector

$N_I(x)$  = Shape functions

$u_I$  = Nodal displacement vectors

$H(x)$  = Jump functions

$a_I$  = Nodal enriched degree of freedom vector

$F_{\alpha}(x)$  = Asymptotic crack – tip functions

$b_I^{\alpha}$  = Nodal enriched degree of freedom vector

The jump function applies to the nodes that attach to the crack surface, whereas the asymptotic crack-tip functions apply to the nodes that are attached to elements that are cut by the crack-tip. The regular shape functions are used in the normal FE-method and apply to all the nodes. In Figure 2.10 the nodes affected by the jump function  $H(x)$  are shown in the yellow, while the nodes affected by the asymptotic crack-tip function  $F_{\alpha}(x)$  are given in red.

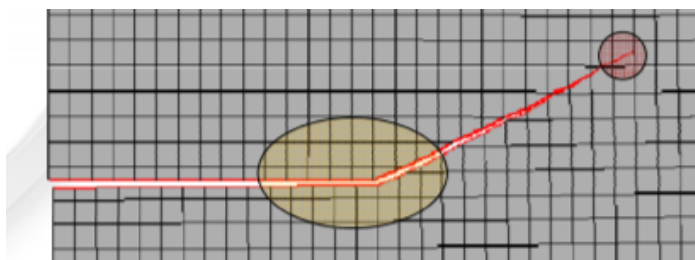


Figure 2.10: Additional functions XFEM [45]

The jump function  $H(x)$  is shown below, where  $x$  is a sample point,  $x^*$  is the point on the crack closest to  $x$  and  $n$  is the unit normal to the crack direction at point  $x^*$  [2]. The coordinates are shown in Figure 2.11.

$$H(X) = \begin{cases} 1 & \text{if } (\vec{x} - \vec{x}^*) \vec{n} \geq 0, \\ -1 & \text{otherwise} \end{cases} \quad (2.9)$$

The asymptotic crack-tip function  $F_\alpha(x)$  is shown below. A polar coordinate system is used for this formula, where  $r$  is the distance from the centre (crack tip) and  $\theta$  is the direction from the crack-tip. The direction of the crack at the crack tip is denoted as  $\theta = 0$  [2]. The coordinates are shown in Figure 2.11.

$$F_\alpha(x) = \left[ \sqrt{r} \sin \frac{\theta}{2}, \sqrt{r} \cos \frac{\theta}{2}, \sqrt{r} \sin \theta \sin \frac{\theta}{2}, \sqrt{r} \sin \theta \cos \frac{\theta}{2} \right] \quad (2.10)$$

In Figure 2.12 the blue square nodes are enriched nodes by the jump function  $H(x)$ , while the red circular nodes are enriched nodes by the asymptotic crack-tip function  $F_\alpha(x)$ . Around the enriched elements blending elements are applied, these elements are adjacent to the enriched elements. The rest of the specimen consists of regular non-enriched elements.

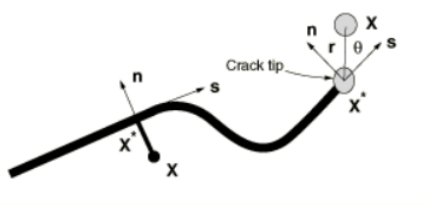


Figure 2.11: Normal and tangential coordinates additional functions XFEM [2]

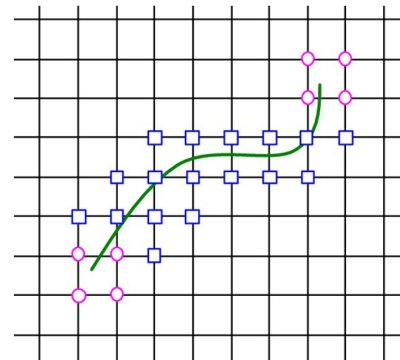


Figure 2.12: Crack XFEM enriched nodes [43]

Using this module, the asymptotic crack-tip function will be disabled in the finite element analysis. Only the jump function  $H(x)$  is used for crack propagation analysis. This has as consequence that in the finite element analysis only whole elements can crack during the crack propagation analysis. Therefore, a fine mesh is necessary in order to obtain the right crack propagation shape. However, a very fine mesh will also result in longer computing times.

In this study, the XFEM module within Abaqus® will be used in order to propagate the crack. There are several methods possible when using the XFEM module for crack propagation simulation. These possible methods are shown in Figure 2.13. Method 1 consists of re-meshing around the crack surface after crack growth. This is very intensive in terms of computing power and will result in long computing time, especially when considering a relative large specimen. Method 2 consists of manual crack control which will result in a well formed crack shape. In addition the computing time is reduced as the mesh does not need to be re-meshed at every crack propagation step. However, the results do not correspond very well with experimental data [33]. At last, method 3 is fully automatized within the XFEM module of Abaqus®. Cyclic loading ensures that the initial crack will propagate. The Power law is rewritten based on energy release rate. The energy release rate per element is calculated by VCCT, while the crack propagation of the individual elements is computed using the Paris Law based on energy parameters.

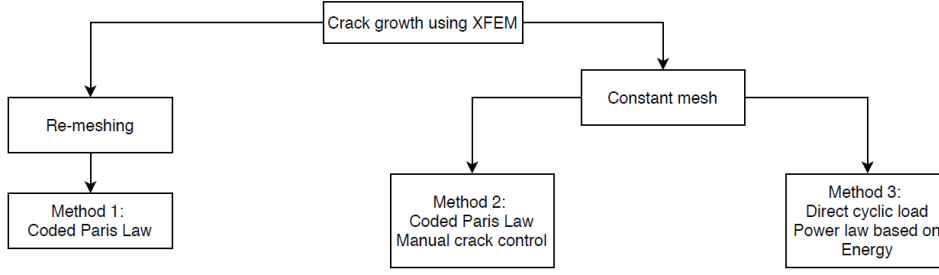


Figure 2.13: Crack propagation XFEM [33]

The direct cyclic loading simulates a varying load over time. When using the XFEM module, the direct cyclic loading is necessary in order to simulate the cycles that cause the crack to propagate. In order to create, this variable load an amplitude has to be created that is depended of time. The load will be multiplied by the amplitude. Within Abaqus® there a multiple options to create a variable load. Within this research there is chosen for a periodic amplitude as this is also chosen by W. Nagy [25]. This periodic function, shown in equation 2.11, is a function of time and amplitude. The parameters, shown in equation 2.12, are also used by W. Nagy [25]. This function will result in one cycle of fully loading and unloading within one second, shown in Figure 2.14. The loading ratio  $R$  is therefore zero, while the frequency is 1  $Hz$ .

$$y = A_0 + A_1 \cos(t - t_0) + B_1 \sin(\omega(t - t_0)) \quad (2.11)$$

$$y = 0.5 + 0 \cos(t - 0.5) + 0.5 \sin(2\pi(t - 0.5)) \quad (2.12)$$

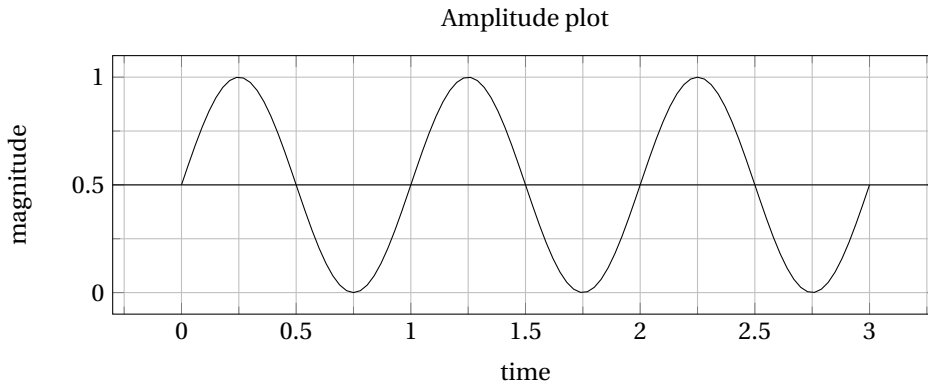


Figure 2.14: Amplitude direct cyclic loading

The Paris law parameters have to be defined into automate crack growth by Abaqus®. Usually in literature, like the thesis of W. Nagy [25], all the material parameters are described in terms of  $C$  and  $m$ , as shown in equation 2.7. The fracture toughness, denoted by  $K_{IC}$ , can not be used directly in the Abaqus® XFEM module. The SIF-parameters have to be rewritten to energy relation parameters in order to automate the crack propagation. In equation 2.13 [15], there can be seen that  $K_{IC}$  is rewritten to  $G_{IC}$ . The parameters in mode 2 and 3 are more difficult to obtain, and therefore often not available in literature. However, these two parameters can be rewritten to energy-parameters using formulas 2.14 and 2.15 [15].

$$G_{IC} = \frac{K_{IC}^2}{E'} [J/m^2] \quad \text{where } E' = \frac{E}{1 - \nu^2} \quad (\text{for plain strain}) \text{ and } E' = E \quad (\text{for plain stress}) \quad (2.13)$$

$$G_{IIC} = \frac{K_{IIC}^2}{E'} [J/m^2] \quad \text{where } E' = \frac{E}{1 - \nu^2} \quad (\text{for plain strain}) \text{ and } E' = E \quad (\text{for plain stress}) \quad (2.14)$$

$$G_{IIIC} = \frac{K_{IIIC}^2}{2\mu} [J/m^2] \quad \text{where } E' = \frac{E}{1 - \nu^2} \quad (\text{for plain strain}) \text{ and } E' = E \quad (\text{for plain stress}) \quad (2.15)$$

Within the XFEM module of Abaqus®, the following threshold [33] has to be overcome to start the crack growth. Usually constants  $c_1$  and  $c_2$  are set very low to immediately start the crack growth.

$$f = \frac{N}{c_1 \Delta G^{c_2}} \geq 1.0 \quad (2.16)$$

The following parameters apply on the Paris region described in section 2.3.1. Both material constants need to be rewritten in terms of energy. These terms are rewritten using equations 2.17, 2.18 and 2.19 [33]. Where  $\Delta G$  is the relative fracture energy release rate,  $E' = E$  for plane stress and  $E' = \frac{E}{1-\nu^2}$  for plane strain. The relative fracture energy release rate, denoted as  $\Delta G$ , is the range of fracture energy release rate between the maximum and minimum load situation [33]. Once the crack growth is started, equation 2.18 is used to model the stable crack growth.

$$\frac{da}{dN} = C \Delta K^m \quad (2.17)$$

$$\frac{da}{dN} = c_3 \Delta G^{c_4} \quad (2.18)$$

$$c_3 = C E'^{c_4} \quad c_4 = \frac{m}{2} \quad (2.19)$$

At last, the fatigue growth with energy relations are described. In Figure 2.15, the fatigue crack growth according to the Paris law is shown with energy relation parameters. Fatigue crack growth is only possible when equation 2.20 [33] is met. Within Abaqus®, this equation is related to the  $G_c$  by equations 2.21 and 2.22 [33]. Parameters  $C_1$ ,  $C_2$  and  $\frac{G_{thresh}}{G_c}$  are set very low in order to immediately start the crack propagation phase. Equation 2.22 determines the point at which unstable crack growth occurs in relation to the fracture toughness and is set to 0.85 based on previous research [15].

$$G_{thresh} < G_{max} < G_{pl} \quad (2.20)$$

$$\frac{G_{thresh}}{G_c} = 0 \quad (2.21)$$

$$\frac{G_{pl}}{G_c} = 0.85 \quad (2.22)$$

The  $G_c$  can be specified using various mixed mode models within Abaqus®. In this study, there is chosen to use the Power law shown in equation 2.23 [42].

$$\frac{G_{eq}}{G_{eqC}} = \left( \frac{G_I}{G_{IC}} \right)^{a_m} + \left( \frac{G_{II}}{G_{IIC}} \right)^{a_n} + \left( \frac{G_{III}}{G_{IIIC}} \right)^{a_o} \quad (2.23)$$

The procedure of crack propagation used by Abaqus® based on a combination of Paris Law and VCCT is illustrated in Figure 2.16. Using VCCT, the amount of energy to propagate the crack is computed. If the amount of energy is higher than  $G_{thresh}$  the element will crack. The stable crack growth of the element will be calculated using equation 2.18 (Paris Law) in which the propagation direction, length ( $\Delta a$ ) and amount of load cycles (N) are computed. After the element is cracked, the stress field is re-calculated and the next element that cracks is calculated based on VCCT and the Paris law. The element in the enriched region, which requires the least amount of cycles will be cracked first. This procedure is repeated which results that every step correspond with the propagation of one element at a certain number of load cycles[33].

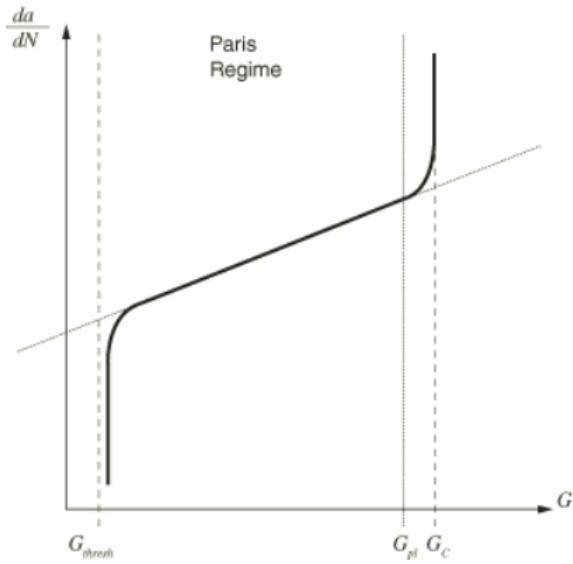


Figure 2.15: Fatigue Crack growth Paris law[9]

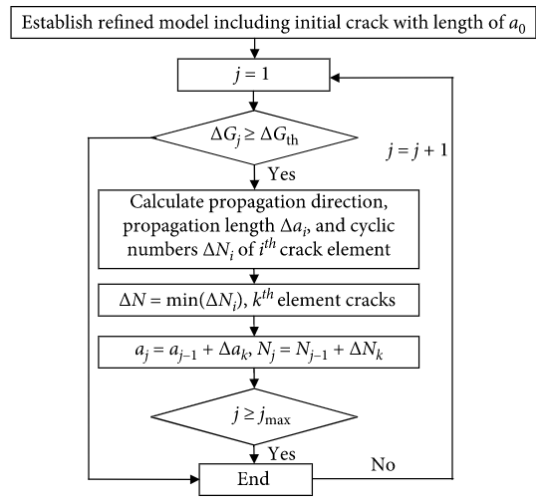


Figure 2.16: Procedure X-FEM Abaqus [38]



# 3

## Welding simulation analysis

In this chapter the welding simulation analysis will be described, which is performed to obtain the residual stress field that occurs due to the welding process between the trough and the deck plate. The modelling of the welding process is divided into two phases. In the first part, a thermal analysis is performed in which the heat transfer of the welding arc to the specimen is modelled using FEA. In this part the temperature increase caused by the welding arc is modelled per time step in Abaqus®. In the second part the stresses caused by the temperature change are modelled. These stresses are introduced by restrained deformation due to expansion and shrinkage of the elements within the specimen. At the end of the simulation the obtained residual stress field is used in the fatigue crack propagation simulation. The method of the weld simulation model is based on the MSc-thesis of K. Spyridoni [34]. Her thesis was focussed on the modelling of residual stresses of a orthotropic deck specimen. The geometry of the welding simulation model is based on the OSD-specimen of W. Nagy [25]. Therefore a new model has been built which has the same geometry as used in the thesis of W. Nagy. The units has been changed from *m* to *mm*, as this is more convenient when modelling the crack propagation in Chapter 4 of the thesis.

During both the mechanical and thermal analysis a number of assumptions have been made in order to simulate the welding conditions of the experiment. These assumptions might influence the results in some extend. All assumptions are listed below.

- It is assumed that both the parent material and the filler material are the same according to the NEN-EN 1993-1-2 [26]. The filler material can have different material properties. In addition, the material properties could be different in the HAZ compared to the rest of the OSD-specimen.
- No material, geometrical and weld imperfections are modelled. Geometric imperfections consist for example of a slightly curved deck plate or variations in thickness of the specimen. The material properties of the FEM-model are constant over the whole specimen. At last, weld imperfections like lack of penetration and slag inclusion are ignored.
- The mechanical analysis does not result in a constant residual stress field over the cross-section due to the boundary conditions and thermal expansion. Therefore, the cross-section at  $z=-380$  mm, which are verified with the experimental data, is assumed to be present over the whole cross-section in the fatigue crack propagation analysis. The reasoning behind this assumption is described in section 3.2.2.

### 3.1. Thermal model

#### 3.1.1. Geometry of the model

As mentioned before, the specimen used in this research will be identical to the specimen used in the research of W. Nagy [25]. The geometry of the OSD-specimen according to W. Nagy[25] is shown in Figure 3.1. The specimen has a depth of 400 mm, which is shown in Figure 3.2. The specimen is supported by two supports at either side of the through. At the left-hand side, the specimen is supported by a clamped support with a width of 40 mm (x-direction). At the right-hand side, the specimen is supported with a pinned support placed 50 mm away from the edge of the specimen. The deck has a thickness of 15 mm, while the trough

has a thickness of 6 mm. The mechanical loading that is placed on top of the model will be described in the fracture model, as the model is not mechanically loaded while the specimen is welded.

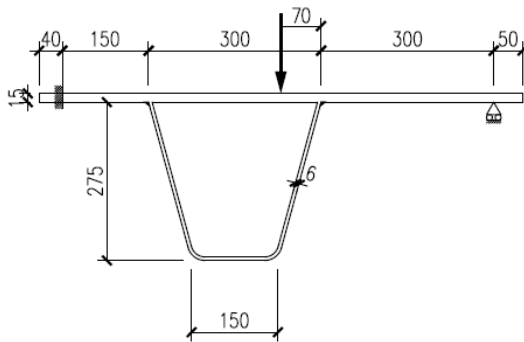


Figure 3.1: Geometry OSD-specimen [25]

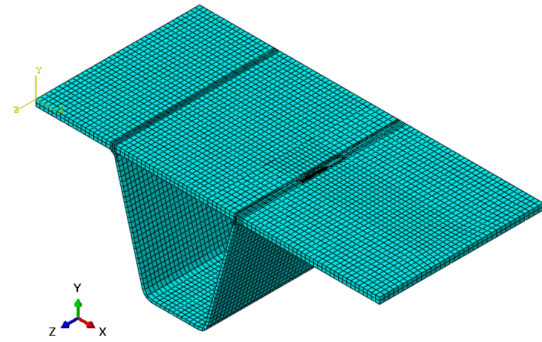


Figure 3.2: 3D model OSD-specimen

All the specimens are welded using an automated welding machine. The exact geometry of the weld is not described in the thesis of W. Nagy. Therefore an estimation of the weld geometry has been made on a photo, shown in Figure 3.3. The final weld geometry based on the drawing is shown in Figure 3.4. It is assumed that there are no imperfections in the weld and the weld is fully penetrated.

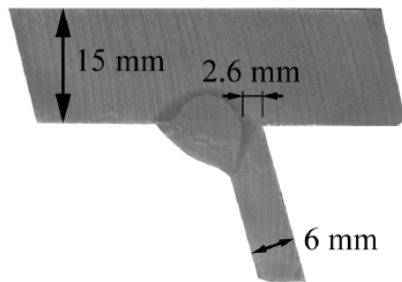


Figure 3.3: Image weld [25]

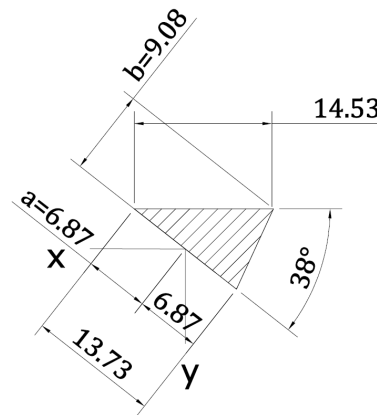


Figure 3.4: Weld geometry in millimeters

### 3.1.2. Units

As mentioned in the introduction of this chapter, the model of the OSD-specimen has been built in millimeters. This has certain advantages when modelling the crack propagation model as the stress units is then in MPa and the crack length is in millimeters instead of meters. Within Abaqus®, it is required to change all the units with the change in model size. Almost all units have to be changed due to the change in the dimension unit. For keeping things organised, the units applied by K. Spyridoni and N. van den Berg are shown in Table 3.1.

Property	K. Spyridoni		N. van den Berg	
	Value	Unit	Value	Unit
Length	1	<i>meter</i>	1000	<i>millimeters</i>
Density	7850	$kg/m^3$	$7.850 \cdot 10^{-9}$	$Tonne/mm^3$
Temperature	-273.15	<i>K</i>	-273.15	<i>K</i>
Conductivity	53.33	$W/m.K$	53.33	$mW/mm.K$
Specific Heat	439.802	$J/kg.K$	$4.39802 \cdot 10^8$	$mJ/Tonne.K$
Convection	10	$W/m^2.K$	0.01	$mW/mm^2.K$
Emissivity	0.5		0.5	
Heat Flux	1000	$W/m^3$	1	$mW/mm^3$
Energy	1	<i>J</i>	1000	<i>mJ</i>
Stefan-Boltzmann constant	$5.67 \cdot 10^{-8}$	$W.m^{-2}.K^{-4}$	$5.67 \cdot 10^{-11}$	$mW.mm^{-2}.K^{-4}$

Table 3.1: Units heat input model

### 3.1.3. Material properties

There is chosen to use S355 steel, as this is also applied in the research of W. Nagy [25]. However, there are no properties at elevated temperatures specified in that research. These properties are necessary for the weld simulation model. Therefore there is chosen to apply the material properties according to NEN-EN 1993-1-2 [26] also used by K.Spyridoni [34]. The material properties are shown in Figure 3.5. In Figure 3.6, the stress-strain diagram per temperature °C according to the NEN-EN 1993-1-2 [26] is shown.

### 3.1.4. Element activation

In this section, the 'birth and death' principle will be elaborated. This principle has been applied in the work of K. Spyridoni in order to simulate depositing of weld material to the OSD-specimen during the weld process. To describe this principle, the thesis of K. Spyridoni [34] is used. This element activation method is applied in both the thermal and mechanical analysis. At the beginning of the weld process, no weld material is present between the deck plate and the trough. The total weld has been divided in the FEM-model in 'weld elements' with a length of 10 mm. At the start of the analysis, no weld material should be present between the deck plate and the stiffener. However, before the analysis in Abaqus® is able to start, the necessary weld elements were modelled. Therefore, in step 1 all the weld elements are deactivated using the command 'Model change' in Abaqus®. This process results in the 'death' of these weld elements. After all the weld elements are deactivated, the thermal analysis can start. Every time step, a weld element is reactivated using the 'Model change' command in the model. This process is the 'birth' of these elements. Simultaneously, the heat source model, described in section 3.1.5, moves over the reactivated element. This simultaneous process simulates the heat input of the arc and the depositing of weld material to the OSD-specimen. During the deactivation of all the weld elements, it is made sure that the remaining OSD-specimen is stress-free. When a weld element is reactivated, this element is free of any stress and strain. The sequence of weld elements is added to Annex B.

### 3.1.5. Welding simulation

In this section the welding simulation in the FE-model will be described. The welding simulation will be almost the same compared to the research of K. Spyridoni [34], only the units and the parameters for the welding will be different. In this model the temperature of the specimen during the welding process will be modelled using Abaqus®. The temperature at each node is registered per time increment. It is therefore important to have a fine mesh around the weld area, as the temperature gradient will be large.

During the welding process, fillet material is added in the opening between the trough and deck of the orthotropic steel deck. During this process, a heat source is applied in order to bond the fillet material to the parent material. After the fillet material is added, the joint cools down as the heat source has been removed. This process will be modelled using a transient thermal analysis within Abaqus®. The thermal process, shown in Figure 3.7, can be divided into three parts: Heat input due to the welding arc, heat transfer through the specimen and heat loss to the environment [34].

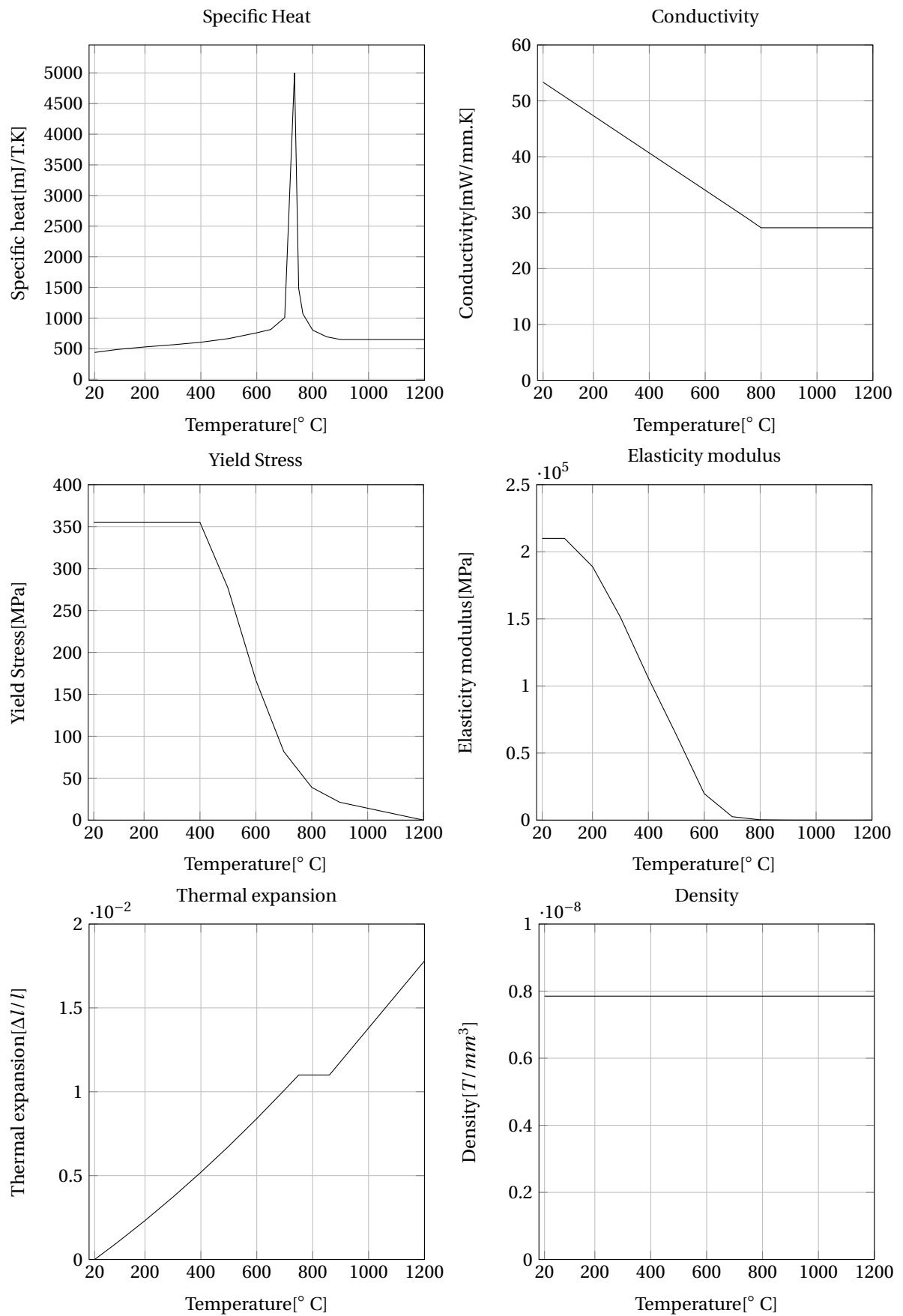


Figure 3.5: Material properties [26]

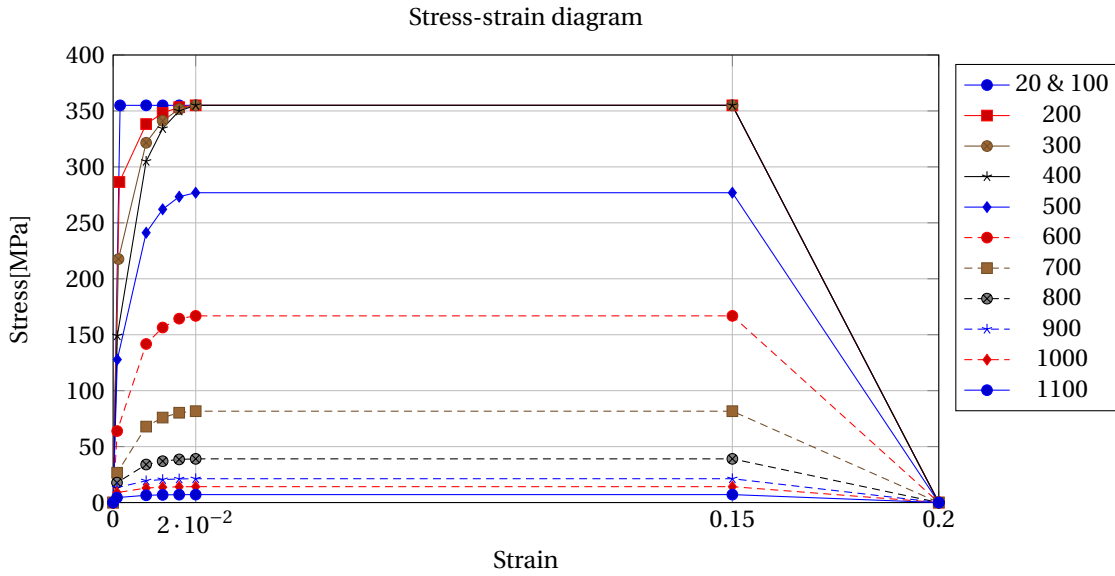


Figure 3.6: Stress-strain diagram

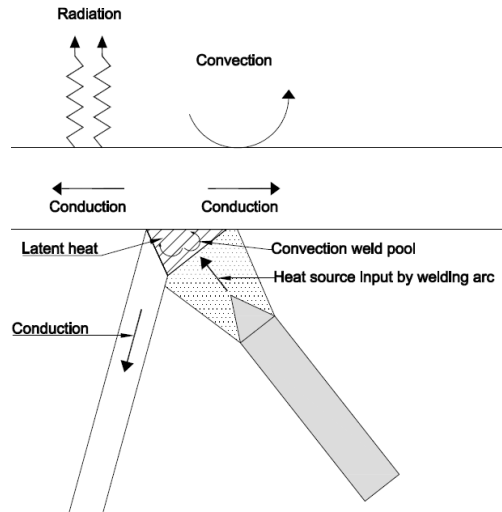


Figure 3.7: Thermal process during welding

This thermal process can be represented by equation 3.1.

$$c \rho \frac{\partial T}{\partial t} = k \left( \frac{\partial^2 T}{\partial x^2} \right) + k \left( \frac{\partial^2 T}{\partial y^2} \right) + k \left( \frac{\partial^2 T}{\partial z^2} \right) + q \tag{3.1}$$

Where  $T$  is the temperature in  $^{\circ}C$ ,  $t$  is the time in seconds,  $\rho$  is the density in  $T/mm^3$ ,  $c$  is the specific heat capacity in  $mJ/T.K$ ,  $q$  is the internal heat generation rate in  $mW/mm^3$  and  $k$  is the thermal conductivity in  $mW/mm.K$ .

The heat flux will be modelled using a DFLUX subroutine within Abaqus®. This subroutine is added to Annex A. With the subroutine the heat energy input caused by the welding can be specified by magnitude time and location within the model. Within the subroutine the heat flux is calculated using two formulas and the specified weld parameters. The heat source model used by K. Spyridoni has been developed by Goldak et al. [13]. This model consist of two ellipsoidal shapes, shown in Figure 3.8, in which the heat flux is modelled that is introduced by the welding. The heat flux is modelled by two power density distributions. There is one formula for the front half ellipsoid and one for the rear half ellipsoid. The front power density distribution is

described as:

$$q_f(x, y, z) = \frac{6\sqrt{3}f_f Q}{abc_f \pi \sqrt{\pi}} e^{-3x^2/a^2} e^{-3y^2/b^2} e^{-3z^2/c_f^2} \quad (3.2)$$

While the rear power density distribution is described as:

$$q_r(x, y, z) = \frac{6\sqrt{3}f_r Q}{abc_r \pi \sqrt{\pi}} e^{-3x^2/a^2} e^{-3y^2/b^2} e^{-3z^2/c_r^2} \quad (3.3)$$

All parameters used in both formulas are shown in Figure 3.9. In both equations  $Q$  is the power output of the welding machine defined in mW. Within the subroutine, the  $Q$  is specified by multiplying the current  $A$ , Voltage  $V$  and the efficiency. These parameters are obtained from the thesis of W. Nagy [25]. Submerged Arc Welding (SAW) has been used for welding the OSD-specimens. Before the SAW, the through and deck plate were connected using a few tack welds. For the SAW welding a automatic single wire welding machine has been used. The specimen was first welded on one side, and then back from the other side. Parameters  $a$  and  $b$  are based on the geometry of the weld. Parameter  $a$  is defined by half of the width of the weld, while parameter  $b$  is defined by the depth of the molten zone. The magnitude of both parameters is shown in Figure 3.4. Parameters  $c_f$  and  $c_r$  define the length of the front and rear ellipsoid. Both parameters are related to the weld geometry parameter  $a$ . According to Goldak et al. [13],  $c_f$  is approximately the same as parameter  $a$ , while  $c_r$  is defined as  $c_r = 2.33c_f$ . Parameters  $f_f$  and  $f_r$  define the amount of energy that goes to the front ellipsoid and rear ellipsoid. Goldak et al. [13] and experimental data, show that  $f_f + f_r = 2$ ,  $f_r = 1.4$  and  $f_f = 0.6$  will result good results.

At last, the  $x, y$  and  $z$  parameters are described. These three parameters determine the position of the heat source within the FEM-model. Within the subroutine, the time and coordinates are used as input. The subroutine has the coordinates within the FEM-model that are subjected to a heat flux and the magnitude of this heat flux at each time step as output. The origin of the heat model, shown in Figure 3.8, start at the origin of the FEM-model shown in Figure 3.10. However, the heat source model has to be rotated in order to correctly heat the fillet material. Within the subroutine the coordinate system is rotated with 38 degrees, shown in Figure 3.11. With the rotation of the coordinate system within the subroutine, the starting position of the heat source model within the FEM-model has been defined. According to W. Nagy [25], the automatic welding machine moves with a speed of 550 mm/min to 650 mm/min. There is assumed that the average speed is 10 mm/s, this will be the speed that will be used in the FEM-model. The coordinates within the subroutine that determine the position of the heat source model are changed with each time step. Every second the heat source model moves 10 mm/s in negative  $z$ -direction. After 40 seconds, one side of the specimen, with a length of 400 mm, has been 'welded' with time steps of 10 mm/s. After the heat source model has passed the first side of the OSD-specimen, a short cooling period of 100 second is analysed by the FEM-model. This cooling period is applied because the welding machine has to be moved to the other side of the specimen. After the first cooling period the specimen is welded in the next 40 seconds. After both sides have been welded, a longer second cooling of 4000 seconds is applied. This is so that the specimen can cool down completely. After these 4000 seconds the temperature field data analysis is finished. This temperature field data is used for the calculation of the residual stresses in the mechanical model.

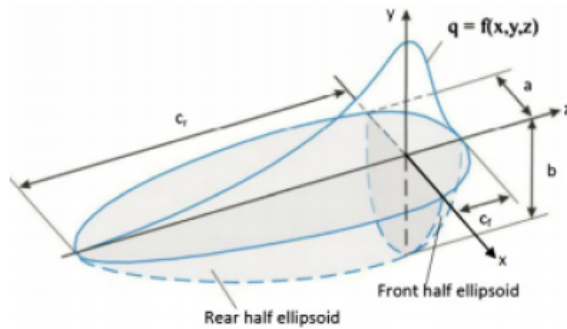


Figure 3.8: Heat source model [19]

Welding Properties		
Welding Speed	10	mm/sec
Current	26	A
Voltage	600	V
Efficiency	0.95	
Heatflux	$1.48 \times 10^7$	mW/mm <sup>2</sup>
Width a	6.87	mm
Depth b	9.08	mm
Front c <sub>f</sub>	6.87	mm
Back c <sub>r</sub>	16	mm
Heat front f <sub>f</sub>	0.6	
Heat back f <sub>r</sub>	1.4	

Figure 3.9: Welding properties

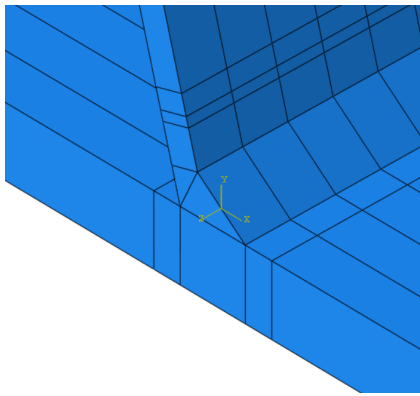


Figure 3.10: Origin FEM-model

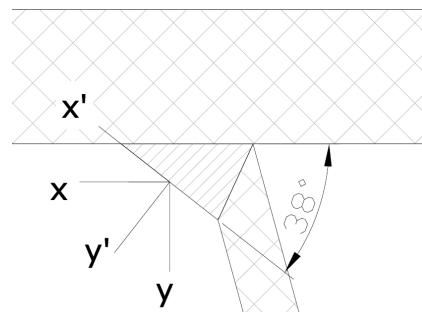


Figure 3.11: Rotated coordinate system

### 3.1.6. Mesh

In Figure 3.12 and 3.13, the mesh is shown as overview and in detail. Figure 3.13 shows that the mesh has been refined around the weld area. In this way, there are less elements needed for building the model, as the thermal analysis is time consuming in terms of computing time. With the current mesh the computing time on a workstation (Xeon® W2123) is around four full days of running time, due to the relative large OSD-specimen. The weld itself has the smallest elements with a size of 1.75 mm. There is chosen to apply wedge elements (DC3D6) due to the triangular shape of the weld. The deck plate has been modelled with hexahedral elements (DC3D8) that have a size of 10 mm and a height of 5 mm. Between the hexahedral elements and wedge elements there is chosen for tetrahedral elements (DC3D4) to transition in element size and type.

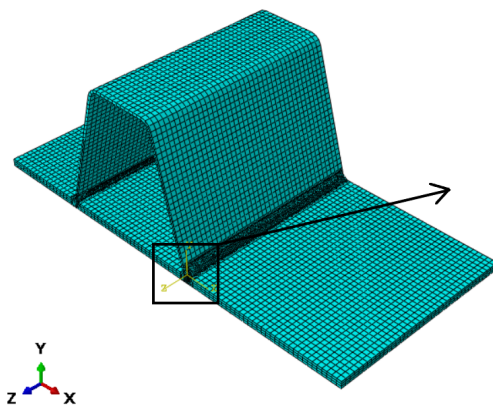


Figure 3.12: Overview mesh

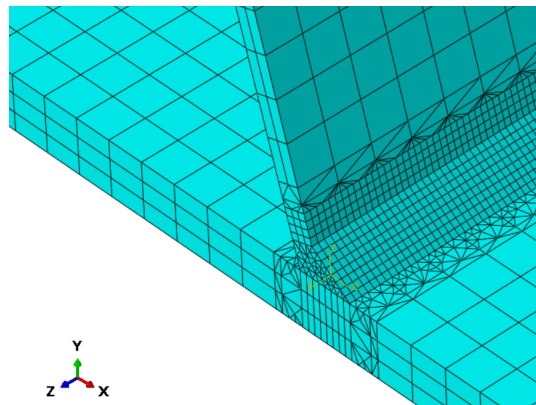


Figure 3.13: Mesh detailed view

### 3.1.7. Results

In this section the results of the thermal analysis will be described. The results of the thermal model are temperature field data at every time step over the whole FEM-model. Unfortunately, no temperature data has been recorded during the welding process of the research done by W. Nagy. Therefore it is hard to verify the results of the thermal analysis. Nevertheless, in Figure 3.14, the molten zone of the weld in the OSD-specimen is shown. The molten zone of the experiment in the research of W. Nagy can be compared with the thermal analysis. It is assumed that the steel used in the experiment melts around 1200 degrees. The contour plot of the weld area at  $z = -200$ , where temperatures  $\geq 1200^\circ\text{C}$  are denoted in light grey is shown in Figure 3.15. A comparison between the two models is shown in Figure 3.16. The molten zone of the FEM-model is slightly underestimated compared to the results of the experimental data. Overall, the shape of the molten zone is similar compared to the experiment. However, it must be noted that a comparison between a cross-section of an OSD-specimen and a contour plot is not as accurate as comparing experimental data with results from the FEM-model. This will be done in Chapter 3.2 as experimental data of the residual stresses is available.

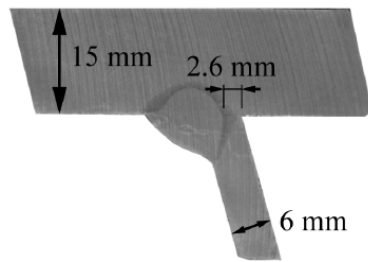


Figure 3.14: Weld experiment [25]

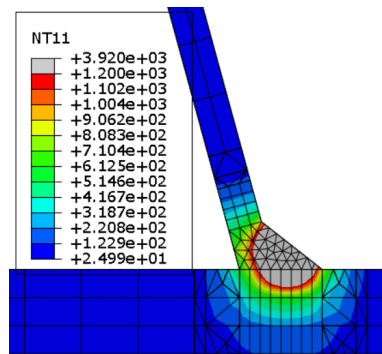


Figure 3.15: Heat model weld

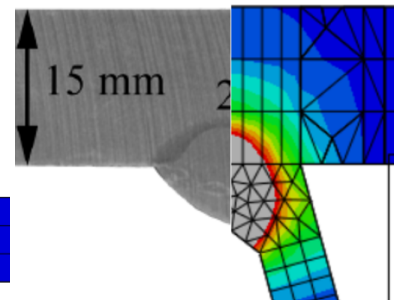


Figure 3.16: Comparison between experiment [25] and FEM-model

## 3.2. Mechanical model

In this part of the chapter, the temperature field data obtained in the thermal analysis will be used in the mechanical analysis in order to model the residual stress due to welding process. This residual stress field will be compared to the experimental data of W. Nagy.

### 3.2.1. Mechanical analysis

In order to obtain the residual stresses a mechanical FEM-analysis has been performed. The temperature field data is used as predefined field input during the analysis. During the mechanical analysis, similar time steps as in the thermal model are applied. Also a similar sequence in the 'birth and death' principle has been used in order to obtain valid results. The FEM-model obtains the stresses due to the temperature depended material properties described in section 3.1.3. During the mechanical analysis the material expands and shrinks due to the changes in temperature. During this variation in volume, stresses are generated due to restrained deformation. At the end of the mechanical analysis, the residual stress field is obtained due to the welding of the OSD-specimen.

### 3.2.2. Boundary conditions

During the mechanical analysis, the mechanical boundary conditions (BC) of the OSD-specimen influence the stress distribution greatly [34]. However, there is little information on the boundary conditions during the welding process other than the picture shown in Figure 3.17. However, the research of K. Spyridoni [34] was a starting point of finding the right boundary conditions for the mechanical analysis. The OSD-specimen should not be restricted in such way that it cannot expand due to the increased temperature, this would lead to higher residual stresses due to additional restrained deformation. In contrary to the research of K. Spyridoni, there are no rotational restrictions applied as the specimen is clearly not clamped in Figure 3.17. However, there are supports applied in each direction in order to keep the specimen in the same place when the elements are activated step by step over time, due to the 'birth and death' principle. Otherwise, the elements are placed not at the correct position, because the OSD-specimen was displaced in a unsupported direction. The boundary conditions in each of the three directions are shown in Figure 3.18. At  $z = -400 \text{ mm}$ , the OSD-specimen is supported in the  $z$ -direction. While at the right-hand side of the specimen, the specimen is supported in the  $x$ -direction.

The support in the  $y$ -direction was more difficult to determine, as this support can greatly influence the results. First the tack welds are simulated in the FEM model. During the production of the specimen a number of tack welds are placed in order to keep the trough and deck connected. These tack welds are modelled by not deactivating the welds at each corner at the first step. This ensures that the trough and deck cannot displace from each other. Due to the heat introduced into the mechanical model, the specimen was expanded. In the manufacturing process, the OSD-specimen was in unrestrained condition in both  $x$ - and  $y$ -direction. As the free edges can deform freely, the residual stresses at these edges is very low, while at the restrained edges the residual stresses are very high. This phenomenon is shown in Figure 3.19 with the red arrow, where at the right upper corner the residual stresses will be relatively high and at left lower corner relatively low. The residual stresses of this cross-section will be assumed constant over the whole cross-section during the fatigue crack simulation. As can be seen in Figure 3.17, a section of 4000 mm is welded, wherefrom OSD-

specimens of 400mm are cut. In this way, the OSD-specimens in the middle have a near constant residual stress over the length of the weld. This justifies the method of using a cross-section of the residual stress field over the whole length of the OSD-specimen in the fatigue crack propagation simulation as the residual stress field will be constant over the whole width (z-axis) of the specimen. Therefore, it is important to evaluate at which cross-section the residual stresses correspond with the experimental data. A type of parametric study has been performed in order to find the boundary conditions and cross-section that corresponds with the literature data [25]. All the boundary condition variants are shown in Table 3.2. Two variants correspond well with the experiment. In the first variant (BC7), no support is applied. The support in the y-direction relies fully on the four tack welds. The second variant (BC8), consists of y-supports at the four corners off the specimen. The boundary conditions are activated during step 1, this result in a stress free specimen when all the weld elements are deactivated in the same step. Overall, the OSD-specimen can freely expand due to the un-symmetrical boundary conditions in every axis, this prevents overconstraining the specimen and unrealistic high residual stresses [34]. The results of most relevant variants are shown in Figures 3.30, 3.31 and 3.32. In order to keep the graphs readable, not all variants are shown. The results are compared with experimental data in section 3.2.6.

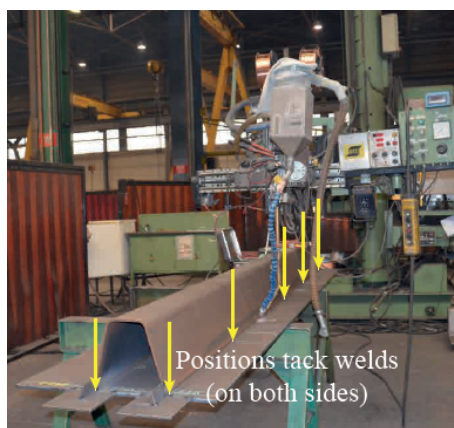


Figure 3.17: Overview welding process boundary conditions [25]

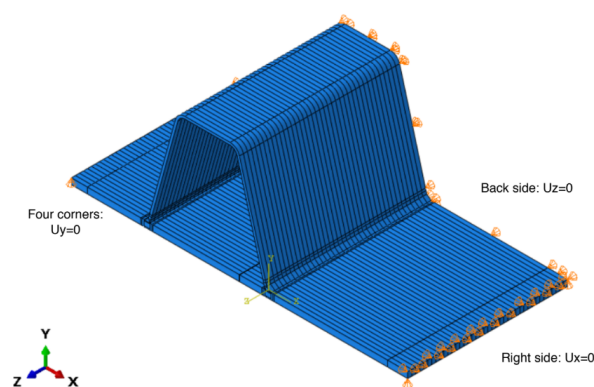


Figure 3.18: Boundary conditions

BC	Y-support	Z-axis [mm]	Side
BC1	Support under the weld	-200	Right
BC2	Deck supported	-200	Right
BC3	4 corners	-200	Right
BC4	4 corners	-200	Left
BC5	No support	-200	Right
BC6	No support	-380	Left
BC7	No support	-380	Right
BC8	4 corners	-380	Right

Table 3.2: parametric study boundary conditions

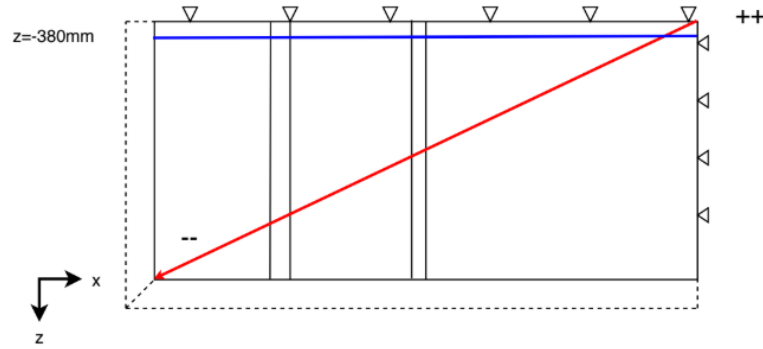


Figure 3.19: Thermal expansion mechanical model

### 3.2.3. Mesh

In Figure 3.20 and 3.21, the mesh is shown as overview and in detail. The mechanical analysis requires less computing time compared to the thermal analysis, however it still takes 2.5 days (Xeon® W2123) to compute with the current mesh. The mesh is refined around the weld area as there the difference in stresses would be large. In the refined mesh area, the mesh size is set to 0.5 mm in order to verify the results with the experimental data of W. Nagy. In the deck linear hexahedron (C3D8R) elements are applied, where in the refined area these have a size of 0.5 mm. Linear wedge elements (C3D6) have been applied to the weld itself. In between the refined and non-refined mesh, tetrahedron (C3D4/10) elements have been applied to transition in element type and size. For the rest of the non-refined mesh, two layers of linear hexahedron (C3D8R) elements are applied with a size of 10 mm.

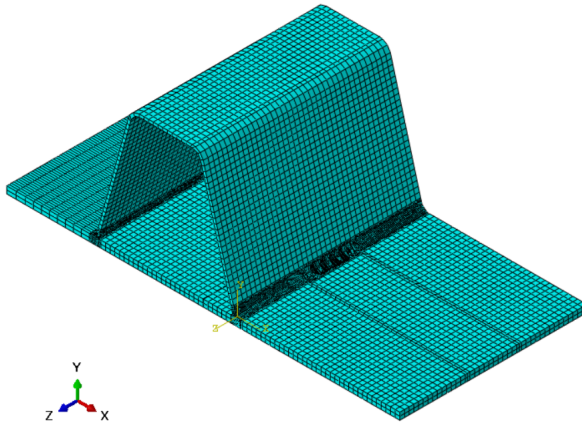


Figure 3.20: Overview mesh mechanical model

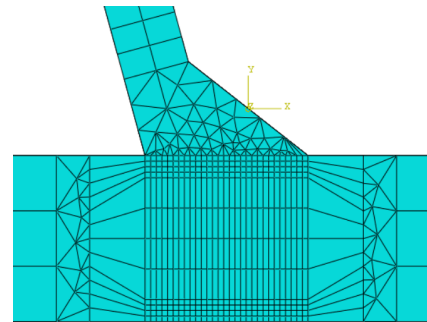


Figure 3.21: Cross-section mesh mechanical model

### 3.2.4. Stress discontinuities

After the first results, there were some stress discontinuities visible between the welds when using the parameters described in the previous paragraphs. These stress discontinuities are shown in Figure 3.22, in which light grey are tensile stresses  $\geq 300 \text{ MPa}$  and dark grey are compressive stresses  $\leq -300 \text{ MPa}$ . As described before, at each time step, 10 mm of weld material is re-activated within the model. At each interfaces between these groups of 10 mm of weld material stress discontinuities occur. These discontinuities, cause tensile stresses on one side and compressive stresses on the other side. The discontinuities are caused by the expansion of the elements due to the heat and simultaneous activating the next weld-element when the previous weld-element is at its maximum temperature. Weld-element (length 10 mm)  $n_i$  is heated by the heat source, and thus expands during the mechanical analysis. When weld-element  $n_{i+1}$  is re-activated at its original position, there is interference due to the expansion of weld-element  $n_i$ . The FEM-model 'solves' the problem of overlapping elements, by introducing tensile and compressive stresses to connect the nodes of the re-activated weld-element  $n_{i+1}$ . This FEM-problem on itself is not a problem as the results can be

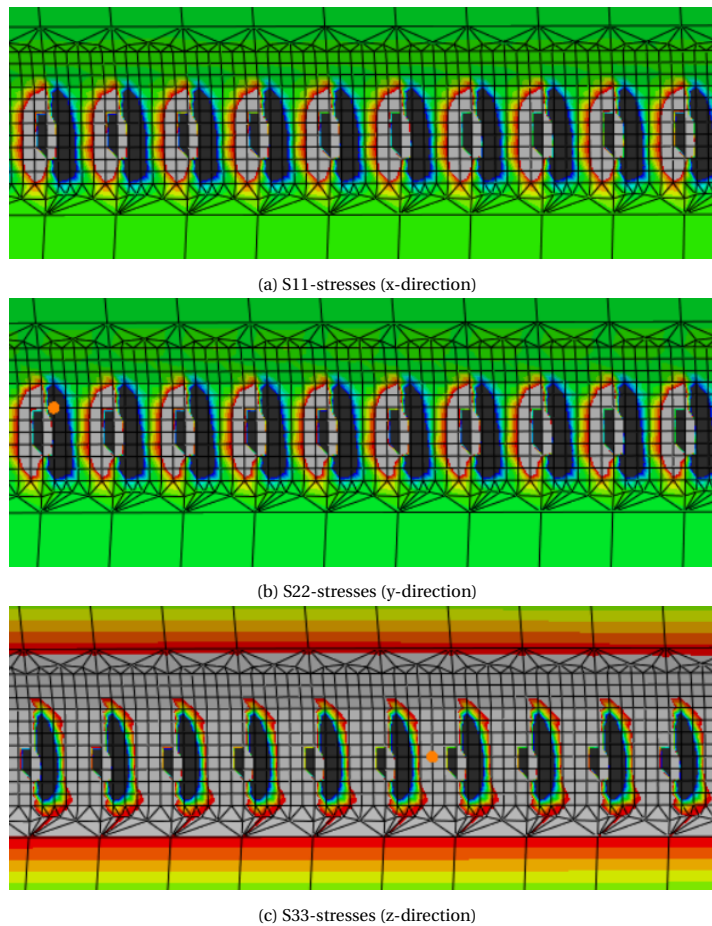


Figure 3.22: Stress discontinuities

analysed in between the discontinuities. However, the compressive stresses will slow down the crack propagation path of the initial crack. In order to minimize these stress distortions, two parameters of the model have been changed compared to the method of K. Spyridoni. Firstly the material properties have changed. One parameter has been added to the properties described in section 3.1.3. The parameter 'anneal temperature' in Abaqus® has been added. This temperature has been set to 1000 °C and is applied to the whole model. This means that when an element reaches 1000 degrees Celsius, the plastic strain of the element till that time step is set to zero [1]. When the temperature drops below the set temperature, the plastic strain starts recording again from zero. This means that above 1000 degrees Celsius the material acts like it is liquid and when the temperature cools down below the 'anneal temperature' it starts strain-free. This reduces the stress-discontinuities, as at the moment at which the new weld element is re-activated, the temperature of the already activated weld element is very high. Due to this high temperature, the material will act like a liquid, and hardly any stresses will be generated due to the re-activation of the new weld element. The stress-discontinuities will be reduced due to this added material parameter.

In addition, the 'birth and death' sequence is modified in order to reduce the stress discontinuities. In the first results with the stress discontinuities, the same sequence as in the thermal analysis was applied in the mechanical analysis. This method was based on the sequence that was applied in the work of K. Spyridoni [34]. However, in order to reduce the stress discontinuities, the predefined temperature field is applied before the weld element is added. In this way, the already activated weld element has the highest temperature before the new element is re-activated. This re-activated weld element is heated very fast, due to the shift in the predefined temperature field. This causes less plastic strains between the weld elements. The sequence of each step with its corresponding predefined temperature field is added to Annex B. The time step size has been adjusted in order to correspond with the time steps of the predefined temperature field. Otherwise, there would be not enough sufficient cooling time in order to cool down the OSD-specimen.

Fortunately, the results with the changed parameters above have resulted in better results in terms of stress

discontinuities. The improved results are shown in Figure 3.23 in which the stress scale is the same as in Figure 3.22. It must be noted that compared to Figure 3.22, the mesh is different in order to obtain the effect of a smaller mesh size. However, on both outer sides the mesh is exactly the same. In Figure 3.23a and 3.23b, the tensile stresses have been reduced between the weld elements. While in Figure 3.23c, the compressive stresses between the weld elements have been eliminated. The mesh refinement in the middle of the specimen reduces the stress discontinuities even further. In an ideal scenario an almost constant stress should be present along the length of the weld. It is not possible to refine the mesh over the whole specimen due to the increase in computing time.

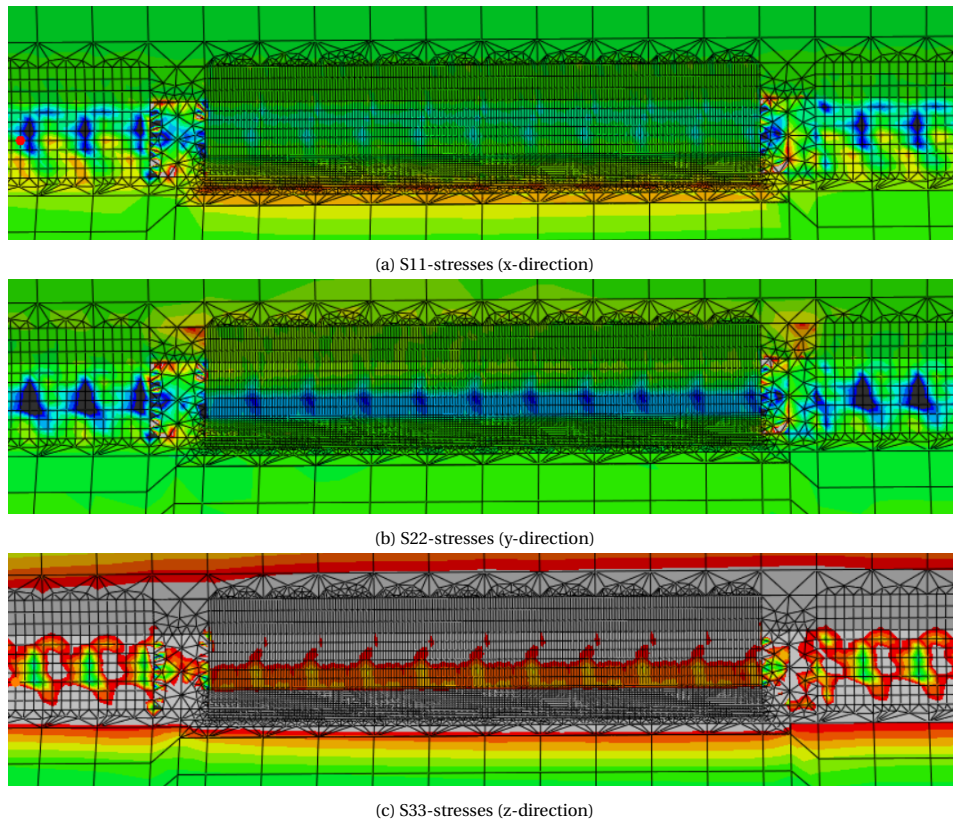


Figure 3.23: Revised stress discontinuities

### 3.2.5. Results

In this section the residual stresses along the deck and the trough are plotted. The results of variant 8 (BC8) are shown. In Figure 3.24, the S33-stresses along the deck plate are shown. The results are not symmetric as at one connection the mesh is refined. In Figure 3.25, 3.26 and 3.27, the S33-stresses are shown along the troughs. The differences between the left and the right joint are very little. The stresses are obtained at the middle of the specimen ( $z = -200 \text{ mm}$ ). The residual stresses are compared to the experimental data in section 3.2.6.

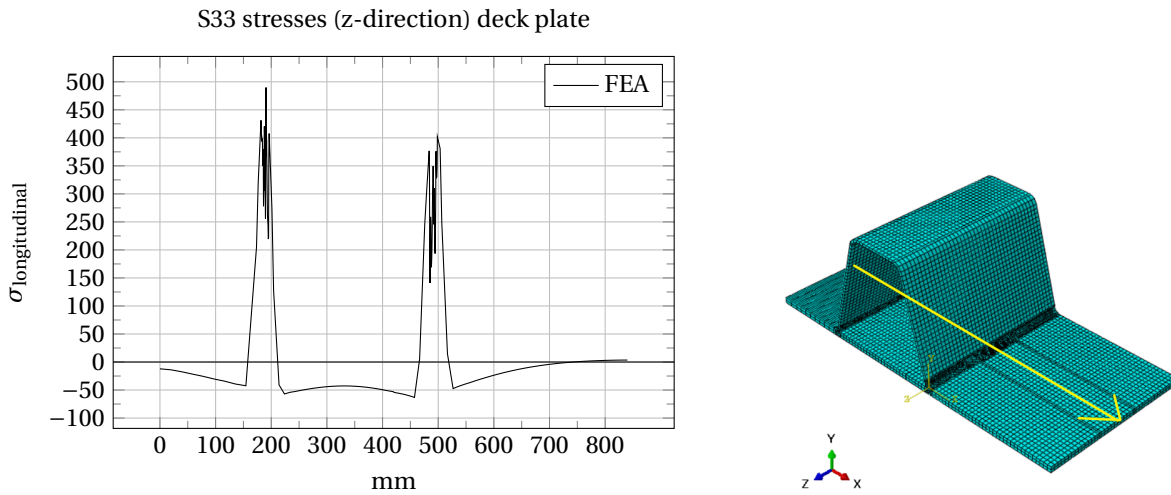


Figure 3.24:  $\sigma_z$  along deck plate

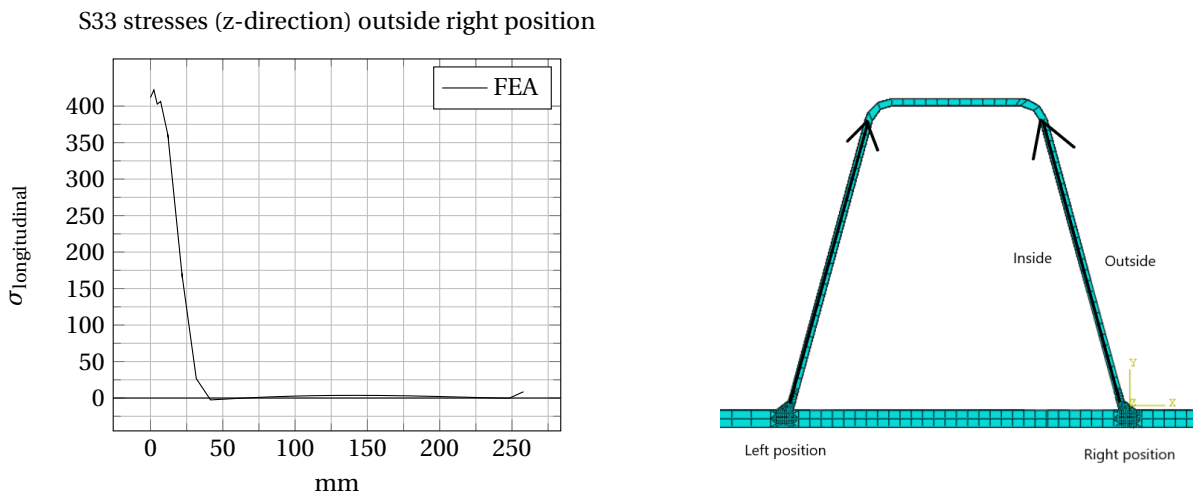


Figure 3.25:  $\sigma_z$  Right position outside

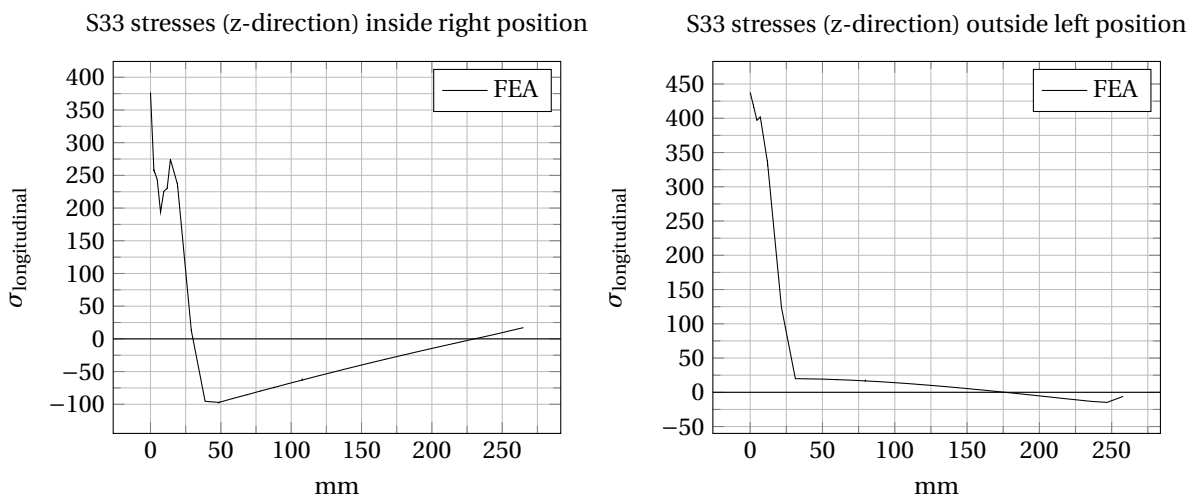


Figure 3.26:  $\sigma_z$  right position inside and  $\sigma_z$  left position outside

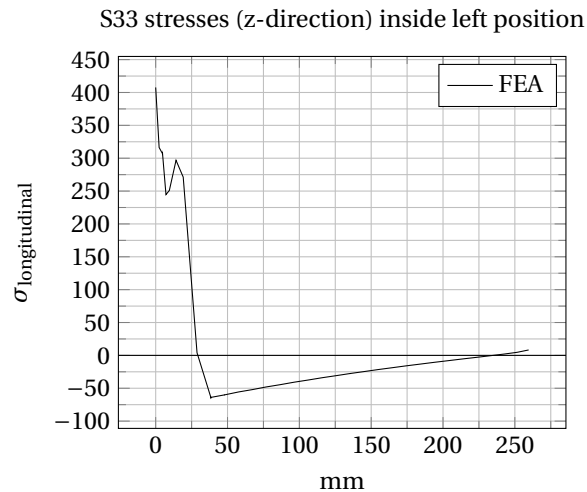


Figure 3.27:  $\sigma_z$  left position inside

### 3.2.6. Verifying results

The results of the residual stresses obtained by the mechanical model will be compared with the results of W.Nagy [25] using experimental data.

In the thesis of W.Nagy [25], the residual stresses due to the welding process have been monitored. This research has been done by incremental hole-drilling (IHD) measurements. During the welding process, residual stresses are introduced around the weld area. The magnitude of these stresses can be obtained using this method. A special type of strain gauge, Strain Gauge Rosettes (SGR), are installed around the weld area. After the welding process, a very small blind hole is drilled into the specimen. Due to the removal of material, there will be redistribution of the residual stresses around the hole. This redistribution of stresses and relieved strains caused by the hole can be monitored by the surrounding strain gauges. These relieved strains can be reversed calculated into stresses that were present before the hole was drilled. The hole is drilled through the SGRs. Only a small depth of the specimen can be analysed, due to the very small hole. In the case of the OSD-specimen, the residual stresses of only 1 millimeter in depth are obtained. Every  $50 \mu\text{m}$  the strain can be obtained from the SGR, resulting in 20 stress measurements in 1 millimeter of depth. The principle of this method is shown in Figure 3.28.

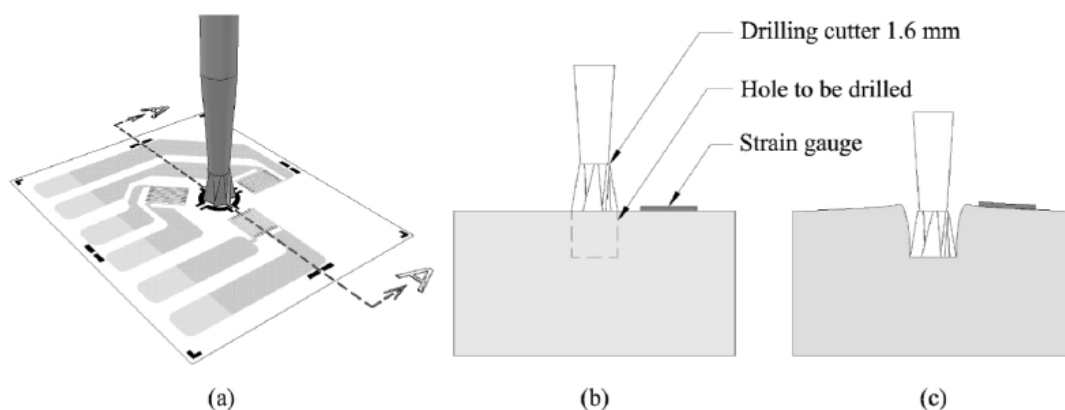


Figure 3.28: Principle of IHD measurement with tensile stress [25] (a) 3D-model with drill and SGR (b) cross-section before drilling (c) cross-section after drilling, stress/strain release

One OSD-specimen that was prepared has been analyzed with this method to obtain the magnitude of the residual stresses due to welding. On the specimen two groups of SGRs are placed, one called 'Left' and one called 'Right'. These will be compared to the results of the mechanical model. There were three measurements on the deck plate, one on the weld toe of the stiffener and one on the weld toe of the deck. These

measurement were all to a depth of 1 mm. Additionally, there was one measurement with a depth of 2 mm at one of the deck plate position. The positions of the strain gauges are shown in Figure 3.29.

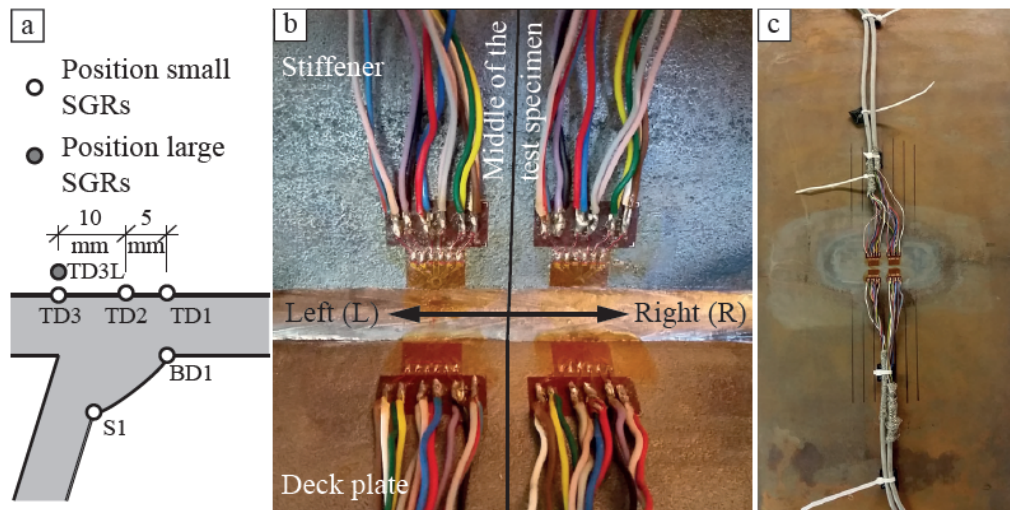


Figure 3.29: OSD-specimen residual stresses[25] (a) Location strain gauges (b) Close-up setup strain gauges (c) Overview strain gauges

The experimental data that has been described previously will be compared with the results from the mechanical model. In order to obtain the stresses at a certain point, a path with a length of 1 mm will be made in Abaqus® in order to obtain the residual stresses at the same point. However, the mesh size at the measured locations is 0.5 mm. This will result in only three points at which the residual stresses can be obtained. In contrast, the experimental data has every  $50\mu\text{m}$  a measurement, which results in a more flowing lines. The FEA results are only analysed in the middle of the specimen as the distance between the two groups has not been specified. The results of the experimental data and results of the mechanical models have been combined in Figure 3.30, 3.31 and 3.32.

In the thesis of W. Nagy [25] is described that the stresses obtained by the measurements of the experiment start at a very high compressive stress. This negative peak can be considered as a sort of singularity at the surface of the specimen. This singularity is caused by the surface preparation before placing the SGRs [25]. The stress should converge to a flat line at greater depth within the specimen. Therefore, the comparison between the FEA and the experimental data starts at a depth of 0.4 mm. The results of SGR TD3 can be ignored as the result does not converge. At that position, larger SGR's (TD3L) have been installed, which do converge. These can be used for the comparison between experimental data and the FEM-model. There is chosen to exclude the singularity close to the surface of the specimen in order to compare the experimental data with the FEM-model.

In the following section the residual stresses will be compared with the experimental data of W. Nagy. In the graphs all eight boundary condition variants are shown. However, in the written comparison below the focus lies only on variant BC7 and BC8 as these variants correspond well with the experimental data. In all graphs where the longitudinal stress (S33 z-direction) is analysed the yield stress of the material is denoted with a thin green line. In Figure 3.30 and 3.31, the deck plate results are shown. The residual stresses in the longitudinal direction are around the yield strength (355 MPa) in most of the FEM-models, while the experimental results are much lower around the 250 MPa. In the thesis of Nagy [25], it is stated that these stresses should be around the yield stress referring to chapter 4. In that chapter, W. Nagy has done a welding simulation model in FEM validated with experimental data on another geometry. The longitudinal stress in this analysis was around the yield strength in both the experiment as in the FEM-model. The results of this analysis is shown in Figure 3.33. Therefore, it is verified that the results of the FEA in this thesis correspond with the experimental data as the longitudinal residual stresses should be around the yield stress of 355 MPa. In the thesis of K. Spyridoni [34] the longitudinal stresses reached the yield stress at the same position, although the geometry was not identical to the geometry in this thesis. The transversal residual stresses of both BC7 and BC8 are slightly lower at the three deck plate positions, however this difference is considered acceptable.

In Figure 3.31 and 3.32, the results at both weld toes are shown. In comparison to the deck plate results, these results are closer to the experimental data. At the weld toe (BD1), the transversal residual stresses correspond well to the experimental data. The longitudinal residual stresses are slightly higher than the yield stress of the

material. This position is of great importance as the initial crack will be placed at the weld toe in the fracture model. Overall, it can be concluded that both variant BC7 and BC8 correspond well with the experimental data. In the fatigue crack simulation, the residual stress field of variant BC 8 will be used to obtain the effects of the residual stress field.

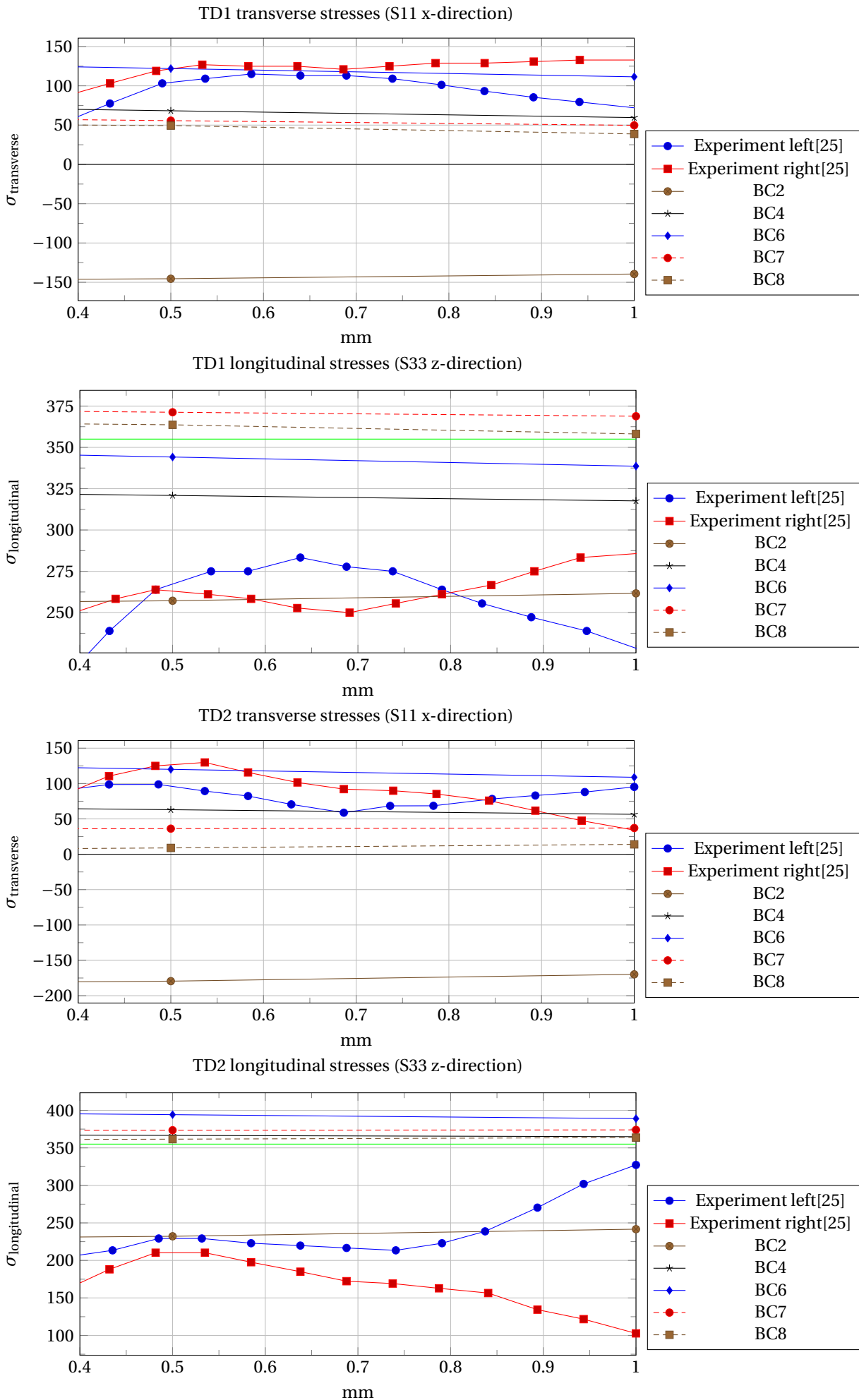


Figure 3.30: Comparison results weld deck plate [25]

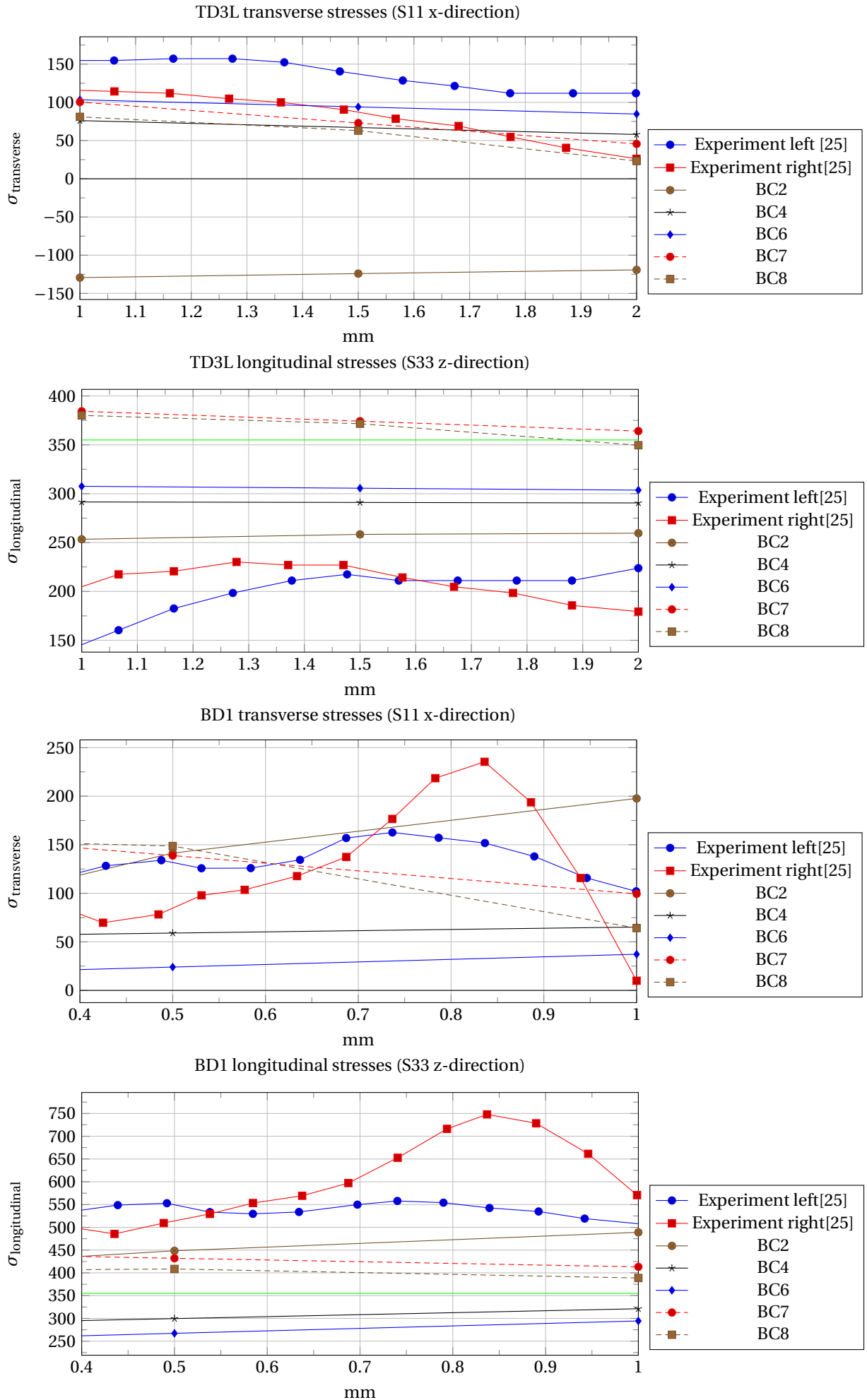


Figure 3.31: Comparison results weld toe deck and deck plate [25]

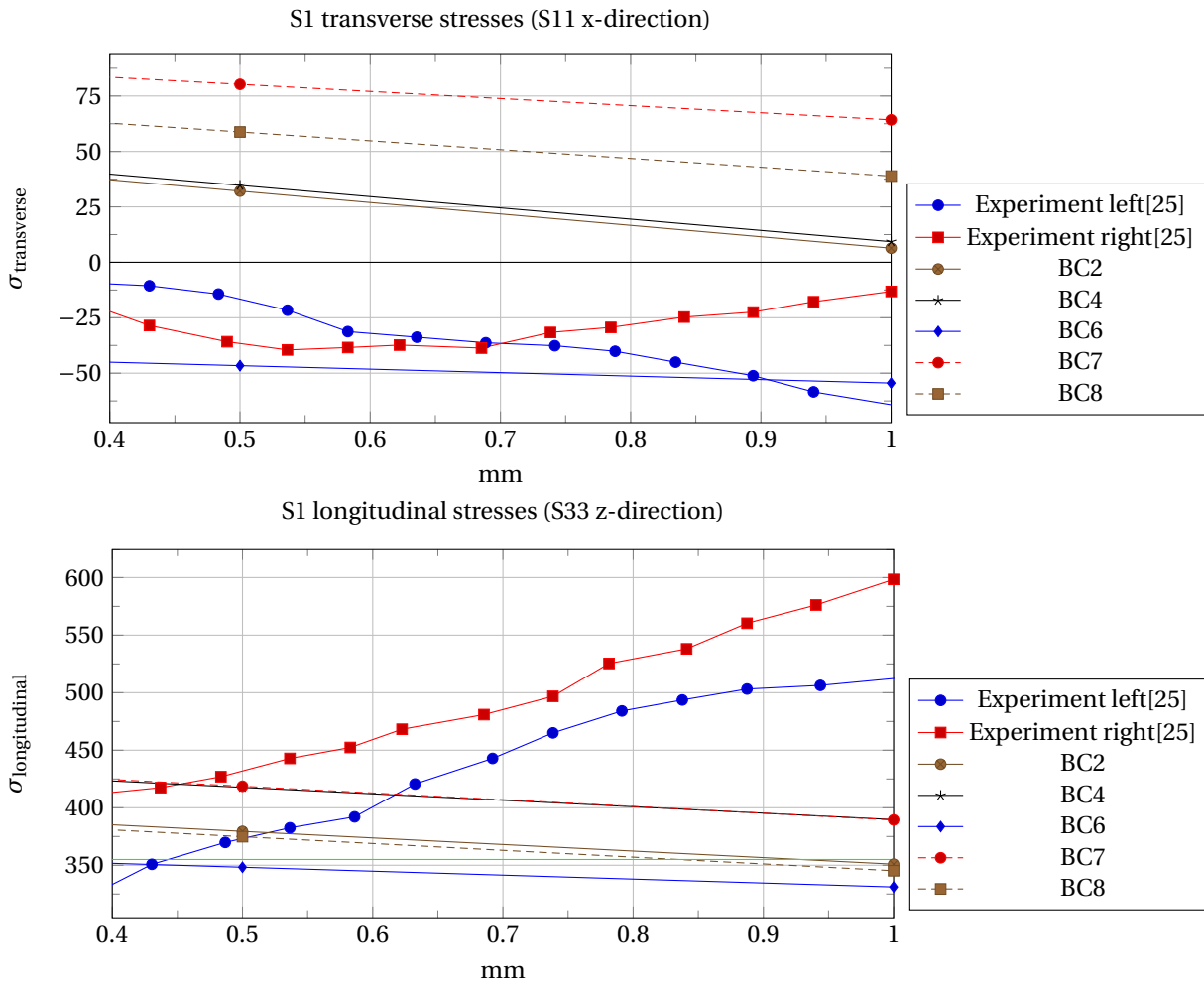


Figure 3.32: Comparison results weld toe stiffener [25]

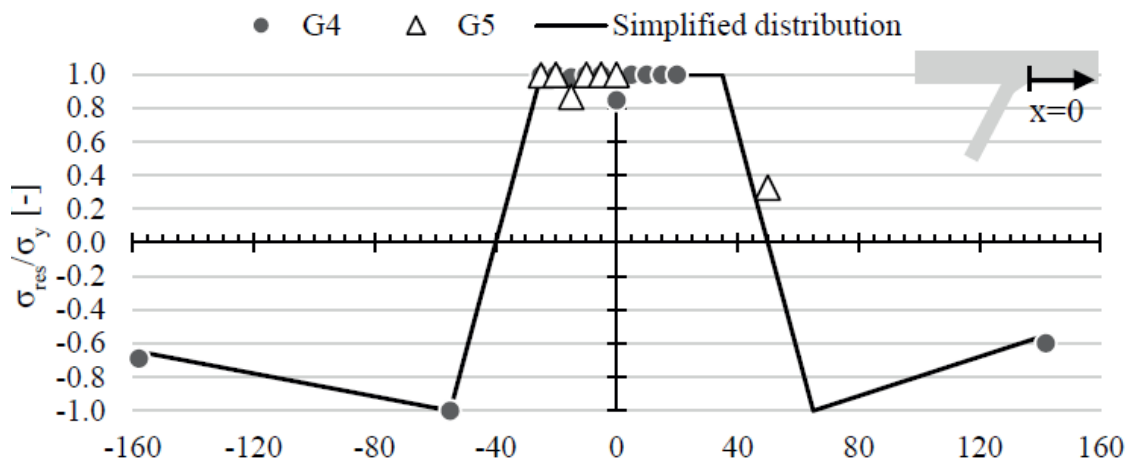


Figure 3.33: Results Chapter 4 longitudinal stresses top deck[25]

In Figure 3.34, the results of the mechanical analysis are compared to other similar experimental data of Kainuma et al. [20]. In this research the transverse residual stresses along the thickness of the deck at the weld root have been determined using both experimental data as FE-analysis. In this comparison, the FE-analysis performed in this thesis will be compared with both the FEA and experimental results. As the thickness's

of the deck and stiffener of both the experimental data and the FEM-model are different compared to the geometry used in this thesis, the relative thickness of the deck is used to compare the results. The transverse residual stress data from the experimental data is obtained using strain gauges along the deck thickness, while the transverse residual stress data of the FE-analysis is obtained directly from the FEM-software used by Kainuma et al.[20]. From the results of variant BC8, it can be seen that the mesh size in the middle of the deck is coarser compared to the top and bottom of the deck. The mesh on the top and bottom has a size of 0.5 mm in order to correctly compare with the experimental data of W. Nagy, while in the middle a mesh size of 3.67 mm is applied. Overall, the results of variant BC8 corresponds very well compared to both the FEA and experimental data of Kainuma et al. [20].

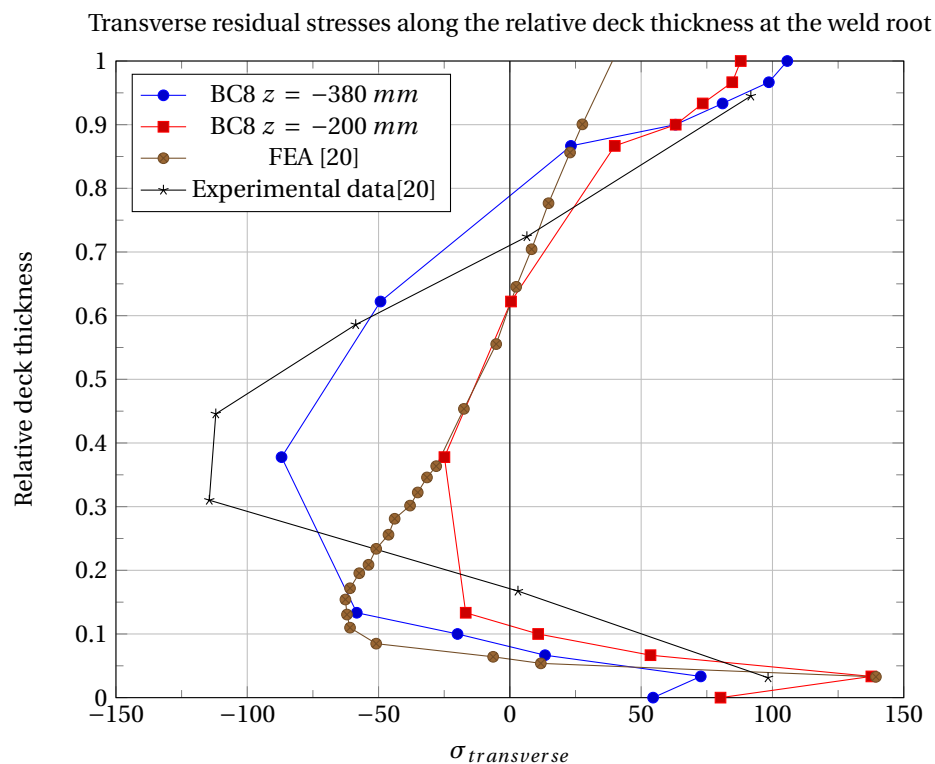


Figure 3.34: Comparison between FEA results and literature data [20]

### 3.2.7. Simplified residual stress field based on FEA

Based on the results of the mechanical model variant BC8, a simplification of the stresses in each direction is made. In Figures 3.35, 3.37 and 3.39 the simplified residual stresses are shown, while the FEA stress field output corresponding to these figures is shown in Figures 3.36, 3.38 and 3.40. The stresses are shown in the global axis system, so residual stress component S11 corresponds to the x-direction, residual stress component S22 to the y-direction and residual stress component S33 to the z-direction. As can be seen in the simplification of residual stress components S11 and S33, the stresses are not symmetrical everywhere. This is due to the asymmetrical geometry and the sequential weld sequence. The simplified stresses will be used in the crack propagation model, where the influence of the stresses in each direction will be analysed.

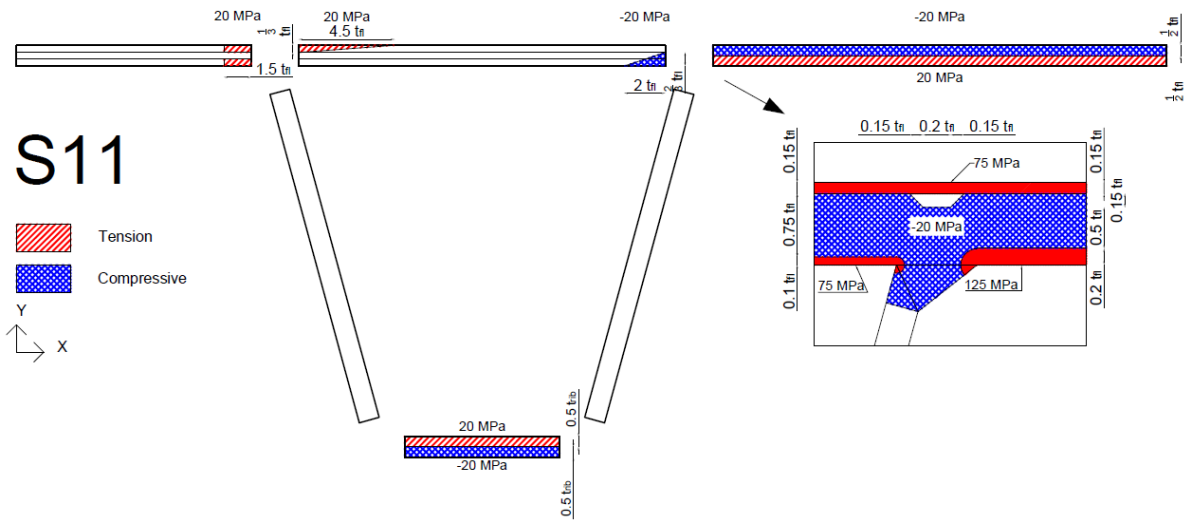


Figure 3.35: Simplified residual stress component S11 (x-direction)

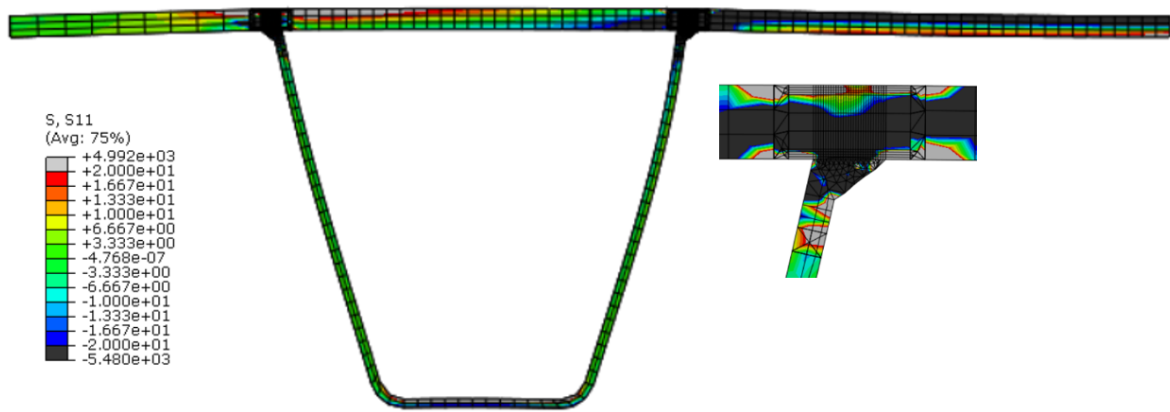


Figure 3.36: FEA residual stress component S11 (x-direction)

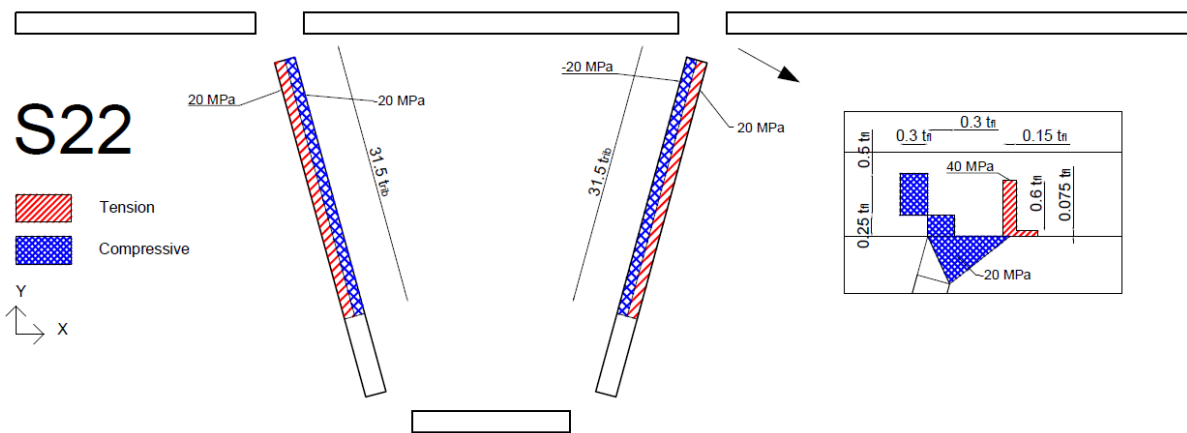


Figure 3.37: Simplified residual stress component S22 (y-direction)

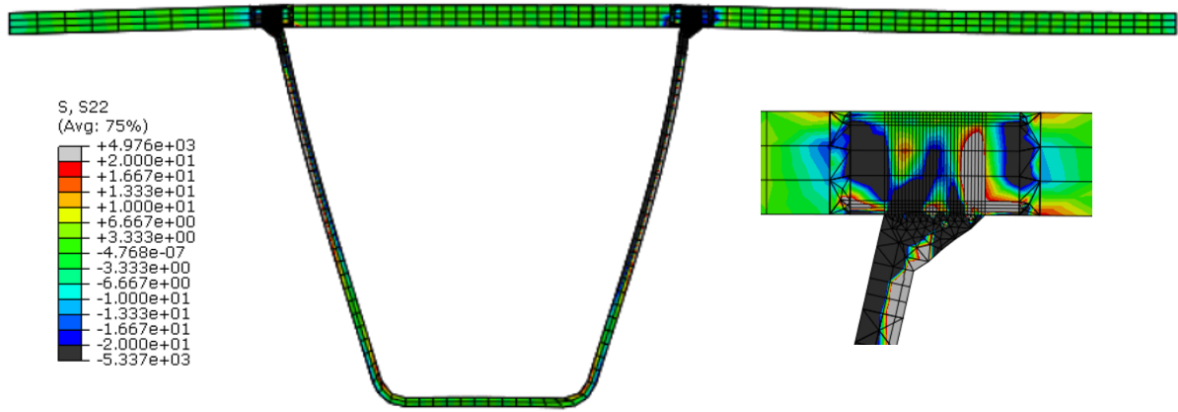


Figure 3.38: FEA residual stress component S22 (y-direction)

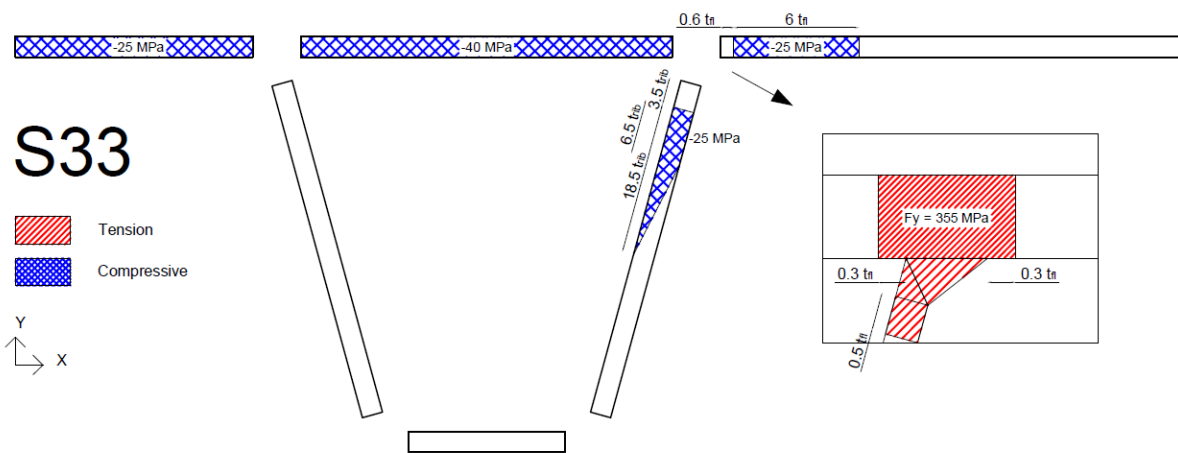


Figure 3.39: Simplified residual stress component S33 (z-direction)

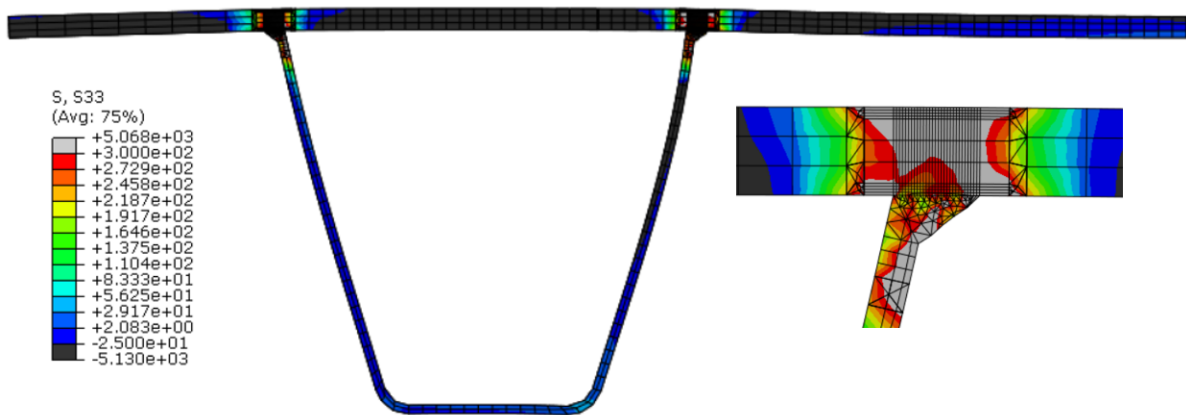


Figure 3.40: FEA residual stress component S33 (z-direction)

# 4

## Fatigue crack propagation simulation

In this chapter the fatigue crack growth simulation will be described. First, the model properties will be described. Next, a comparison between the FE-results and the static test data will be performed in order to verify the model. Thirdly, a parameter study has been performed towards the effect of the Paris law parameters, element types and element size on the crack propagation rate. At last, the fatigue crack growth simulation is described. A crack propagation analysis is performed using XFEM based on LEFM and VCCT. The results of the analysis will be compared with the experimental data of W. Nagy [25]. The analysis will include the residual stresses obtained by the weld simulation model in Chapter 3. The model with the residual stresses will be compared to a model without these stresses, in order to evaluate the effect of the residual stresses on the crack propagation.

During the fatigue crack propagation analysis a number of assumptions have been made in order to simulate the conditions of the experiment. These assumptions might influence the results in some extend. All assumptions are listed below in order to clarify which assumptions could influence the results.

- The boundary conditions do not correspond with the experiment exactly. This results in different stress and strain distribution around the crack region as been shown in section 4.1.3. The friction between the boundary conditions and the OSD-specimen has also not been modelled. The different stresses during the fatigue crack propagation analysis could result in different results.
- It is assumed that both the parent material and the filler material are the same according to the NEN-EN 1993-1-2 [26]. This can influence as the filler material might is influenced by the heat. Also the filler material can have different material properties. At last, the Paris law properties of the weld, could be different compared to the parent material. Also, this phenomena has been neglected in this analysis
- Due to the different boundary conditions between the mechanical model and the crack propagation model, the inserted residual stresses are not in balance during the fatigue crack propagation simulation. The changes in stress field can be small if the boundary conditions are similar.

### 4.1. Model properties

#### 4.1.1. Geometry of the model

As mentioned before the specimen used in this research will be identical to the specimen used in the research of W. Nagy [25]. The geometry of W. Nagy is shown in Figure 3.1. The experiment set-up is shown in Figure 4.1. The specimen has an depth of 400 mm. The specimen is supported by two supports at either side of the stiffener. At the left-hand side the specimen is supported by a clamped support, shown in Figure 4.3, with a length of 40 mm (x-direction). At the right-hand side the specimen is supported with a pinned support, shown in Figure 4.4, placed 50 mm away from the edge of the specimen. The deck has a thickness of 15 mm, while the stiffener has a thickness of 6 mm. At the deck the stiffener has a width of 300 mm, while at the bottom the width is 150 mm. The stiffener has a height of 275 mm. The loading of the specimen will be done using an hydraulic jack. This jack pushes down on a beam that has a round edge, which will result in a line load on the specimen. The line load is applied at 420 mm from the right edge of the specimen. The load beam

and the deformation of the specimen due to the loading is shown in Figure 4.2. The initial imperfections of the OSD-specimen and the uneven loading will not be taken into account in the FEM-model.

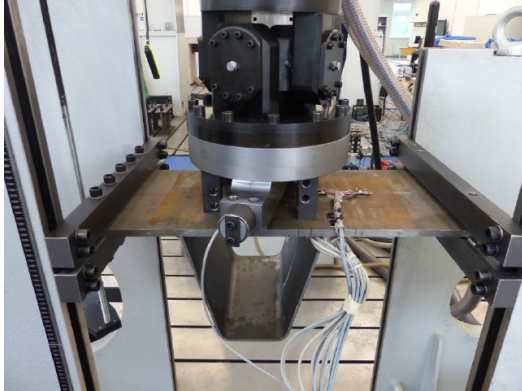


Figure 4.1: Experiment set-up OSD-specimen [25]

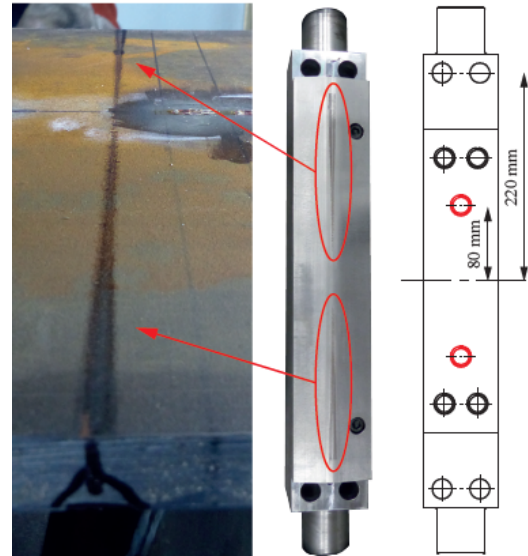


Figure 4.2: Loading condition OSD-specimen [25]

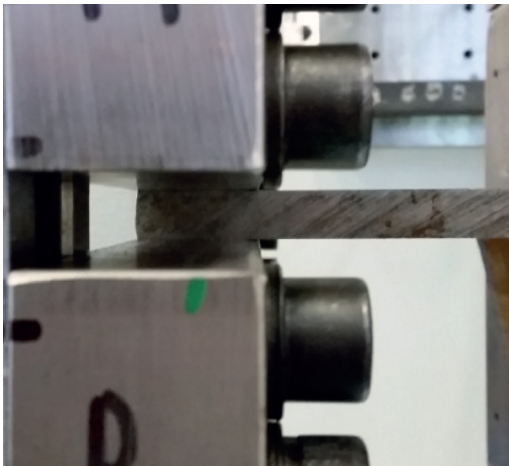


Figure 4.3: Clamped support OSD-specimen[25]



Figure 4.4: Pinned support OSD-specimen[25]

#### 4.1.2. Loading model

The loading model is divided into two parts, a static load and a periodic load. Both loads are line loads positioned 70 mm next to the weld root as shown in Figure 3.1. Within the FEM-model the load is modelled as a concentrated force at the earlier described reference point (RP-1).

The static load is there to verify the model compared to the experiment in terms of deformations, strains and stresses. Around the joint area, strain gauges are placed in order to capture the strains and stresses. The displacement of the OSD-specimen is obtained at the point of loading by the hydraulic cylinder that loads the specimen. These static experimental tests are done in increments of 10 kN with a maximum load of 40 kN. The static test in the FEM-model is only done at a load of 40 kN as the material properties within the model are linear elastic.

During the crack propagation analysis in Abaqus® a direct cyclic analysis will be performed. This quasi-static analysis simulates cyclic loading based on a varying load. The varying load is modelled using a periodic function in order to mimic the load cycle used by W. Nagy [25]. There is chosen to load the model with a force of -31 kN, which corresponds to specimen 10 [25]. The load of -31 kN is multiplied with a periodic function dependant of time in order to simulate cyclic loading. This periodic function, shown in equation 4.1, is a

function of time and amplitude. These parameters, shown in equation 4.2, are also used by W. Nagy [25]. The total load on the OSD-specimen is shown in Figure 4.5. The loading ratio  $R = \frac{Load_{min}}{Load_{max}}$  is therefore zero, while the frequency is 1 Hz. The load is applied in the negative y-direction, and evenly spread over the line to represent a line load.

$$y = A_0 + A_1 \cos(t - t_0) + B_1 \sin(\omega(t - t_0)) \quad (4.1)$$

$$y = 0.5 + 0 \cos(t - 0.5) + 0.5 \sin(2\pi(t - 0.5)) \quad (4.2)$$

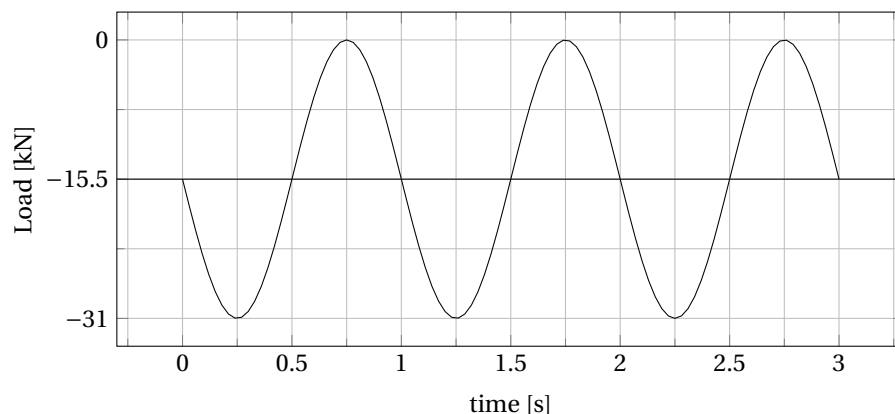


Figure 4.5: Direct cyclic load

### 4.1.3. Boundary conditions

The boundary conditions (BC) will influence the stress distribution of the FEM-model greatly. Therefore it is important to model the boundary conditions as close to the boundary conditions in the experiment, shown in Figures 4.1, 4.2, 4.3 and 4.4. The influence of the boundary conditions are investigated using a small parametric study. In the first variant, denoted as BC1, the experimental boundary conditions will not be modelled. The boundary conditions of the FEM-model will be applied directly to the OSD-model. While in the second variant, denoted as BC2, the metal beams that define the boundary conditions in the experimental set up are modelled in the FEM-model. In this way the deformation of the beams that form the boundary conditions are modelled in the FEM-model. Both FEM models are shown in Figures 4.6 and 4.7.

At the left edge of variant BC1, 40 mm of the OSD-specimen is restricted in its deformation in all six directions and rotations ( $U_1, U_2, U_3, UR_1, UR_2, UR_3=0$ ). The line load is applied using a reference point (RP-1). This reference point is kinematically coupled to a line along the specimen in order to simulate a line load [15]. At 50 mm from the right edge of the OSD-specimen, both the top and bottom are restricted in the y-direction ( $U_2=0$ ).

At the the left edge of variant BC2, two square steel beams with a dimension of 40 mm are positioned on both sides of the OSD-specimen. The beams have both a length of 440 mm, so these exceed the OSD-specimen with 20 mm at both sides. Both end surfaces of the beams are restricted in all six directions and rotations ( $U_1, U_2, U_3, UR_1, UR_2, UR_3=0$ ). Within Abaqus® surface-to-surface contact is applied to simulate the interaction between the beams and the OSD-specimen. The friction coefficient between the surfaces is 0.3. At the right edge the same square beams with a dimension of 40 mm are applied. However a half circle with a radius of 5 mm is applied where the beam makes contact with the OSD-specimen. This half circle will simulate a pinned connection of the OSD-specimen. Both end surfaces of the beams are restricted in all three directions ( $U_1, U_2, U_3=0$ ). Again both beams have a length of 440 mm. Also the surface-to-surface contact is applied to simulate the interaction between the half circles of the beams and the OSD-specimen. The friction coefficient between the surfaces is 0.3. The loading is applied using one square beam with a length of 440 mm under which a triangular shaped part is attached. The edge of the triangle that makes contact with the OSD-specimen has a radius of 1 mm. The load is applied on centre of the top surface of the beam over a length of 250 mm. This is done as the hydraulic cylinder is only connected to a part of the loading beam. Both end surfaces of the beams are restricted in every direction except for the y-direction in which the load is applied ( $U_1, U_3, UR_1, UR_2, UR_3=0$ ). Also the surface-to-surface contact is applied to simulate the interaction between triangle of the beam and the OSD-specimen. The friction coefficient between the surfaces is 0.3.

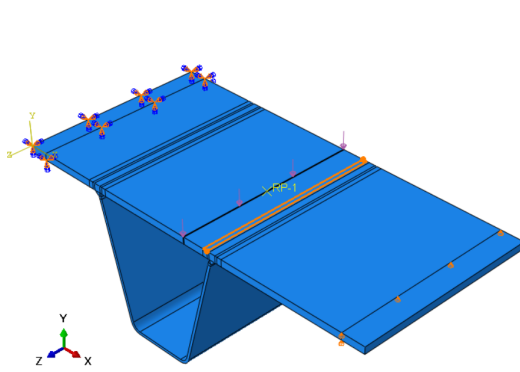


Figure 4.6: Boundary condition variant 1 (BC1)

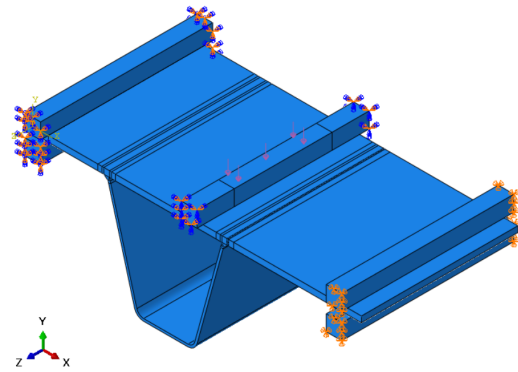


Figure 4.7: Boundary condition variant 2 (BC2)

#### 4.1.4. Material Properties

As the used method is Linear Elastic Fracture Mechanics (LEFM), linear material properties are used in the FEM-model. The E-modulus = 210 GPa and the  $\nu = 0.3$ . It is assumed that both the weld and the parent material have the same material properties. Also Paris Law parameters are defined in the model as these are required in the fatigue crack propagation analysis. The Paris law properties  $C_3$  and  $C_4$  are based on the literature data of W. Nagy [25], while the fracture toughness parameters are based on other literature [4] as these were not specified in the data of W. Nagy. Parameters  $C_1$ ,  $C_2$  and  $\frac{G_{thresh}}{G_c}$  are set very low in order to immediately start the crack propagation phase. The  $\frac{G_{pl}}{G_c}$  is set at 0.85 based on literature data[15], at 0.85 times the fracture toughness unstable crack growth occurs. The Paris law parameters are shown in Table 4.1.

Load	$C_1$	$C_2$	$C_3$	$C_4$	$G_I$	$G_{II}$	$G_{III}$	$\alpha_{m/n/o}$	$\frac{G_{thresh}}{G_c}$	$\frac{G_{pl}}{G_c}$
-31 kN	0.001	0	$3.00 * 10^5$	1.5	6.3	6.3	6.3	1	0	0.85

Table 4.1: Load and Paris law parameters [4, 25]

## 4.2. Comparison FE results with the static test data

A static FE-analysis is performed in order to verify if the stresses and strains of the experimental data[25] correspond with the FEA model. During this experiment the OSD-specimen is with a varying load ranging from -40 kN to 40 kN. As the model is linear elastic, the specimen is loaded once with a load of - 40 kN. The rest of the values will be extrapolated where necessary.

### 4.2.1. Deformation

In this section, the deformations of the experiment will be compared with the FEA of this research. This is shown in Figure 4.8. Both variants of the boundary conditions are compared with the experimental data. The first variant, denoted as BC1, is much stiffer compared to both the experiment as the second variant, denoted as BC2. Variant 2, denoted as BC2, has a slightly higher deformation compared to the experimental data, while variant 1 has a lower deformation. The difference in deformation is caused by the different boundary conditions. The boundary conditions of BC2 are less stiff due to the surface-to-surface contact, while the boundary conditions of BC1 are much stiffer due to infinitely stiff boundary conditions. Overall the both FEA correspond well with the experimental data as the difference is minimal.

### 4.2.2. Strain comparison

In this section, the strain between the experimental data of W. Nagy [25] and both FEM-models described in this thesis. The strain is analysed in the longitudinal direction (z-direction) of the OSD-specimen. The strains are both analysed at a distance of 25 mm from respectively the weld toe and weld root. Also the strains are measured in the middle of the specimen.

The comparison between the experimental data [25] and the FEM-model are shown in Figures 4.9 and 4.10. The strains along the deck of FEM-model BC2 are similar compared to the experimental data. While the strains along the stiffener of FEM-model BC2 are comparable to the experimental data, although not as close as along the deck. Variant 1, denoted as BC1, has stiffer boundary conditions, which results in lower strains at

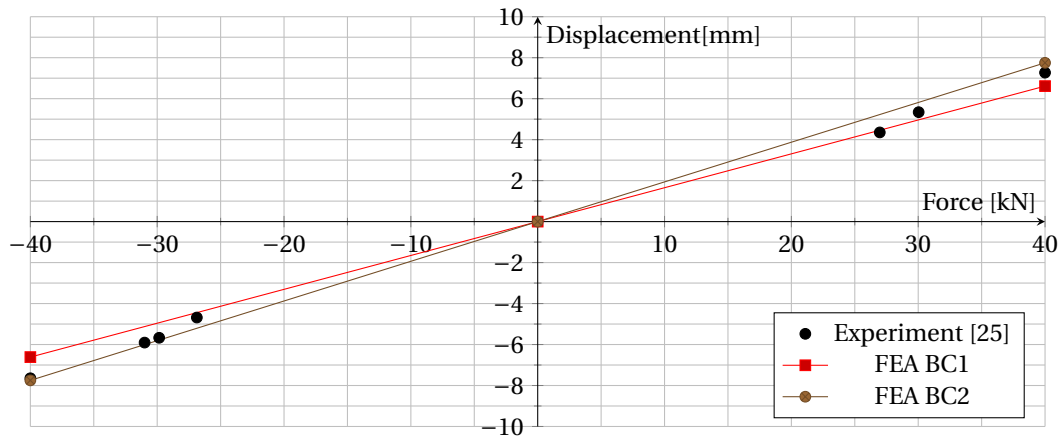


Figure 4.8: Deformation

the measured positions. The stiffer boundary conditions of BC1 result in lower strain levels at both the weld root and toe, especially the the clamped support is stiffer compared to the experiment. Due to the 'surface-to-surface' contact applied in BC2, the clamped support is not completely fixed as the specimen can slip slightly as the line load is applied. This slippage results in less stiff boundary conditions which increases the strains at the measured position.

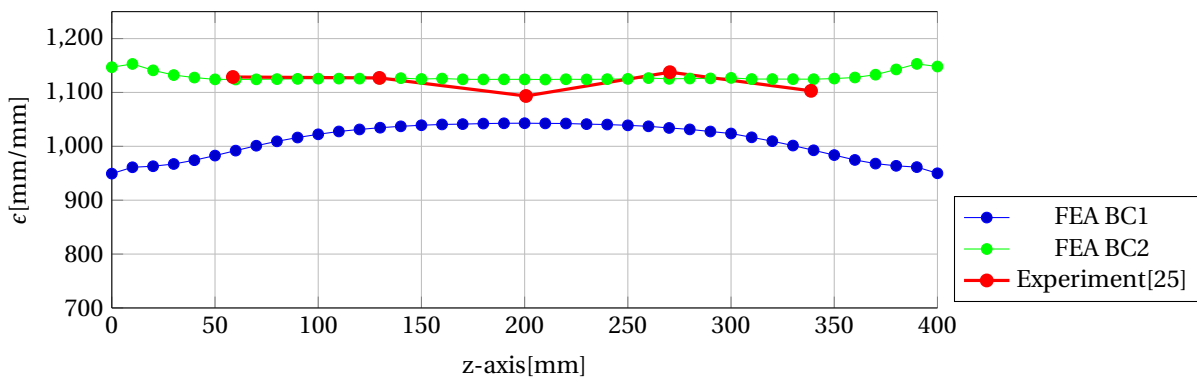


Figure 4.9: Strain deck

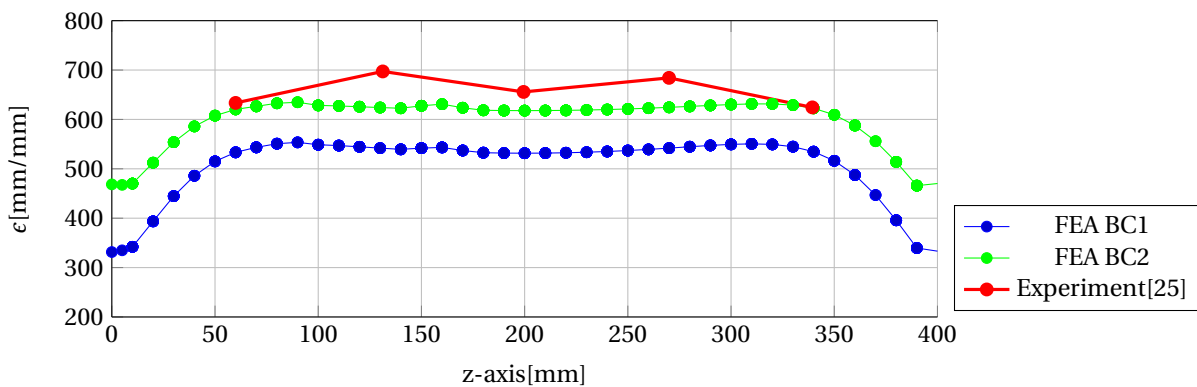


Figure 4.10: Strain stiffener

### 4.2.3. Hot spot stresses

In this section the hot-spot stresses between the experimental data of W. Nagy [25] and both FEM-models described in this thesis. The stress is analysed in the transversal direction (x-direction) of the OSD-specimen. Also the stresses are analysed in the middle of the specimen.

The comparison between the experimental data [25] and the FEM-model are shown in Figures 4.11 and 4.12. The Hot Spot Stresses (HSS) at the weld toe along the deck are comparable between the two FEM-models and the experimental data. Variant one (BC1) is slightly closer to the experimental data compared to variant two (BC2). The HSS at the weld root along the stiffener are comparable between the FEM-model and the experimental data. Especially, the variant two (BC2) follows the trend of the experimental data closely. Variant one (BC1) deviates more compared to the experimental data. Both FEM-model show a singularity close to both the weld root and weld toe.

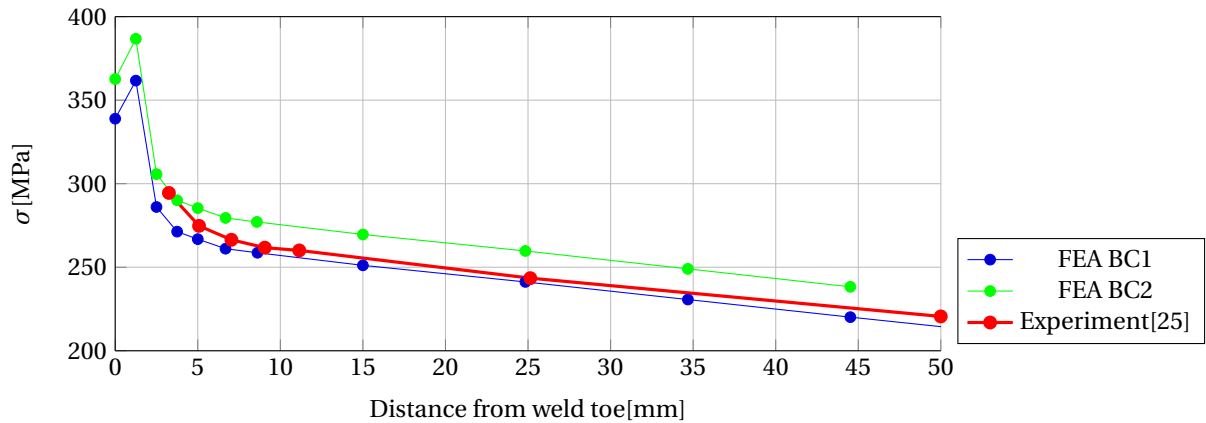


Figure 4.11: Hot spot stress weld toe deck

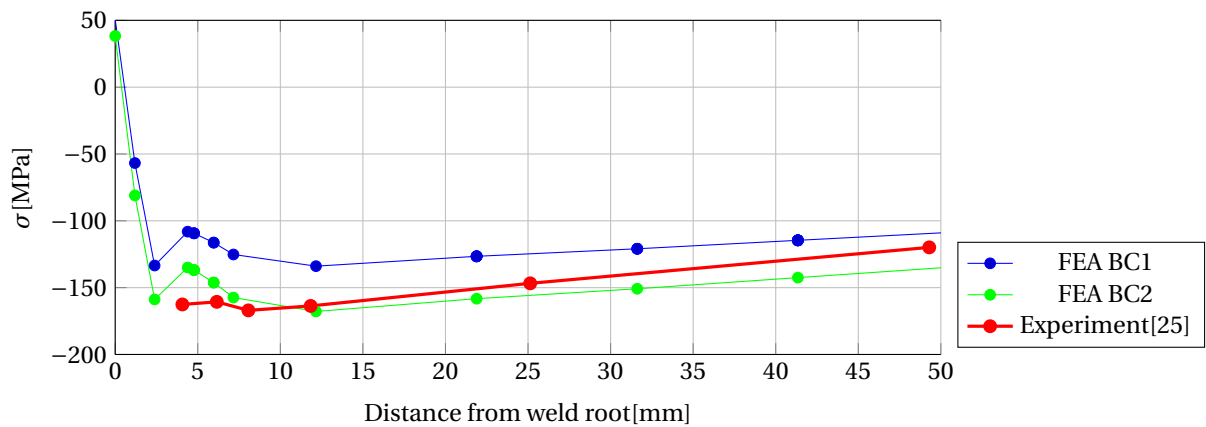


Figure 4.12: Hot spot stress weld toe stiffener

## 4.3. Parameter study

A parameter study has been performed in order to get a better understanding of the Paris law parameters on the crack propagation rate of an OSD-specimen. The various parameters, described in section 2.4, will be changed independently from each other in order to obtain the influence of each parameter. Also effects of both the element types and element sizes will be analysed in this parameter study.

### 4.3.1. Base model

The model used for this parameter study is the same as in the whole research and shown in Figure 3.1. Only the mesh has not been refined in order to reduce computing time. The results do not need to be realistic as only the influence of the parameters will be analysed. The initial crack size, shown in Figure 4.13, has also

been increased in order to match the increased mesh size. Element type C3D8, with a size of 1.5 mm, has been used in the enriched crack region. The initial crack has a width of 5 mm and a height of 1 mm. The crack is inserted in the middle of the specimen ( $z = -200$  mm) at the weld toe, as shown in Figure 4.14, where the crack is denoted in red. In terms of the Paris Law parameters there is chosen to use the parameters shown



Figure 4.13: Crack geometry parameter study

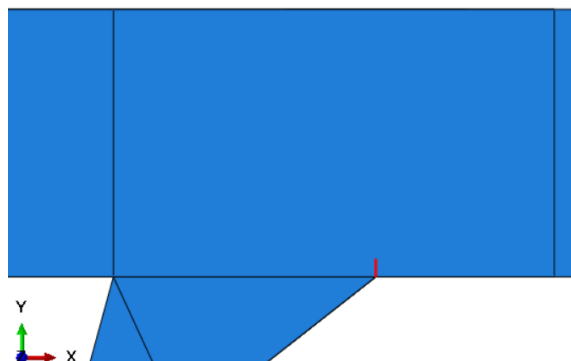


Figure 4.14: Crack location parameter study

in Table 4.2. The load is the same as described in section 4.1.2. This load consist of a dynamic cyclic load of -31 kN applied at reference point 1 (RP-1). Both parameters  $C_3$  and  $C_4$  are based on the research of W. Nagy [25] and derived using the formulas described in section 2.4. The mixed mode model parameters are based on literature[4] as the parameters are not specified in the report of W. Nagy. The Paris law and mixed mode model parameters will be varied in the parameter study. The parameters will be varied three times: the base value, a higher value and a lower value. The difference per value is determined per parameter.

Paris Law parameter study						
Load	Paris law components		Mixed mode model			
	$C_3$	$C_4$	$G_I$	$G_{II}$	$G_{III}$	$\alpha_{m/n/o}$
-31 kN	$5.00 * 10^{-5}$	1.5	6.3	6.3	6.3	1

Table 4.2: Paris Law parameters

#### 4.3.2. $C_3$ -parameter

First, the  $C_3$ -parameter will be analysed. This parameter is primarily related to the toughness of the material. The parameter will be varied between  $2.5 * 10^{-5}$  and  $10 * 10^{-5}$ . The results of the three models is shown in Figure 4.16. The difference between the three different values is substantial. The higher the  $C_3$ -parameter, the faster the crack propagation. However, the trend of each line stays the same.

#### 4.3.3. $C_4$ -parameter

Next, the  $C_4$ -parameter will be analysed. This parameter is also related to the toughness of the material. In this analysis four different values have been analysed, ranging from 0.5 to 2. The results of the four models is shown in Figure 4.16. The difference between the four different values is relatively small. It can be noticed that the smaller the  $C_4$ -parameter is, the steeper the slope of the graph is. The crack does not propagate faster when the parameter is lower, as in the early stage of crack propagation is slower.

#### 4.3.4. $G$ -parameter

Next, the  $G$ -parameter will be analysed. This parameter is also related to the toughness of the material. In this analysis four different values have been analysed, ranging from 3.8 to 11. The results of the three models is shown in Figure 4.17. The difference between the three different values is negligible. As the crack propagation analysis primarily falls in the "Paris region", the crack propagation results are primarily influenced by the  $C_3$  and  $C_4$  parameters. Based on the theory in section 2.4, a change in this parameter will influence the results when unstable crack growth occurs at failure of the structure.

### 4.3.5. Element type

Fourthly, the element types will be analysed. Two different element types will be analysed with the base parameters. Only the elements in the enriched region are changed. The base element, a C3D8 linear brick element, will be replaced by a tetrahedron element (C3D10). Both elements are shown in Figure 4.15. The results of the two models is shown in Figure 4.17. The brick element propagates relative linear, while the tetrahedron element propagates in two distinct phases. The trend of the graph using the tetrahedron element complies more with the results of W. Nagy. It also must be noted that both W.Nagy as R.S. Gupta used tetrahedron in their enriched region. However these elements have the disadvantage that they require more computing time compared to linear brick elements.

### 4.3.6. Element size

In Figure 4.18, the results of the parameter study towards the element size is shown. Both element types have been analysed using various element sizes. The element size using linear brick elements (C3D8) seems to have no significant differences in crack propagation rates. While the tetrahedron elements will propagate faster with smaller element sizes. Only two analyses have been performed with the C3D10 elements as smaller element size will consume too much CPU time.

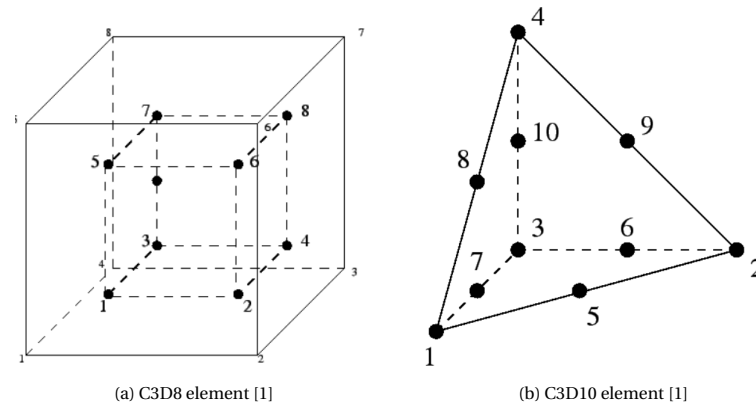


Figure 4.15: Elements parameter study

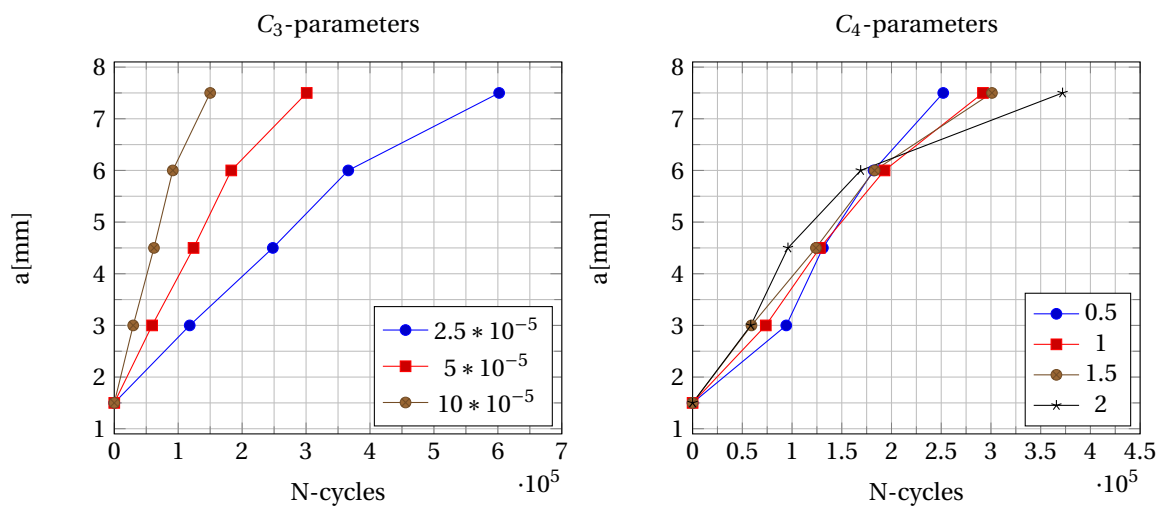


Figure 4.16: Parameter study C<sub>3</sub> and C<sub>4</sub> parameters

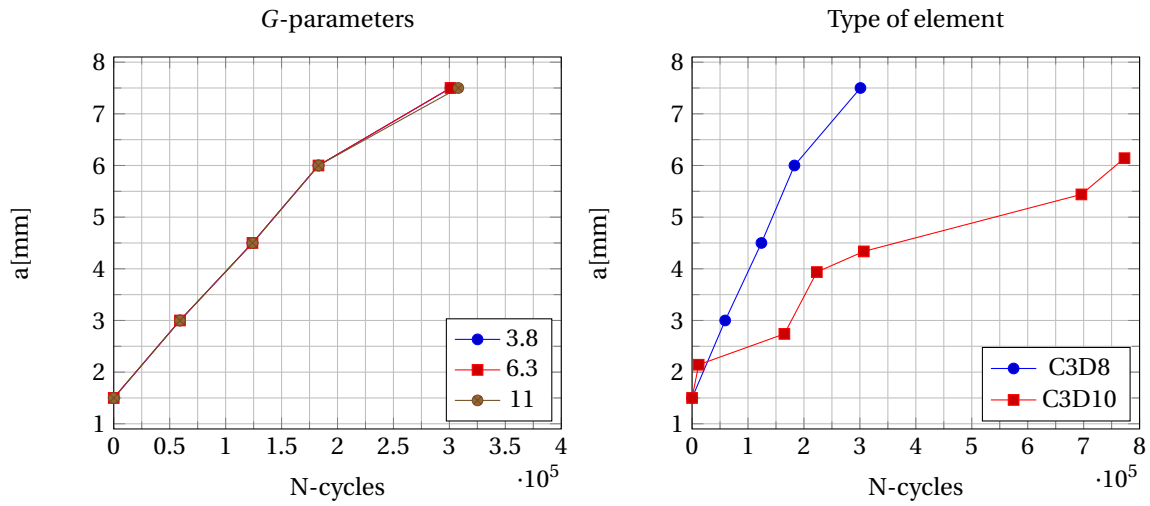


Figure 4.17: Parameter study G-parameter and element types

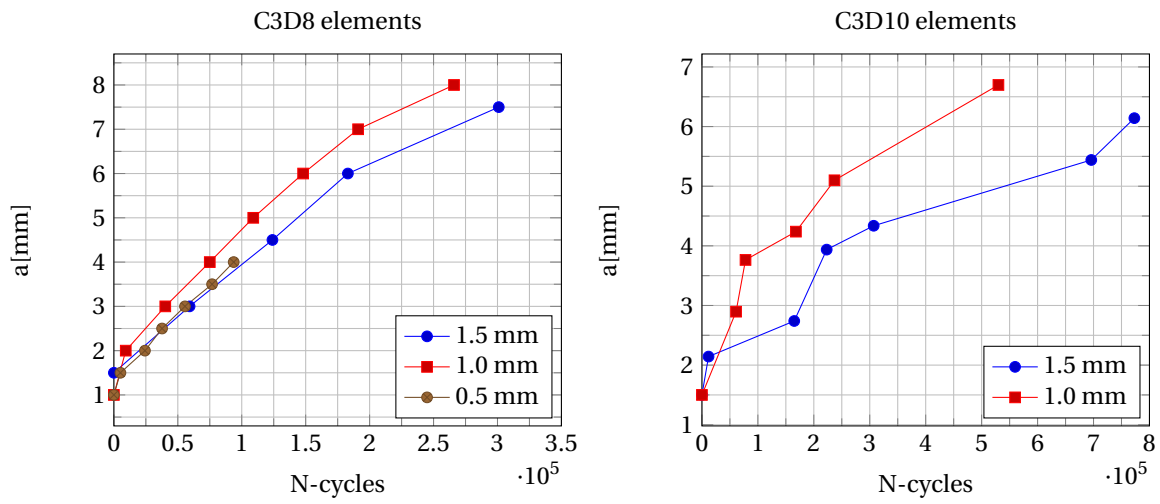


Figure 4.18: Parametric study element size

## 4.4. Fatigue crack propagation simulation

In this section the crack propagation model will be described. Within this chapter the crack propagation rate based on fatigue loading will be modelled. The XFEM-model will replicate a fatigue experiment [25] of W. Nagy. Within this experiment both the fatigue loading as the crack propagation of a OSD-specimen is monitored.

Both the initial crack size in depth, denoted as  $a$ , and the length of the crack, denoted as  $2c$ , are measured using beachmark measurements and fractographic analysis. These experimental data are used to compare the FEM-model. Also an XFEM analysis has been performed by W. Nagy. However this analysis uses another method based on stress intensity factors (SIF). Therefore this analysis is ignored in the comparison as it uses another method.

The initial crack, shown in Figure 4.19, will be placed at the same position as in the parameter study, shown in Figure 4.20. The initial crack shape has a rectangular shape where the crack depth is denoted as  $a$ , the half length of the crack is denoted as  $c$  and the total crack length is denoted as  $2c$ . The initial crack size is based on experimental data of W. Nagy. This data is shown in Figures 4.22 and 4.23. The initial crack size is based on Figure 4.23 where the crack depth is around 1.5 mm and the total crack length is around 275 mm. This corresponds to around 170 000 cycles in Figure 4.22. This concludes that the XFEM model will propagate the initial crack from 1.5 mm until failure. The initial phase of the crack propagation will not be modelled as there is no experimental data available on the crack length in this phase. Both graphs are based on beachmark measurements of specimen 10.

### 4.4.1. BC2-variant

In section 4.1.3, variant BC2 is described, in which the test set-up is modelled. The interface between the OSD-specimen and the set-up has been modelled using 'surface-to-surface'-contact. Currently it is difficult to use this type of interaction with a direct cyclic analysis, as the deformation during this analysis is too large for the 'surface-to-surface'-contact. This implies that a crack propagation simulation is not possible using this type of model. Therefore, there are no results of model variant BC2 available as the model needs to be improved in future research.

### 4.4.2. Mesh

The mesh around the weld region is shown in Figure 4.21. The mesh has been refined around the weld area. In the enriched region around the crack zone, linear hexahedron (C3D8) elements with a size of 0.75mm are applied. In between the refined and non-refined mesh tetrahedron (C3D10) elements have been applied to transition in element type and size. For the rest of the non-refined mesh, linear hexahedron (C3D8R) elements are applied with a global size of 10 mm.

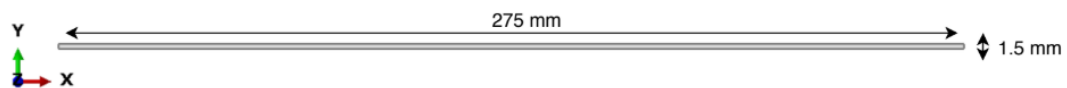


Figure 4.19: geometry initial crack

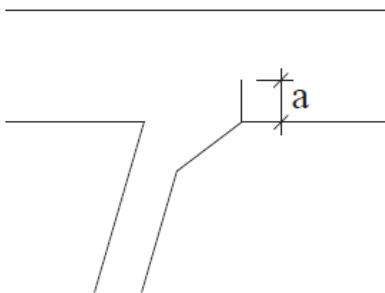


Figure 4.20: Shape and position initial crack [25]

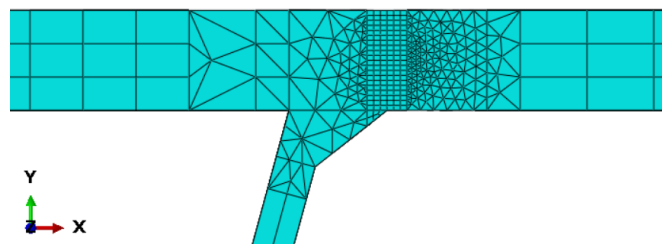


Figure 4.21: Mesh fatigue crack simulation model [25]

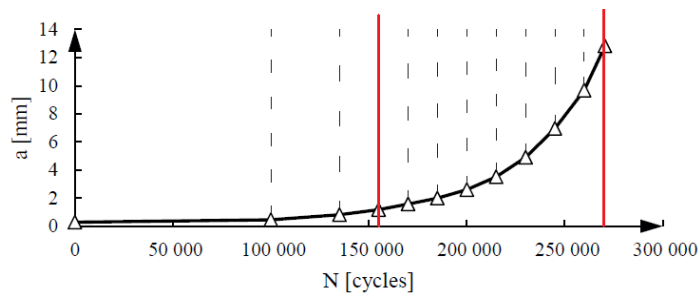


Figure 4.22: Initial crack depth Specimen 10 [25]

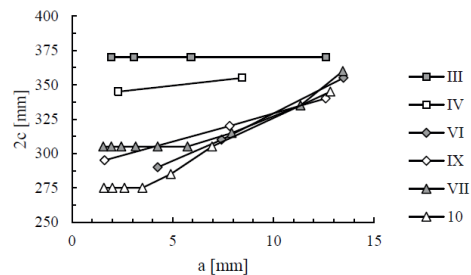


Figure 4.23: Initial crack length Specimen 10 [25]

#### 4.4.3. Residual stresses

In order to obtain the influence of the residual stresses on the crack propagation, the stresses due to the welding are inserted in Abaqus® with the function 'Predefined Field'. This function allows insertion of a stress at the initial step of the FE-analysis. The simplified residual stresses, described in section 3.2.7, are inserted into the fracture model. This method has both advantages and disadvantages. The advantage of using this method, is that the residual stress field can be accurately inserted onto the mesh of the fracture model. Also the residual stress field will change due to the crack propagation. For example if there is a residual tensile stress around the crack area and the crack propagates, this tensile stress will be released due to the propagating crack. Other methods, used for example by W. Nagy, used a separate Stress Intensity Factor,  $K_{res}$ , in order to include the influence of the residual stresses [25].

The disadvantage of the applied method is that in most cases the boundary conditions of the mechanical weld model and the crack propagation model are different. This has the result that after the stresses are inserted into the crack model, the stresses might not be in equilibrium due to the different boundary conditions. After the first static analysis the stress field might change due to the different boundary conditions. The changes in stress field can be small if the boundary conditions are similar. Also due to the inserted stress and difference in boundary conditions, the OSD-specimen will deform slightly due to the unbalanced stresses.

#### 4.4.4. Results

The XFEM-model will be compared with the experimental results of W. Nagy [25]. First, the results will be analysed using the graphs which show the trend of the crack propagation simulation compared to the experimental data. Which is followed by comparing the finite element analysis to the experiment in terms of statistics. In both comparisons the effects of the residual stresses on the crack propagation will be analysed. The results of the FEA with and without residual stresses are shown in Figure 4.24, 4.25 and 4.26. Each residual stress component, S11, S22 and S33, which corresponds to the residual stresses in x-, y- and z-direction, is introduced into the XFEM-model separately in order to obtain the effects of the residual stress components. The crack propagation rate of the base model is slightly faster compared to the experiment. However, the trend of the graph is comparable with the experiment until around 6mm of crack depth. The crack propagates slower compared to the experiment after 6mm of depth in the base model (no residual stresses). It can be noticed that the base FEA and the FEA including all residual stress components, propagates further compared to the other models. Computation to the failure requires much more CPU-time compared to the S11, S22 and S33 FEM-models. Therefore, it is chosen to compute only the base model and the model including all three residual stress components. It can be assumed that the other models will show continuous trend as the base FEA and the analysis including all three stress components.

The crack length ( $2c$ ) of the base model is comparable till around  $2.35 \cdot 10^5$  cycles. After this amount of cycles the experiment propagates to around 345 mm in length, while the FEM-model only slightly propagates in this direction. At last, it can be seen in Figure 4.26 that the crack shape between the experiment and the crack simulation analysis is similar. The overall crack shape including the residual stresses does not significantly differ between all the XFEM-models.

The imported residual stress component S11 results in a higher crack propagation rate in terms of crack depth, which is caused by the tensile stress around the weld toe. In the first phase of the crack propagation, the rate of propagation is accelerated as the tensile stress component opens the crack. As the crack propagates towards the region of compressive residual stresses, the crack propagation rate slows down. At the end of the analysis, the relation between the load cycles and the crack depth is similar compared to the base model. The residual stress component S11 on the crack length ( $2c$ ) results in a higher crack propagation

rate. However, the results are still not fully consistent to the experimental data.

The inserted residual stress component S22 results in a slightly higher crack propagation rate, which is likely caused by the tensile stress around the initial fracture in the OSD-specimen. Over the whole analysis, the crack propagation rate is higher compared to the base model. Residual stress component S22 does not have a significant effect in terms of crack width as the data is comparable with the base XFEM-model without residual stresses.

The imported S33-stresses result in a slower crack propagation rate, which is likely caused by the tensile stress around the weld zone. As residual stress component S33 is parallel to the crack length, these tensile stresses in the z-direction, close the crack and therefore it requires more cycles, to propagate the crack. Residual stress component S33 results in a lower crack propagation rate in terms, as the specimen hardly propagates in the length.

The FEA, including all three residual stress components, follows the experimental data rather closely, especially between 1.5 mm and 3.75 mm of crack depth. After this crack depth, the crack propagation rate is lower compared to the experimental data. At around 265.000 cycles the FEM-model stopped converging. The moment of failure is around the same number of cycles. Around 235.000 cycles the crack propagation rate is lower compared to the experiment until the point of failure. This can be explained by the perfect material used in FEM-model and therefore the model fails in a few load cycles. In reality, there are small imperfections which declare the steadier crack propagation trend at failure. The results of the crack length are between residual stress component S11 and the base FEA and do not correspond well to the experimental data. This needs further studies. At last, no significant change is visible comparing this model to the benchmarks or other models.

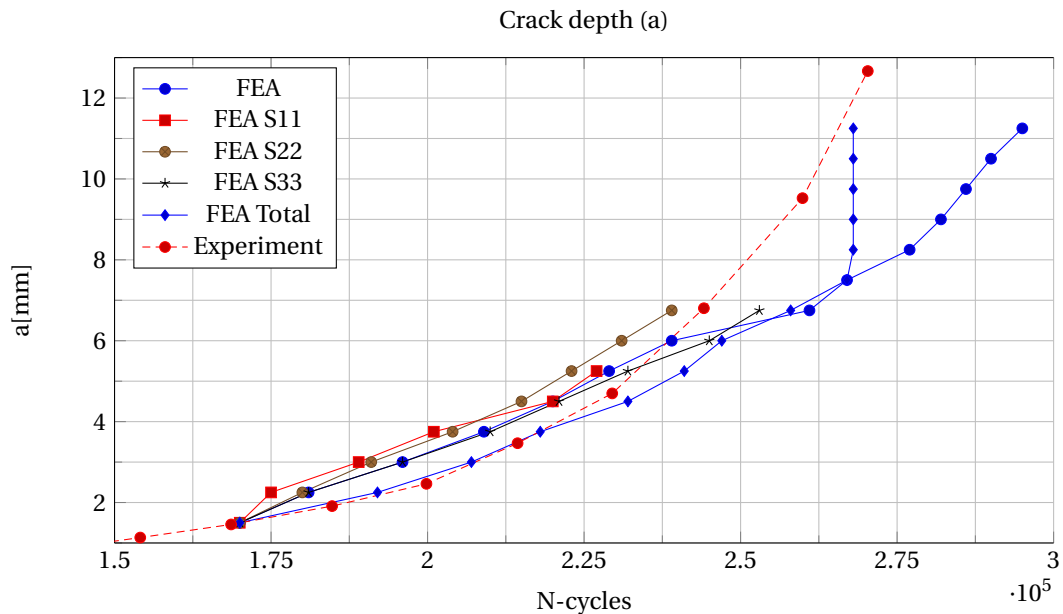


Figure 4.24: Results fracture models crack depth

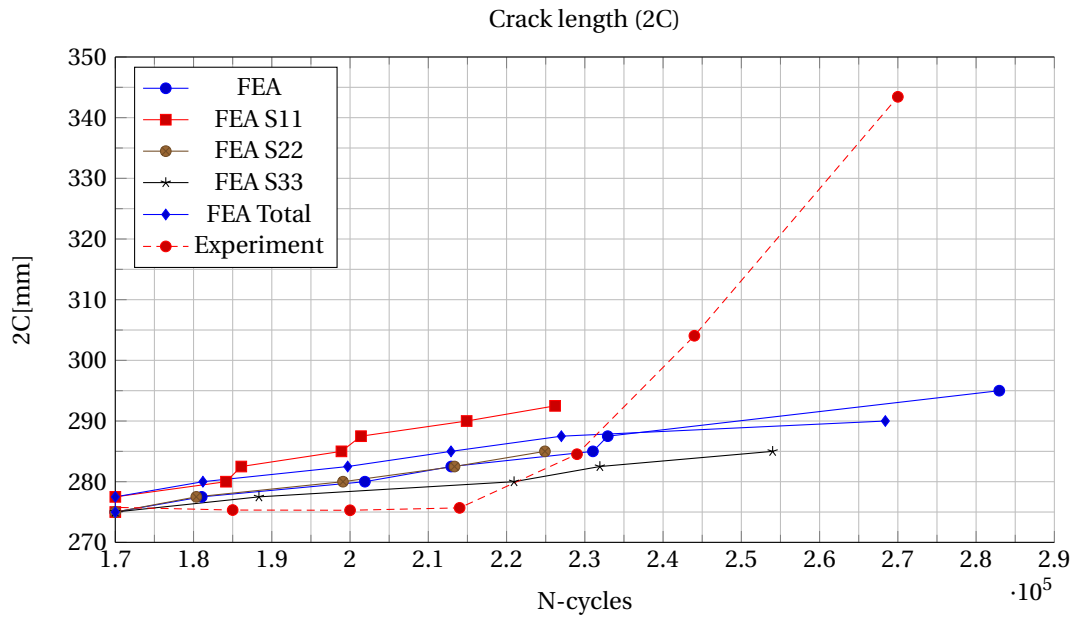


Figure 4.25: Results fracture models crack width

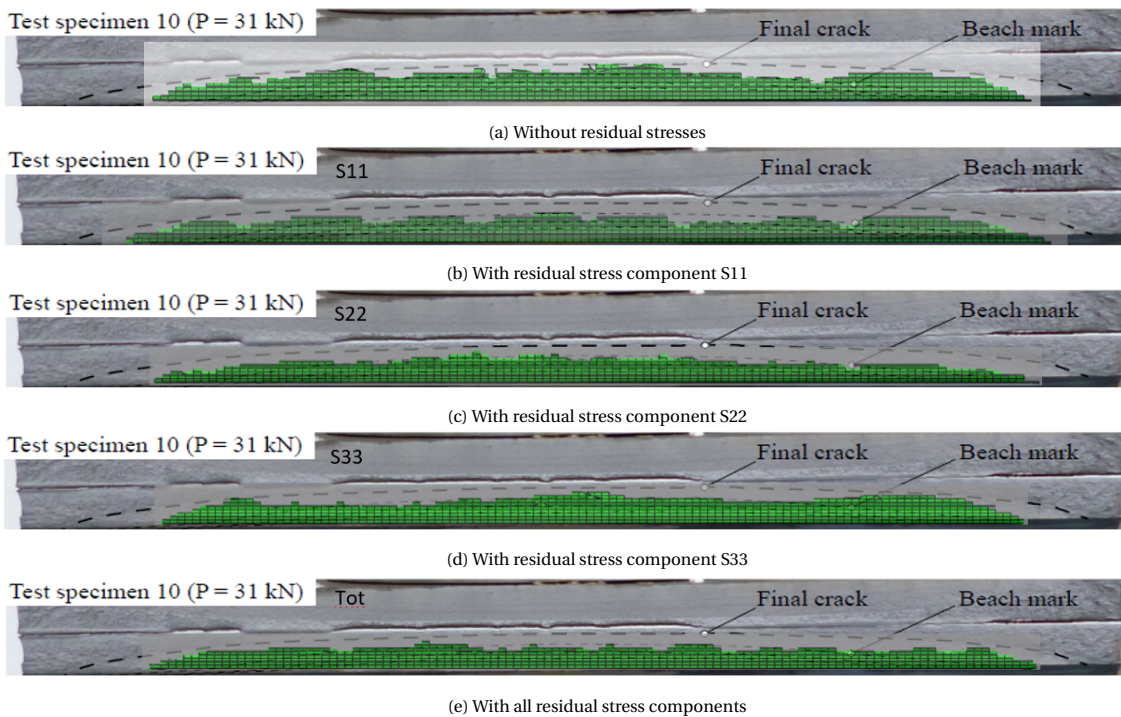


Figure 4.26: Comparison benchmark measurements and XFEM-results

In Figure 4.27, 4.28 and 4.29, the fracture energy release rate per fracture mode is shown. Overall it can be seen that fracture mode 1, shown in Figure 4.27, is dominant over fracture modes 2 and 3. Fracture mode 1, crack opening, corresponds to the crack propagation perpendicular to the crack face. Fracture modes 2 and 3 correspond to in-plane shear and out-of-plane shear, respectively. The inserted residual stresses cause higher fracture release rates compared to the base FEA in all three fracture modes. In the dominant fracture mode 1, the residual stress component S11 results in the highest energy release rate. This can be explained by the tensile stress component perpendicular on the crack surface causing the crack to open. The effect of residual stress components S22 and S33 are minimal as the results of these two FE-analysis are close to

the base FEA. The model with all the residual stress components is in between the model with the residual S11-component and the other two residual component models. The residual stress component S11 results in high energy release rates in fracture mode 2, in-plane shear. Influence of the residual stress components S22 and S33 are minimal as the results of these two FE-analysis are close to the base FEA. The model with all the residual stress components leads to results of the model with the residual S11-component and the other two residual component models. Fracture mode 2 is influenced by in-plane shear stresses, which correspond with S12-stresses in Abaqus. From the results, it can be explained that the inserted S11-component influences the S12-stresses around the crack region, which results in higher energy release rate. At last, residual stress component S33 results in the highest energy release rate in fracture mode 3. This mode is affected by out-of-plane shear which corresponds to S13-shear stresses in Abaqus. The tensile residual stress component S33 cause an increase in S13-shear stresses. The effect of residual stress components S11 and S22 are minimal as the results of these two FE-analysis are close to the base FEA, while the model which includes all three residual stress components follows the same trend as the residual stress S33 model.

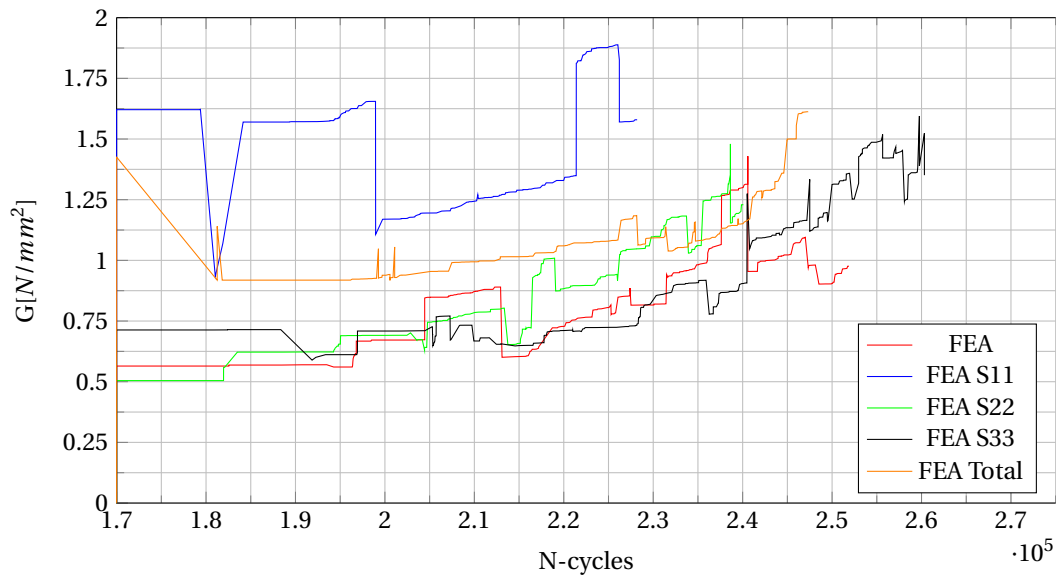


Figure 4.27: Results fracture models energy release rate mode K1

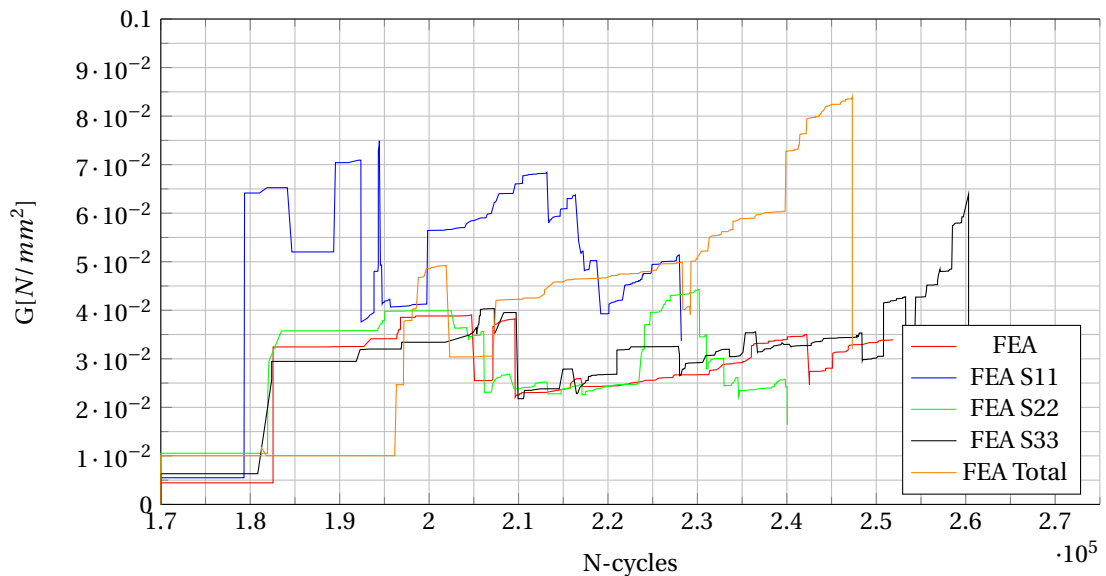


Figure 4.28: Results fracture models energy release rate mode K2

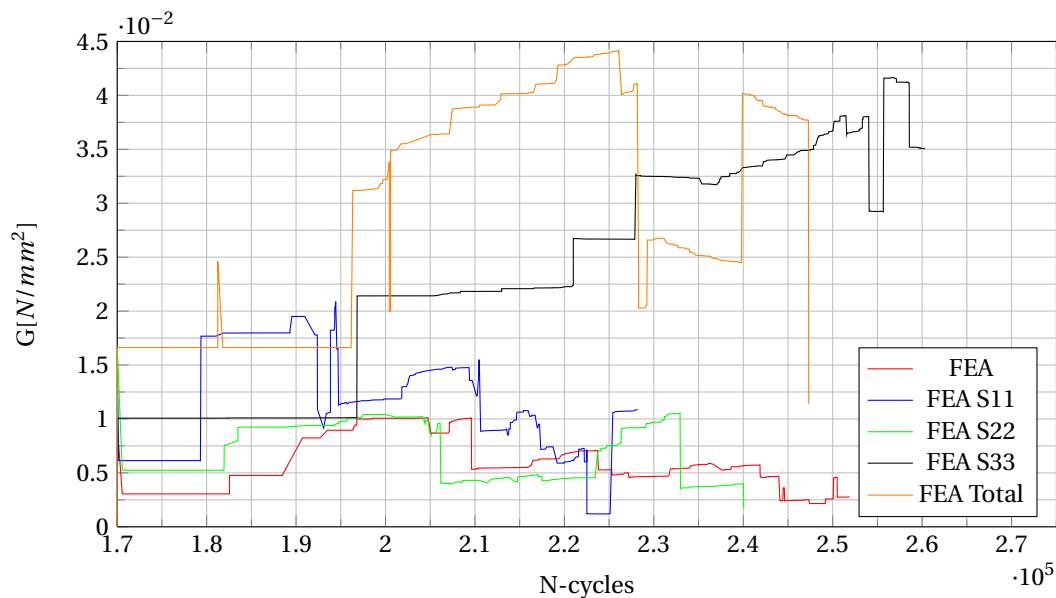


Figure 4.29: Results fracture models energy release rate mode K3

The results in Figure 4.24 are used to quantify the influence of the residual stresses. In Tables 4.3 and 4.4, the average percentage differences and squared correlation of each model crack depth is determined and compared to the experiment [25] and the base model without residual stresses. Both data shown in Tables 4.3 and 4.4 are determined using the formulas in equations 4.3 and 4.4.

$$R^2 = \left( \frac{n(\sum xy) - (\sum x)(\sum y)}{\sqrt{[n \sum x^2 - (\sum x)^2][n \sum y^2 - (\sum y)^2]}} \right)^2 \quad (4.3)$$

$$\% - difference = \frac{\sum_{i=1}^n \frac{(y_i - x_i)}{x_i}}{n} \quad (4.4)$$

The experimental data has been interpolated to increments of 0.75 mm, as this corresponds with the results of the FEA due to the mesh size of 0.75 mm. Next, the percentage difference compared to the experiment and the base model is computed and averaged. Faster crack propagation results in a negative percentage difference, while a slower crack propagation results in a positive percentage difference. The average difference per model is shown in Table 4.3. The squared correlation compared to the experiment and the base model is calculated and shown in Table 4.4. For equal comparison of the 'FEA Total' and 'FEA' models with the other models, the crack depth data till 6 mm is used. Influence of the inserted residual stresses compared to the base model is large, as the average percentage difference is 4% and the square correlation is relatively low at 98%. Residual stress components S11 and S22 both result in a higher crack propagation rate and therefore result in a lower fatigue life. In both components, the tensile residual stresses around the initial crack result in faster crack propagation compared to the base model. Residual stress component S33 results in a lower crack propagation rate and therefore in a higher fatigue life. The tensile residual stresses in the z-direction close the crack and result in a slower propagation rate.

The base model has a relatively low squared correlation of 95% compared to the experimental data. The crack propagation rate is higher as the average percentage difference is -3.1%. Compared to the experimental data, residual stress components S11, S22 and S33 all result in a higher crack propagation rate and therefore result in a lower fatigue life. In addition, all three models including one residual stress component have a relatively low square correlation, between 89.2% and 95.4%, compared to the base model and the model including all three residual stress components. The model including all three residual stress components has the highest squared correlation of 99% compared to the experimental data. The average percentage difference is 1.1%, which shows that the crack propagation rate is slightly lower compared to the experimental model. It is concluded that the model, including all three residual stress components, corresponds well with the experimental data. However, including one of the three components in a XFEM-analysis will not significantly improve the results compared to the base model.

<b>N-cycles %-difference</b>	<b>FEA base</b>	<b>FEA S11</b>	<b>FEA S22</b>	<b>FEA S33</b>	<b>FEA Total</b>
<b>Experiment</b>	-3.08%	-5.37%	-4.47%	-1.62%	1.09%
<b>FEA base</b>	0.00%	-1.82%	-2.62%	0.68%	4.34%

Table 4.3: Average percentage differences between experiments and FEA crack height

$R^2$	<b>FEA base</b>	<b>FEA S11</b>	<b>FEA S22</b>	<b>FEA S33</b>	<b>FEA Total</b>
<b>Experiment</b>	95.46%	89.23%	95.37%	94.37%	99.11%
<b>FEA base</b>	100.00%	97.85%	99.86%	99.84%	98.22%

Table 4.4: Squared correlation between experiments and FEA crack height

# 5

## Case study Suurhoffbridge

In this case study the obtained knowledge from the previous chapters is applied to the Suurhoffbridge. The effects of the residual stresses on the crack propagation rate is analysed in this chapter. In a previous MSc-thesis of R.S. Gupta [15] a fatigue analysis has been made without taking into account the residual stresses. That analysis consisted of a crack initiation phase and a crack propagation phase. In this case study the focus lies on the crack propagation phase, as the residual stresses will influence the crack propagation rate. First, the suurhoffbridge will be described. Secondly, the FEM-model will be described and verified using previous FEM-models. Thirdly, the critical load position is determined using influence lines based on SIF's. At last, the crack propagation model will be discussed.

### 5.1. Suurhoffbridge bridge description

The Suurhoffbridge is situated in the port area of Rotterdam over which the A15 highway runs. The bridge connects the second Maasvlakte (port terminal) to the infrastructure of Rotterdam. Under the bridge flows the hartelcanal which used by inland shipping from the harbour to other destinations. Next to the traffic bridge a cable-stayed railway bridge is situated over the Hartelcanal. An overview of the situation is presented in Figure 5.1. The total length of the bridge is 232.75 meter, of which two steel girder bridges and one movable bascule bridge. These three segments are denoted as SV01, SV02 and SB01 (bascule bridge). SV01, SV02 and SB01 have a length of respectively 150.8 meters, 48.05 meter and 33.9 meter. The lay-out of the bridge is presented in Figure 5.2. The bridge has been opened for traffic since 1972.

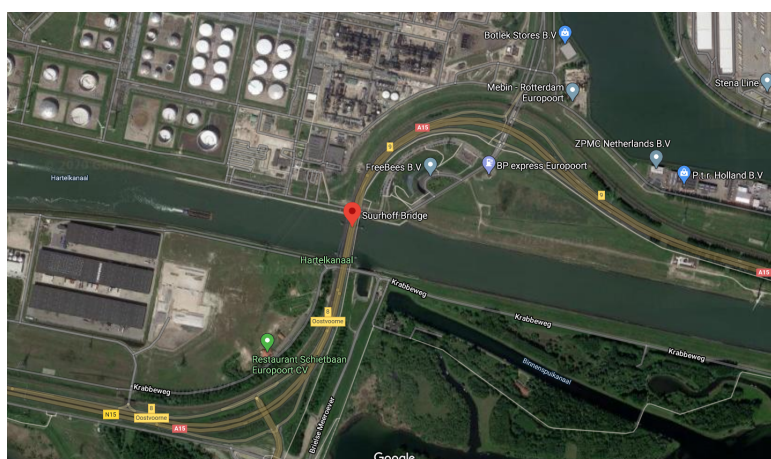


Figure 5.1: Overview Suurhoffbridge [24]

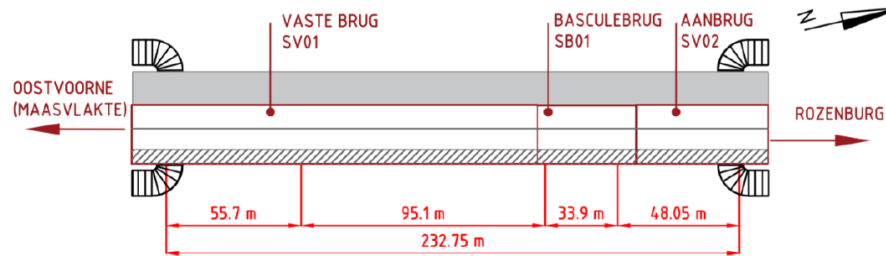


Figure 5.2: Lay-out Suurhoffbridge[15]

The bridge has a total width of 24.12 meters. This width is filled with a 2x2 highway and a pedestrian/bike lane. The two outside lanes are slow lanes while the two inner lanes are fast lanes. The bike lane is situated at the east side of the bridge. A cross-section of the bridge (SV01 & SV02) is presented in Figure 5.3.

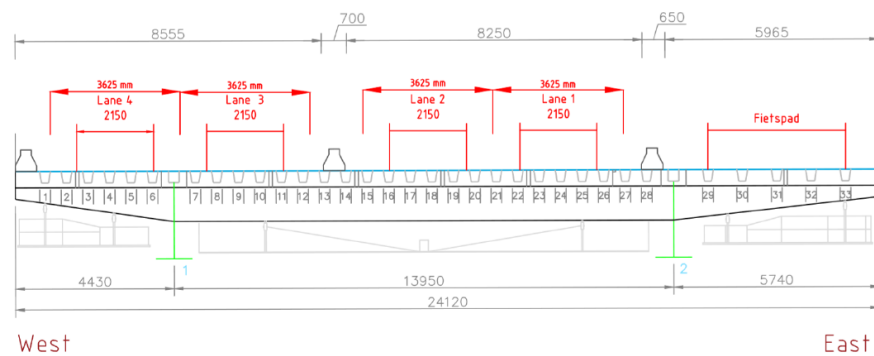


Figure 5.3: Cross-section (SV01 &amp; SV02) Suurhoffbridge[15]

In this report the focus lies on the largest fixed steel girder bridge (SV01) of the three segments. This bridge has an orthotropic steel deck with two steel longitudinal girders. The deck has a thickness of 10 mm while the stiffener has a thickness of 5 mm. The width of the stiffeners at the deck is 300 mm while the width at the bottom of the stiffener is 200 mm. The radius at the bottom corners of the stiffener is 17 mm. The center-to-center distance of the stiffener is 600 mm so the distance in between the stiffeners is 300 mm. On top of the deck an asphalt layer of 50 mm is applied. The geometry of the OSD is presented in Figure 5.4.

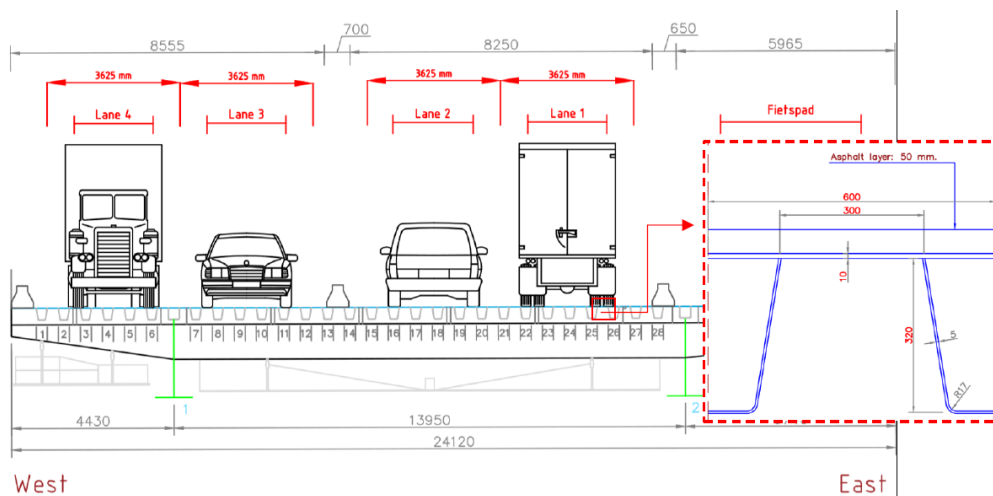


Figure 5.4: Geometry Suurhoffbridge[15]

### 5.1.1. Fatigue problems

During an analysis of the bridge in 2016, a fatigue root-to-deck crack with a length of 230 mm was discovered using Time Of Flight Diffraction (TOFD). The inspection was done between stiffener number 24 and number 27, presented in Figure 5.3. The crack position within the joint is different compared to the toe-to-deck crack described in Chapter 4. The stress field around the crack will be different due to the difference in load and geometric position. The root-to-deck crack, presented in Figure 2.3, is impossible to see at an early crack propagation stage as the crack can only be seen from inside the stiffener. The crack is becoming visible when the crack propagates completely through the deck and causes damage to the asphalt layer. With TOFD, the crack can be discovered at an earlier stage. When a crack is discovered, it is interesting how fast this crack propagates, as this determines when the crack needs to be repaired. The rate at which these cracks propagate is difficult to determine, as it is dependent on many factors like the magnitude of loading, material properties and the number of load cycles. Experiments on the crack propagation rate can give a view on the crack propagation rate, however these experiments are often time consuming and rather expensive.

With fracture mechanics, the crack propagation can be analysed using XFEM. This method will be used in this thesis in order to predict the crack propagation rate for this case study. A case study towards the crack propagation of this specific crack has been performed in the MSc-thesis of R.S. Gupta [15]. However, the FEM-model did not take into account the residual stresses. These stresses might have an effect on the crack propagation rate and therefore may result in a more accurate prediction of the crack propagation of this specific fatigue crack.

### 5.1.2. Fatigue analysis procedure

The fatigue analysis of this case study can be divided into three parts: Verification of the FEM-model, determination of the critical load position and the fatigue crack propagation simulation. The first two parts are needed in order to ensure that the FEM-model complies with the reality and that the critical load position is determined. In the last part, the knowledge obtained from chapters 3 and 4 will be applied on the case study. However, the whole lifespan of the bridge is not modelled in this case study as only the crack propagation phase is simulated, which is presented in Figure 5.5. A number of load cycles due to traffic will initiate the crack. This number of cycles to crack initiation has been determined by applying the HSS-method and a FEM-model in a previous report [15]. In this case study, a similar FEM-model has been modelled and the HSS have been compared with the present literature in order to verify the model and therefore assuming that the same amount of cycles is needed for crack initiation. Next, an influence line based on Stress Intensity Factors (SIFs) in order to obtain the critical load position. The crack propagation phase is modelled using the fatigue crack propagation simulation analysis using XFEM. In this analysis the effects of the residual stresses are determined in this XFEM-model using the simplified residual stresses described in section 3.2.7. Also the fatigue crack propagation simulation will be compared with the TFOD measurements. The whole procedure of this case study is presented in Figure 5.6.

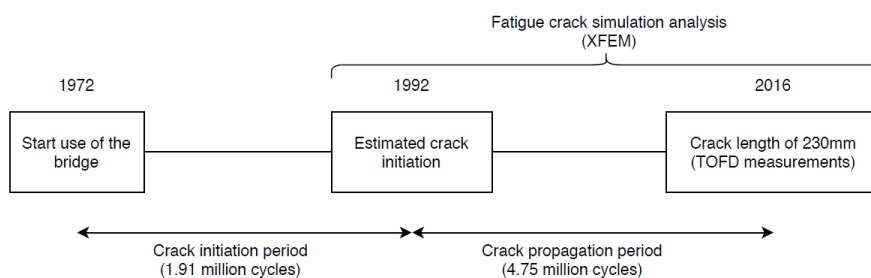


Figure 5.5: Fatigue analysis Suurhoffbridge [15]

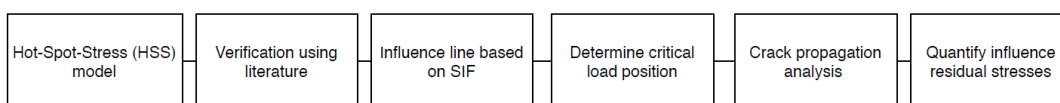


Figure 5.6: Fatigue analysis procedure case study

### 5.1.3. Material properties

In this model, both elastic material properties and Paris Law properties are applied,  $E = 210 \text{ GPa}$  and  $\nu = 0.3$ . It is assumed that S355 steel has been used in the bridge [15]. This is of great importance when determining the Paris Law parameters. It is difficult to exactly determine the Paris law parameters of the Suurhoff bridge as these are dependant on a various factors such as manufacturing conditions and temperature. As described in section 4.3, these parameters can influence the results substantially. Therefore, material testing on the analysed structure is essential to obtain accurate results. However in this case study an assumption will be made based on various literature. Similar parameters will be used as in the fatigue crack propagation simulation in chapter 4 although these parameters are changed slightly in order to obtain better results. These Paris Law parameters are presented in Table 5.1. At last, it is assumed that the properties of the filler material and the parent material is the same.

$C_1$	$C_2$	$C_3$	$C_4$	$G_I$	$G_{II}$	$G_{III}$	$\alpha_{m/n/o}$	$\frac{G_{thresh}}{G_c}$	$\frac{G_{pl}}{G_c}$
0.001	0	$1.10 * 10^5$	1.5	6.3	6.3	6.3	1	0	0.85

Table 5.1: Load and Paris law parameters case study [4, 25]

### 5.2. Hot-Spot Stress (HSS) analysis

This analysis is performed in order to verify if the boundary conditions and geometry correspond with literature data. Only a part of the bridge will be modelled, while the rest of the bridge is modelled using boundary conditions. A cross-section consisting of 4 U-shaped stiffeners (no. 24 - no. 27) will be modelled while the total length of the model is the distance between 4 cross beams. The whole model is presented in Figure 5.7. The model consists of a deck under which U-shaped stiffeners are placed, while both the deck and the stiffeners is supported by crossbeams. All the geometric parameters of the FEM-model are described in Table 5.8. The mesh of the model consist primarily of S4R-elements, except for a transition region which uses S3-elements. The mesh has been refined to a size of 2 mm around the loading area and around the position at where the HSS are obtained, which is at the weld root of the weld.

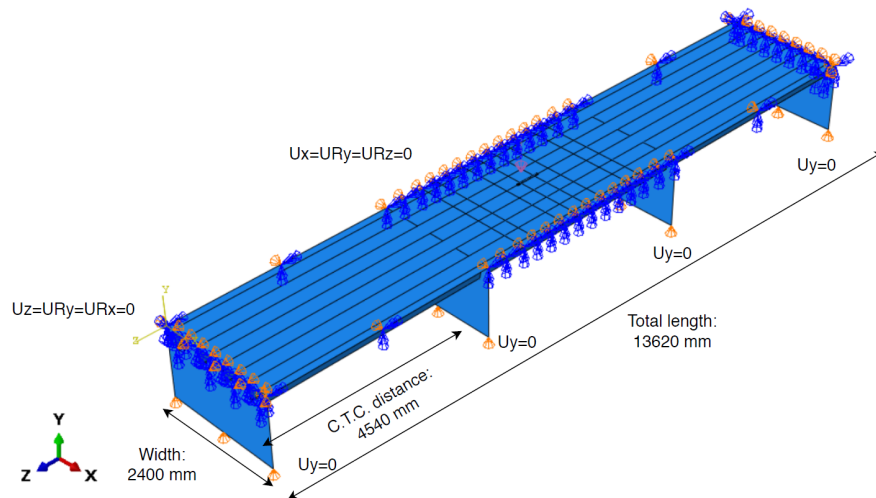


Figure 5.7: Hot Spot Stress (HSS) FEM-model

Part	Distance [mm]
<b>Deck</b>	
Width	2400
Length	13620
Thickness	10
<b>Stiffener</b>	
Height	320
Width top	300
Width bottom	200
Radius bottom corner	17
Thickness	5
C.T.C. distance	600
<b>Crossbeam</b>	
Height	1400
Width	2400
Thickness	14
C.T.C. distance	4540

Figure 5.8: Geometry HSS FEM-model Suurhoffbridge

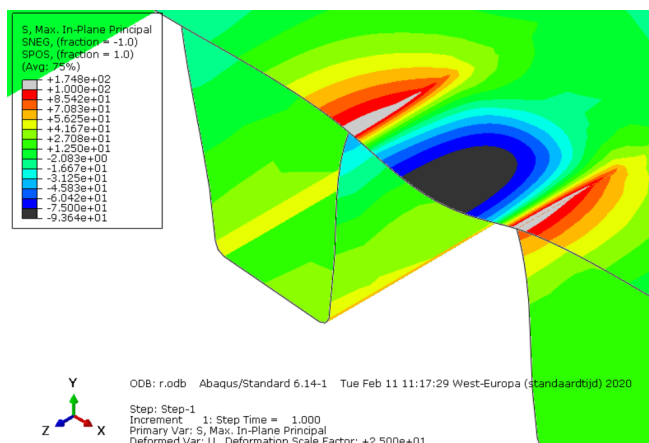


Figure 5.9: Cross-section results HSS-analysis (deformation scale 25x)

### 5.2.1. Load parameters

In this HSS-analysis the same load will be applied compared to the reports of Rijkswaterstaat [5] and R.S. Gupta [15]. The load will consist of a single Type C axle load of 105 kN placed in the middle of the specimen in between the the pair of stiffeners as can be seen in Figure 5.7. Contrary to the analysis in the report of Rijkswaterstaat, the whole axle does not fit on the relative small model, therefore only one wheel load (270 mm x 320 mm) of 52.5 kN is applied.

### 5.2.2. Boundary conditions

As only a small section of the bridge is modelled the boundary conditions are important, as these simulate the stiffness of the rest of the bridge. In this model, there are boundary conditions in all three directions. At both edges of the deck, symmetry boundary conditions have been applied in the x-direction. This implies that the edge of the deck is restricted for rotations around the z- and y-axis and it is restricted for deformation in the x-direction. This boundary condition simulates the continuation of the deck on either side of the model. At both ends of the deck and stiffeners symmetry boundary conditions have been applied in the y-direction. This implies that the edge of the deck is restricted for rotations around the x- and z-axis and it is restricted for deformation in the y-direction. At last, the bottom edge of the cross beams are restricted for deformations in the y-directions. As the crossbeams are very stiff in relation to the deck in combination with the stiffeners, the crossbeams will act as supports for the deck and stiffeners, which is simulated by the y-support.

### 5.2.3. Results

Within Abaqus® a static analysis is performed. The HSS are obtained from 10 and 4 mm away from the weld root. The maximal principal stresses are obtained from the FEM-model after the static analysis. In Figure 5.9, a cross-section of the static analysis is presented. In Figure 5.10, the Hot-spot stresses are presented from the static analysis. It can be seen that the results are close to the results of the report of RWS, which uses a mesh size of approximately 2.5 mm. The difference of the HSS at the weld root is 1 MPa, which corresponds to percentage difference of 1 %, although further from the root it can be seen that the trend of the RWS analysis is flatter while the trend of R.S. Gupta's analysis is slightly steeper. However the differences are so small that these are considered acceptable.

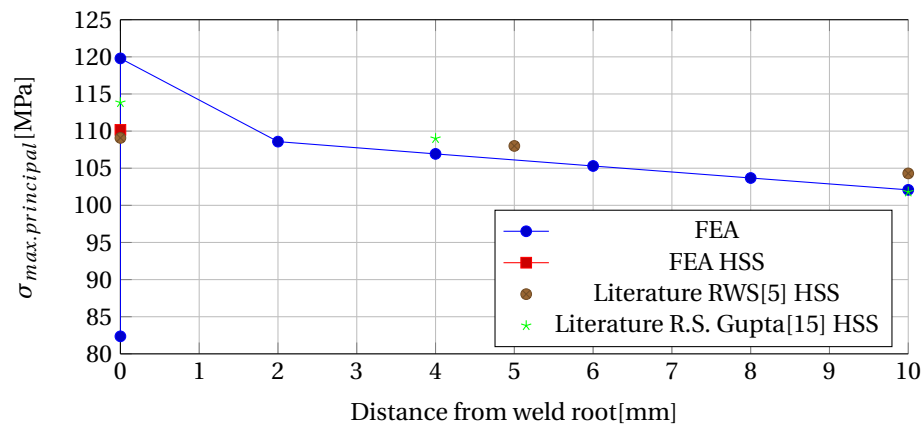


Figure 5.10: Hot spot stress weld root

### 5.3. Analysis critical load position

Next, the critical load position has to be determined. This will be done by using influence lines based on Stress Intensity factors (SIF's). Over the Suurhoffbridge runs a highway, therefore the most critical lorry has to be investigated. According to the NEN 8701 [27] lorry number T1103 (type 4) is most common on highways as 50 percent of the trucks are this type, therefore only this lorry type is analysed. The influence lines are analysed in both the transversal as longitudinal direction. At last, another model has been developed in which a crack is inserted and contains solid elements instead of only shell elements. The combination of both shell and solid elements is to keep the computation time relative low.

#### 5.3.1. XFEM-model

In order to obtain the SIF's caused by the moving load the FEM-model has to be adapted compared to the HSS-model in section 5.2. In order to introduce an initial static crack in the weld root of the joint, a solid part has to be introduced into the model, which is presented in Figure 5.11. The solid part is connected to the shell part using 'shell-to-solid couplings' within Abaqus®. The crack is inserted over the whole length (500 mm), ensuring that Abaqus® correctly recognizes the crack front and crack direction. The height of the crack is 2 mm. Assumed is that there is a gap at the weld root of 1 mm due to lack of penetration. At the right top corner of this gap, the initial crack is inserted, as denoted in red in Figure 5.12. The mesh of the solid part is constructed of linear brick C3D8R, while the rest of the model is using shell elements. Only using solid elements would result in long CPU-time (> 1 day) in order to obtain the influence line.

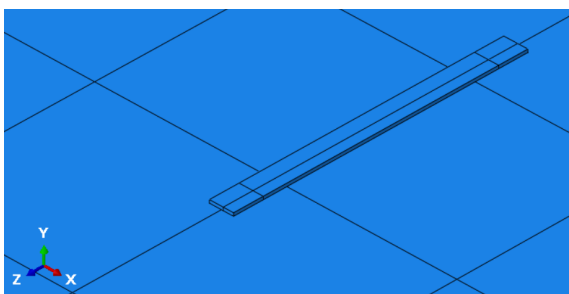


Figure 5.11: Overview solid part XFEM-model

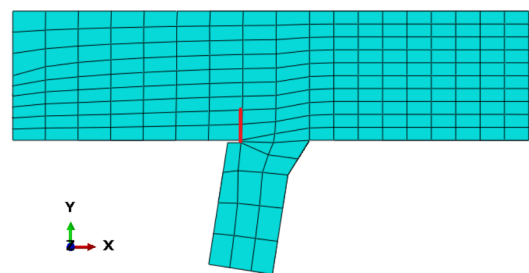


Figure 5.12: Mesh solid part XFEM-model

#### 5.3.2. Load model

There is assumed that lorry number T1103 (type 4) is governing as this type of truck has the most passes over the structure. A schematic overview of the load caused by the truck according to the NEN 8701 is presented in Figure 5.13. This lorry load will move over the deck of the bridge in both transversal and longitudinal direction in order to obtain the influence line. Within Abaqus®, the moving load will be introduced using the DLOAD-subroutine. This is a piece of Fortran-code in which the a pressure load can be assigned to certain coordinates within the model. The transversal DLOAD-subroutine is added to Annex C. The transversal influence lines

are produced with steps of 50 mm while the longitudinal influence line has steps of 100 mm. According to a previous case study [37], the governing position of a similar NEN 1991-2 lorry type 3 is under at the middle Type C axle. Therefore, a transversal influence line is produced where the middle Type C axle moves over the middle of the analysed crack section. Assuming, this is the critical load position in longitudinal direction, the most critical load can be determined by using only one pass. However, in order to verify this assumption a longitudinal influence line will be performed.

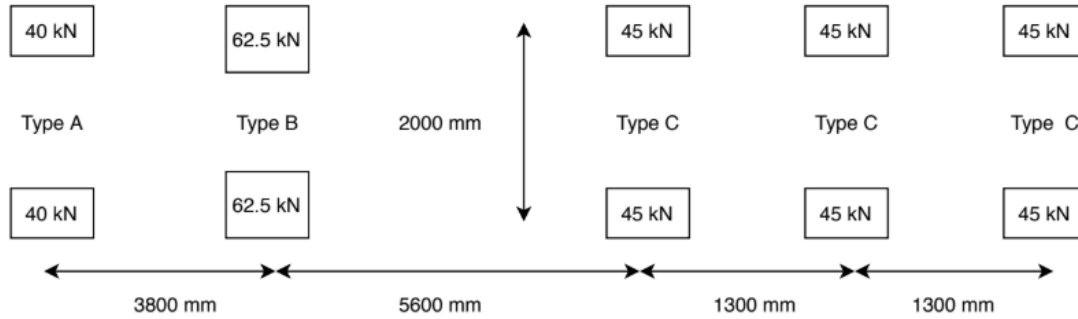


Figure 5.13: Loading scheme lorry number T1103 (type 4) NEN 8701

### 5.3.3. Results

In Figures 5.14 and 5.15, the influence lines in both transversal and longitudinal direction are presented. As can be seen in Figure 5.14, the transversal influence line results in a near symmetrical influence line, where either wheel load runs over the crack. The bigger peaks correspond with the position at which the wheel load is in between the stiffeners, presented in Figure 5.9, while the two smaller peaks correspond with the position at which the wheel load is in between the webs of the stiffener, so on the left-hand side of the position presented in Figure 5.9.

Next, an longitudinal influence line is obtained in the longitudinal direction in order to verify the assumption made in section 5.3.2. The x-position is the same as the peak in the transversal influence line, denoted in red. In Figure 5.15, it can be seen that the assumption in section 5.3.2 is right, as the middle Type C axle is most critical.

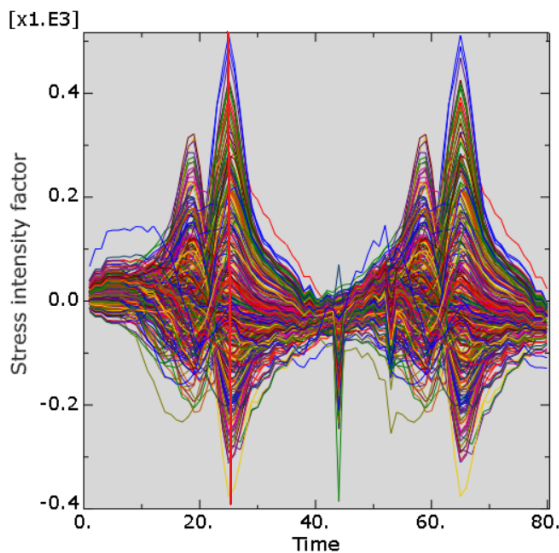


Figure 5.14: Transversal influence line fatigue crack mode 1

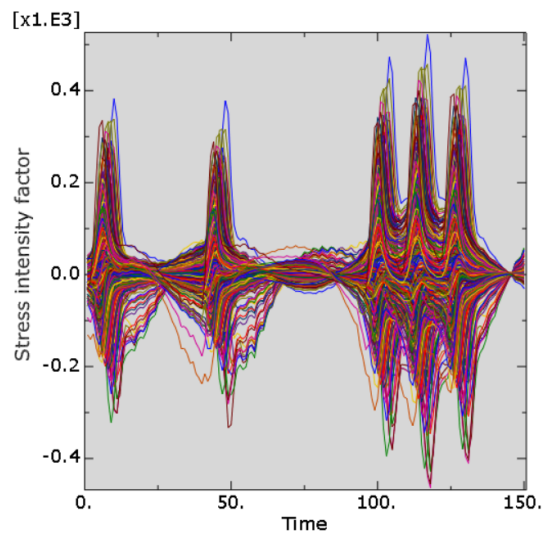


Figure 5.15: Longitudinal influence line fatigue crack mode 1

Next, an influence line is obtained by introducing residual stress components into the solid part of the model. Residual stress component S22 has been excluded, as these stresses do not stay in the solid part, but flow directly into the stiffener. This is caused by the shell elements in the deck as these cannot form equilibrium with stresses in the y-direction. Therefore only residual stress components S11 and S33 are taken

into account. Also the combination of these stress components has been analysed and is denoted as 'Total'. All the maximum values along the crack surface are presented in Figure 5.16. Residual stress component S11 has the largest effect on the SIF, while residual stress component S33 has hardly any influence on the SIF's. However the combination of residual stress component S11 and S33 resulted in the highest SIF's.

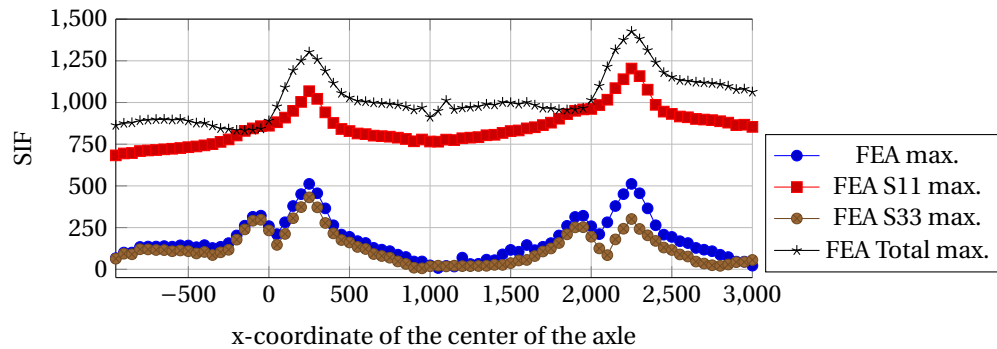


Figure 5.16: Maximum SIF transversal influence lines fatigue crack mode 1

However in the fatigue crack propagation simulation the initial crack will be relatively small and not span the whole length of the solid part. Therefore to obtain the critical load position the middle SIF from the middle element has been analysed and presented in Figure 5.17. The critical load position is at time step 18, which corresponds with the position at which the wheel load is in between the webs of the stiffener. The surrounding elements show the same, however these elements have been excluded from the graph as the graph would become crowded with lines. The effects of the residual stresses are still present, however in the middle these effects are much smaller. Concluding, the critical load position will be when the center of the wheel is located at  $x = -900 \text{ mm}$  and  $z = -6810 \text{ mm}$ , which corresponds with the position at which the wheel load is in between the webs of the stiffener in the middle of the bridge.

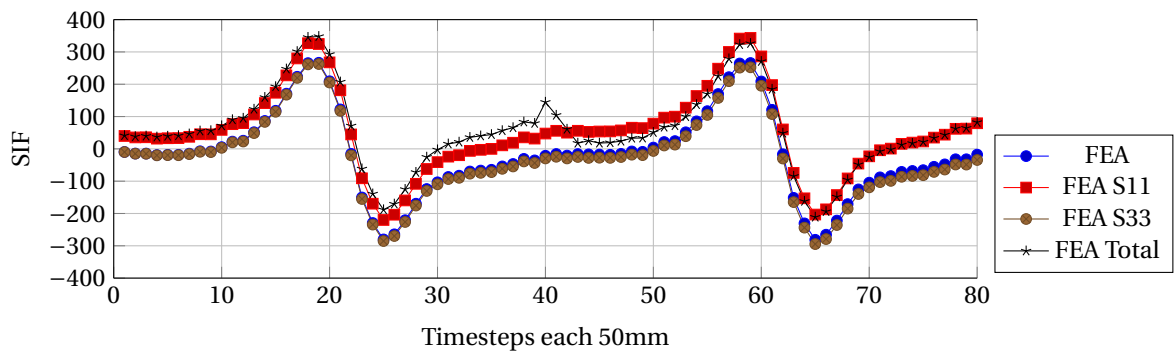


Figure 5.17: SIF middle element transversal influence lines fatigue crack mode 1

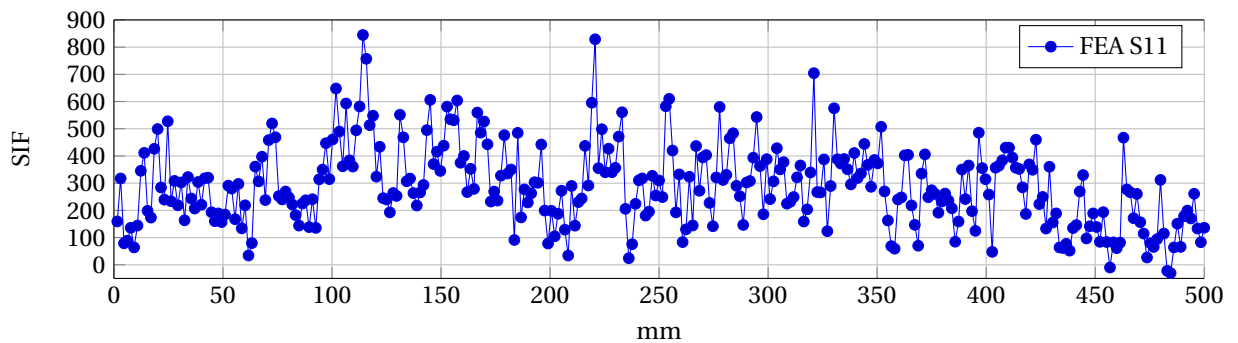


Figure 5.18: SIF along crack surface FEA S11 crack mode 1

At last, the SIF along the crack face is presented in Figure 5.18. It can be seen that the SIF is higher in the middle where the average lies around 300 and most of the peaks between a SIF of 50 and 600. Every 1.5 mm, a SIF is calculated as the mesh size in the z-direction is 1.5 mm. Only FEA S11 is presented as otherwise the graph would become unreadable. However the other models show a similar pattern.

## 5.4. Fatigue crack propagation simulation

In this section the HSS-analysis and the critical load analysis will be used in order to perform a fatigue crack propagation simulation. The fatigue crack propagation simulation will start after crack initiation has occurred. During the crack propagation simulation an initial crack will propagate due to a cyclic load.

### 5.4.1. XFEM-model

The model will be very similar compared to the critical load analysis including the same solid part in combination with the 'shell-to-solid couplings'. However the dimensions of the initial crack will be different. The initial rectangular crack has a crack length of 2.5 mm and a crack height of 1.25 mm. There is not chosen for a semi-ellipsoid shape as brick elements are used in the crack region. As the FEA-software can only crack whole elements and as the mesh is relative coarse due to the computing time the semi-ellipsoid shape will result in a rectangular shape in the analysis.

The mesh is similar as presented in Figure 5.12, consisting of linear brick C3D8R, while the rest of the model is using shell elements. Relative large elements with a height of approximately 1 mm and a width of 2 mm. There is chosen for large brick elements in order to reduce the computing time of the crack propagation analysis based on XFEM.

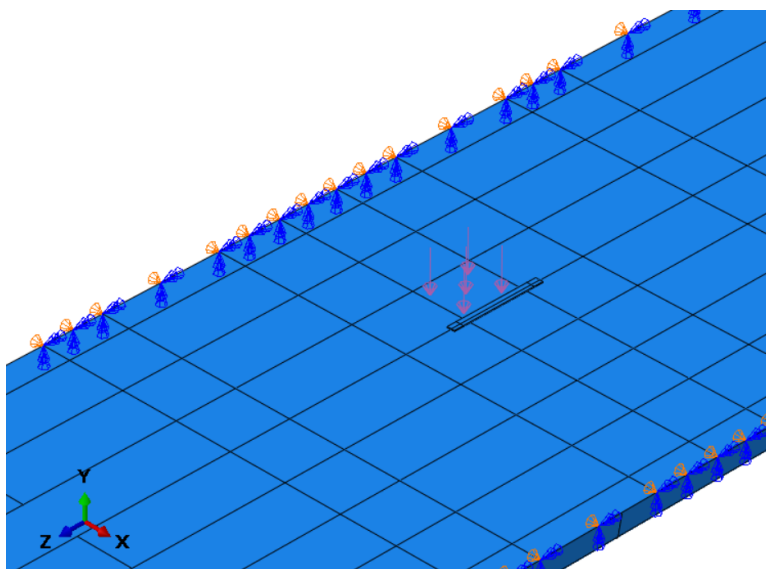


Figure 5.19: Wheel load position

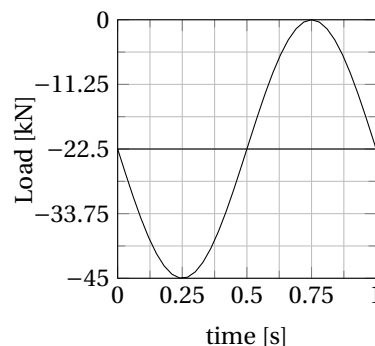


Figure 5.20: Direct cyclic wheel load

### 5.4.2. Load parameters

During the crack propagation analysis in Abaqus® a direct cyclic analysis will be performed. This quasi-static analysis simulates cyclic loading based on a varying load. This varying load causes a stress range that will be used to calculate the crack propagation using VCCT and LFM. There is chosen to load one wheel with a force of 45 kN, this load corresponds to the NEN8701 [27]. The load is applied on one wheel surface on the left-hand side of the solid part as presented in Figure 5.19. The wheel load of -45 kN is multiplied with a periodic function dependant of time in order to simulate cyclic loading. The total amount of cycles will be divided by three as three type C wheels passes the bridge per truck pass. The wheel loads of axles A and B are ignored as the SIFs of these loads are substantially lower as shown in Figure 5.15. These lower stresses will reduce the fatigue damage substantially as a doubling in stress range will result in 8 times ( $2^3$ ) the fatigue damage. The total load on the OSD-specimen is shown in Figure 4.5. The wheel load is applied in the negative y-direction where the total load is evenly spread over the load surface.

### 5.4.3. Results

The fatigue crack propagation simulation will be compared with the measurements from the TOFD [7]. In this thesis it is verified that there was a crack with a length of 230 mm and a height of 10 mm at the weld root of the rib-to-deck joint. After crack initiation in 1992, approximately 4.75 million heavy trucks have passed over the bridge before the TOFD measurements have taken place, as described in section 5.1.2. As three Type C wheels pass the bridge with every pass, the total number of load cycles of Type C wheels is 14.25 million cycles. The results will be focused on the crack length, denoted as 2C. The crack height is not that interesting as during crack propagation, full penetration of the deck occurs relatively quickly. Also the effects of residual stress components S11 and S33 will be evaluated.

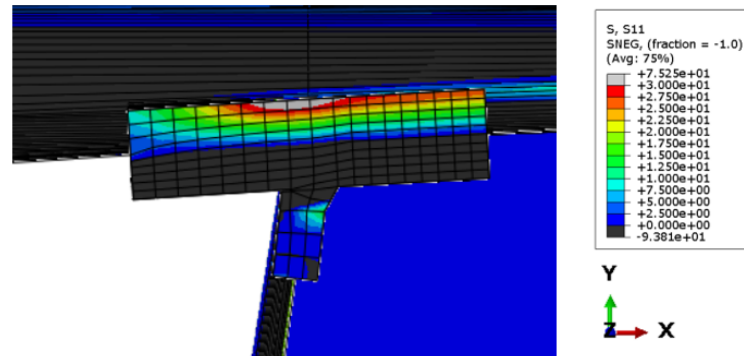


Figure 5.21: Base FEA transversal stresses S11 (X-direction)

First, the base fatigue crack propagation simulation has no residual stress components inserted. As the wheel load is activated onto the deck of the bridge as a cyclic load a compressive transversal stress occurs due to the wheel load and subsequently closes the crack. A contour plot in the middle of the solid part is presented in Figure 5.21. The result is that even at very high cycles no crack propagation occurs as the minimal threshold for crack propagation is not met due to compressive force.

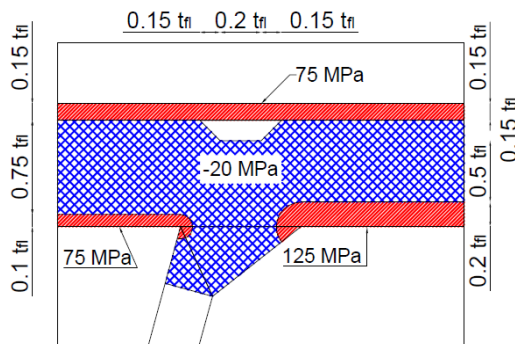


Figure 5.22: Simplified residual stress component S11

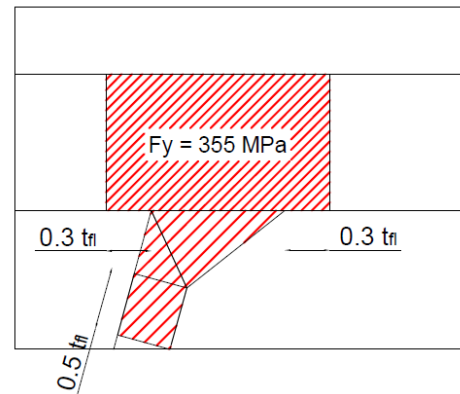


Figure 5.23: Simplified residual stress component S33

Next, the fatigue crack propagation simulation including residual stress components is analysed. The simplified residual stresses, described in section 3.2.7, are used in this case study as a separate weld simulation for this geometry would be too time consuming. Also, the exact weld parameters of the Suurhoffbridge are not available. It is likely that the manual welding is applied on the rib-to-deck joint as the structure is produced in the seventies, this could lead to a different residual stress field. The simplified stresses of residual stress component S11 and S33 are presented in Figures 5.22 and 5.23.

The fatigue crack propagation simulation including residual stress component S11 is presented in Figure 5.28 in which the specimen is not loaded. The shell elements are also pre-loaded with a tensile transversal stress of 60 MPa in order to keep the tensile stress at the bottom of the deck, otherwise the crack will not propagate due to the compressive force. If this is not done the inserted residual stresses will find equilibrium with the

shell elements surrounding the solid part, resulting in a reduced residual stress field. This phenomena can be reduced to insert the full simplified stresses over the whole cross-section or using solid elements in the whole model. This phenomena is less of an issue in Chapter 4 as there only solid elements are used.

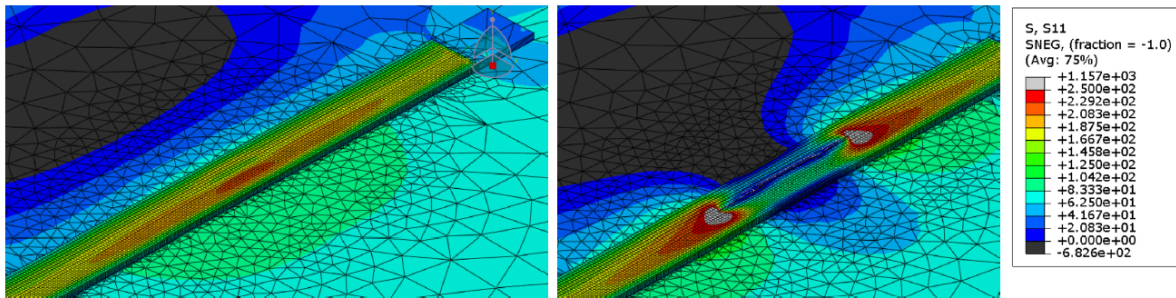


Figure 5.24: Results FEA S11 transverse stress field

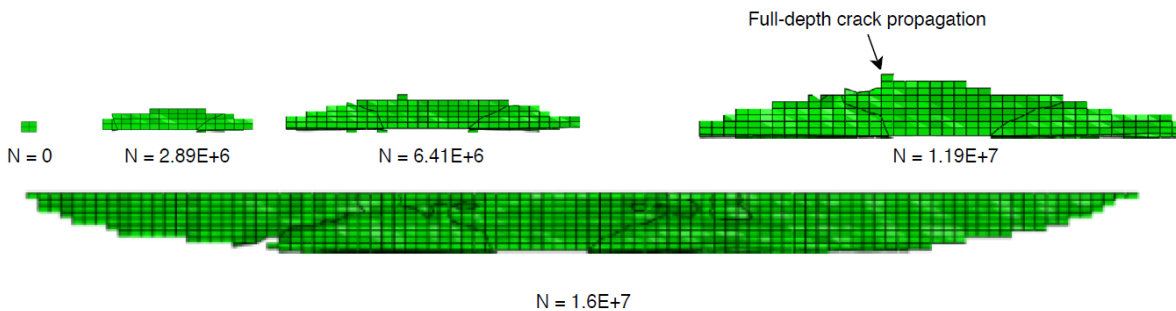


Figure 5.25: Results FEA S11 crack phases

In Figures 5.24, 5.25 and 5.26, the results of the fatigue crack propagation simulation including residual stress component S11 are presented. As presented in Figure 5.26, the crack propagates in the propagation phase in a linear trend, but at around  $1.35 \cdot 10^7$  cycles the crack propagation rate increase till around  $1.62 \cdot 10^7$  cycles at which the crack becomes unstable. That is also the point at which the 230 mm crack length is reached. In Figure 5.25, it can be seen that until  $6.41 \cdot 10^6$  cycles the crack propagates both upwards and to both sides, where the crack has pyramid-shape. At  $1.19 \cdot 10^7$  cycles, the crack reaches the deck surface, which causes the crack to primarily propagate to both sides. At  $1.6 \cdot 10^7$  cycles the crack propagates primarily at the top surface of the crack. Also, the crack shape changes from a pyramid shape towards an inverted pyramid shape. This phenomena can be explained as at the top surface of the deck a transverse tensile stress is present due to the wheel load, which accelerates the crack propagation in the z-direction. In Figure 5.24 the difference in transverse (x-direction) stress field between a partial depth crack and a fully penetrated crack. In the left picture, the crack has not fully penetrated the deck yet although there can be seen a slight change in the middle of the solid part where the crack has an effect on the transversal stress field. On the right picture, the crack is penetrated through the full thickness of the deck over a certain length. The fully penetrated crack obstructs the load transfer of the wheel load in transverse direction, which causes traversal stress peaks at both crack tips as the transversal stresses flow around the crack. This phenomena increases as the fully penetrated crack becomes larger till a point at which the crack becomes unstable and fails. These increasing transverse stresses at either end of the crack explain also the steep increase in crack propagation rate presented in Figure 5.26. In comparison to the TOFD measurements the crack propagation simulation has a difference of approximately 14 percent. This is a good result as both Type A and B wheels are ignored and would slightly reduce the fatigue life which would result in more accurate results.

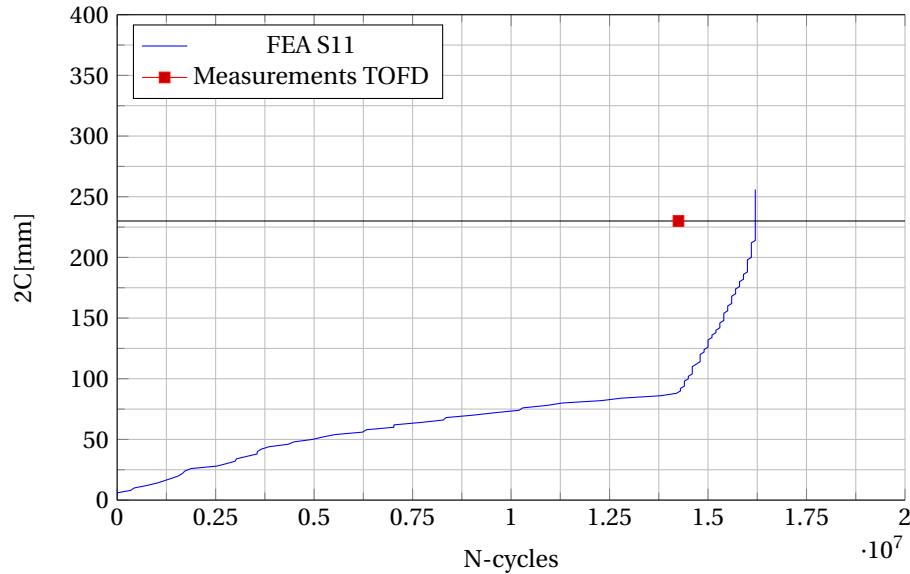


Figure 5.26: Results fatigue crack simulation FEA S11 crack length 2C

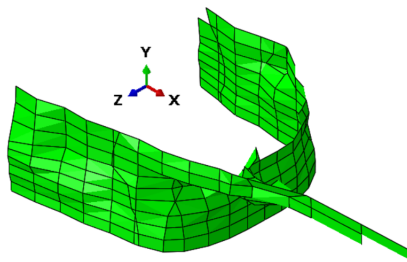


Figure 5.27: FEA crack propagation residual stress components S11 &amp; S33

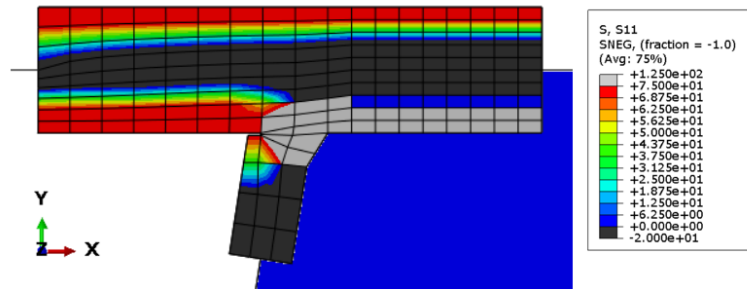


Figure 5.28: FEA residual stresses (X-direction)

Next, the fatigue crack propagation simulation including residual stress component S33, but without residual stress component S11, will result in no crack propagation due to the same reasons as the base model. The inserted residual stresses in the z-direction do not effect the compressive stresses in the transversal direction, which cause crack closure and prevent crack propagation.

At last, the fatigue crack propagation simulation including residual stress components S11 and S33. In this model both transverse and longitudinal residual stresses are introduced. The longitudinal tensile residual stress component S33 is around the yield stress, while the transverse stresses are much lower at maximal 1/3 of the yield stress. This difference in stresses will effect the crack propagation direction in which the relative small initial crack grows. The crack grows due to the relative high longitudinal stresses in transverse direction, which results in unrealistic crack growth. When the direction of the crack changes slightly, the high longitudinal stresses cause rapid fracture mode 1 crack propagation, and cause the crack to propagate unrealistic in transverse direction. The result of this phenomena is presented in Figure 5.27. To avoid this phenomena it is advised to only introduce the residual stresses in the transverse direction. It can also be concluded that the effect of residual stresses is large regarding the fatigue crack propagation of a fatigue crack at the weld root. Especially the residual stress component in transverse direction as natively transversal compressive stresses are present at the weld root.

## 5.5. Discussion

The method described in Chapter 4 shows good results when comparing to experimental data. However when applying the method on a large scale case study many assumptions have been made in order to obtain good results. Furthermore, there are many factors where small changes will affect the results to large extend. The large number of factors that can have effect on the results can prevent applying this methods on large scale

structures as the accuracy and CPU-time of the method should be improved. The following assumptions that have been made are described below with the possible improvements that can be made in future research.

- The material properties applied in this case study are based on literature [4, 25] and knowledge obtained in Chapter 4. However to obtain accurate results the material parameters should arise from material testing from the analysed structure as these parameters have a large effect on the results. It is likely that the manual welding is applied on the rib-to-deck joint as the structure is produced in the seventies. This could have a significant influence on the results as the residual stress field could be completely different for both the welding method as geometry.
- The magnitude and amount of cycles is not exactly measured but assumed based on the NEN8701 [27]. Especially the magnitude of the load is important as a doubling in load would result in 8 times ( $2^3$ ) the fatigue damage as this relation is cubic. In an ideal situation both parameters should be monitored in order to obtain accurate results.
- The combination of solid- and shell-elements using 'shell-to-solid couplings' results in difficulties when introducing and retain the residual stresses in the XFEM-model. In the fatigue crack simulation described in Chapter 4 using only solid elements it was possible to retain most of the residual stresses. A model with only solid elements would result in a substantially large CPU-time, resulting in multiple days of calculating a XFEM-model on a workstation. As described in the results the residual stresses have large effects on the crack propagation. Especially the residual stress component in transverse direction as natively transversal compressive stresses are present at the weld root.
- The residual stresses applied in the case study are based on an automatic weld sequence while it is likely that the manual welding is applied on the rib-to-deck joint as the structure is produced in the seventies. The residual stress field caused by the manual welding process will be different, which could lead to different results.
- The boundary conditions of the XFEM-model are largely based on assumptions described in literature [5, 15]. Although the HSS-model verifies that the stresses at the weld root are similar with large scale FEM-models it would be better if there were experimental data to obtain the stresses at the weld root.
- It can be noted that the position at which the crack occurs has influence on the effect of the residual stress components. As described in Chapter 4, the transverse residual stress component S11 has limited influence on the crack propagation, while in the case study the influence of this component is essential as a transversal compressive stress field is present. In the crack simulation in Chapter 4, the crack is introduced at the weld toe, while in the case study the crack is introduced at the weld root. However more accurate research is required in order to support this as this can also be related to other factors.



# 6

## Conclusions & Recommendations

In this final chapter, both the conclusions and recommendations of this research project are described. After the conclusions, a number of recommendations are given for future research.

### 6.1. Conclusions

From both the weld simulation as fatigue crack simulation analysis, the following conclusions are made:

- The thermomechanical FEA resulted in a residual stress field of the OSD-specimen. Simplified residual stress field for each component of the global stress direction is successfully accomplished and these results are used as input for modelling of the fatigue crack propagation.
- The fatigue crack propagation analysis without residual stresses resulted in a squared correlation factor of 95.4% compared to the experimental data considering the crack depth. The analysis is improved compared to previous models [15], by using the same material properties as the experimental data [25]. The FEA resulted in a higher crack propagation rate as the average percentage difference is -3% compared to the experimental data.
- The fatigue crack propagation simulation including the simplified residual stress field resulted in a squared correlation of 99% compared to the experimental data considering the crack depth. The FEA resulted in a slightly slower crack propagation rate as the average percentage difference in terms of fatigue cycles is 1.1%. It is concluded that the residual stresses influence the crack propagation rate leading to improve the FE results significantly. Compared to the experimental data, residual stress components S11, S22 and S33 all result in a higher crack propagation rate and therefore result in a lower fatigue life. In addition, all three models including one residual stress component have a relatively low square correlation, between 89.2% and 95.4%, compared to the base model and the model including all three residual stress components.

It is concluded that the model, including all three residual stress components, corresponds well with the experimental data. FEA that includes one of the three residual stress components in a fatigue crack propagation analysis will not significantly improve the results compared to the crack propagation analysis without residual stresses.

From the case study regarding the Suurhoffbridge, the following conclusions are made based on the results of the fatigue crack growth simulation:

- The results of the hot-spot stresses based on the static FE-analysis correspond well with the other FEM-models in literature, as the difference in HSS is only 1%. This shows that the boundary conditions and geometry are verified, as the results are compared to an analysis in which the whole bridge is modelled.
- The obtained influence lines based on SIF factors determined the critical load position on the structure. These lines showed that critical position was when the wheel load was positioned between the webs of the stiffener.

- Also, from the influence lines can be concluded that the residual stresses in the transverse direction increase the stress intensity factors, while the influence of the residual stresses in longitudinal direction is much smaller.
- From the fatigue crack growth simulation it can be concluded that the transverse residual stress component  $S_{11}$  is essential for crack propagation, as these tensile stresses initiate the crack propagation phase. The XFEM-model without any transverse tensile residual stresses will not propagate as a compressive transverse stress field prevents crack propagation. The longitudinal residual stress component  $S_{33}$  also does not initiate crack propagation as the compressive transverse stress field is present and prevents crack propagation. Including both longitudinal and transversal residual stresses does result in crack propagation. However, the longitudinal tensile residual stresses do result in unrealistic crack propagation.
- Overall, the fatigue crack simulation including the transverse residual stresses corresponds relatively well compared to the measured data as the difference is only approximately 14%, also considering that two wheel load that have limited effect have been ignored in the analysis. If these two wheel loads would be included the results will improve.

## 6.2. Recommendations

The following recommendations can be made regarding the fatigue crack propagation simulation.

- During a study of the boundary conditions in the crack propagation FE model, a second model is developed. The interface between the OSD-specimen and the set-up has been modelled using 'surface-to-surface'-contact. Currently, it is difficult to use this type of boundary conditions with a direct cyclic analysis, as the deformation during this analysis is too large for the 'surface-to-surface'-contact. There is potential for improvement of FEA by improving the boundary conditions in the future study.
- The crack length propagation does not correspond satisfactory to the experimental data, while the crack depth does. This part could be improved by using other types of element types as the stress distribution at either edge of the crack will change. This can be done with triangular elements (C3D4/10), however, this requires a significant increase of the CPU-time.

The following recommendations can be made regarding the case study of the Suurhoffbridge.

- The boundary condition, material properties and loading by heavy traffic should be determined more accurately with measurements in order to verify the model properties. In this case study a lot of assumptions are made in the model properties, which could lead to inaccurate results.
- An XFEM model with only solid elements will make it possible to retain the residual stresses field better during the direct cyclic analysis. This would also make it possible to introduce the vertical (y-direction) residual stress component into the XFEM-model.

# Bibliography

- [1] *ABAQUS/Standard User's Manual, Version 6.14*. Simulia, 2014.
- [2] Abaqus-docs. Modeling discontinuities as an enriched feature using the extended finite element method. *Abaqus-docs.mit.edu*. URL <https://abaqus-docs.mit.edu/2017/English/SIMACAEANLRefMap/simaanl-c-enrichment.htm>.
- [3] T. Belytschko and T. Black. Elastic crack growth in finite elements with minimal remeshing. *International Journal for Numerical Methods in Engineering*, 45(5):601–620, 1999. doi: 10.1002/(SICI)1097-0207(19990620)45:5<601::AID-NME598>3.0.CO;2-S. URL <https://onlinelibrary.wiley.com/doi/abs/10.1002/%28SICI%291097-0207%2819990620%2945%3A5%3C601%3A%3AAID-NME598%3E3.0.CO%3B2-S>.
- [4] Fatih Bozkurt and Eva Schmidová. Fracture Toughness Evaluation of S355 Steel Using Circumferentially Notched Round Bars. *Periodica Polytechnica Transportation Engineering*, 2018. doi: 10.3311/PPtr.11560.
- [5] Janwillem Breider. Suurhoffbrug Phase 2 Technical Assessment Report MC Renovatie Bruggen. Technical report, Royal HaskoningDHV Arup, 2013.
- [6] J. Burk and F. Lawrence. Influence of bending stresses on fatigue crack propagation life in butt joint welds. *Journal Weld*, 56:375–383, 2001.
- [7] Victor Buyck Steel Construction. Renovatie Suurhoffbrug. 2016.
- [8] Dassault Systèmes Simulia Corp. Abaqus version 6.14/17. 2019, jun .
- [9] Dassault Systèmes Simulia Corp. Abaqus version 6.14 manual. 2019. URL <http://ivt-abaqusdoc.ivt.ntnu.no:2080/v2016/books/usb/default.htm?startat=pt04ch10s07at36.html>.
- [10] José Correia. *An Integral Probabilistic Approach for Fatigue Lifetime Prediction of Mechanical and Structural Components*. PhD thesis, 04 2015.
- [11] Chuang Cui, Yi Bu, Yi Bao, Qinghua Zhang, and Zhongtao Ye. Strain Energy-Based Fatigue Life Evaluation of Deck-to-Rib Welded Joints in OSD Considering Combined Effects of Stochastic Traffic Load and Welded Residual Stress. *Journal of Bridge Engineering*, 23, 08 2017. doi: 10.1061/(ASCE)BE.1943-5592.0001181.
- [12] F.B.P de Jong. Renovation techniques for fatigue cracked orthotropic steel bridge decks. *TU Delft*, 2007. URL <http://resolver.tudelft.nl/uuid:239bdb2c-b59f-40d2-91b7-367139dbad13>.
- [13] John Goldak, Aditya Chakravarti, and Malcolm Bibby. A new finite element model for welding heat sources. *Metallurgical Transactions B*, 15(2):299–305, Jun 1984. ISSN 1543-1916. doi: 10.1007/BF02667333. URL <https://doi.org/10.1007/BF02667333>.
- [14] A. A. Griffith. The Phenomena of Rupture and Flow in Solids. *Philosophical Transactions of the Royal Society of London Series A*, 221:163–198, 1921. doi: 10.1098/rsta.1921.0006.
- [15] Ravi Shankar Gupta. Prediction of Fatigue Crack Propagation in Orthotropic Steel Decks using XFEM based on LFM and VCCT. *TU Delft*, 2019. URL <http://resolver.tudelft.nl/uuid:ef98f2f7-aa79-4bd1-b444-be8c2915eafe>.
- [16] T.K. Hellen. How To– Undertake Fracture Mechanics Analysis with Finite Elements. *NAFEMS*, 2001. URL [https://www.nafems.org/publications/browse\\_buy/browse\\_by\\_topic/fracture/ht18/](https://www.nafems.org/publications/browse_buy/browse_by_topic/fracture/ht18/).
- [17] G. R. Irwin. Fracture Mode Transition for a Crack Traversing a Plate. *Journal of Fluids Engineering*, 82(2):417–423, 06 1960. ISSN 0098-2202. doi: 10.1115/1.3662608. URL <https://doi.org/10.1115/1.3662608>.

- [18] Bohai Ji, Rong Liu, Ce Chen, Hirofumi Maeno, and Xiongfei Chen. Evaluation on root-deck fatigue of orthotropic steel bridge deck. *Journal of Constructional Steel Research*, 90:174 – 183, 2013. ISSN 0143-974X. doi: <https://doi.org/10.1016/j.jcsr.2013.07.036>. URL <http://www.sciencedirect.com/science/article/pii/S0143974X13002290>.
- [19] Suraj Joshi, Jörg Hildebrand, Abdulkareem S. Aloraier, and Timon Rabczuk. Characterization of material properties and heat source parameters in welding simulation of two overlapping beads on a substrate plate. *Computational Materials Science*, 69:559 – 565, 2013. ISSN 0927-0256. doi: <https://doi.org/10.1016/j.commatsci.2012.11.029>. URL <http://www.sciencedirect.com/science/article/pii/S092702561200688X>.
- [20] Shigenobu Kainuma, Young-Soo Jeong, Muye Yang, and Susumu Inokuchi. Welding residual stress in roots between deck plate and U-rib in orthotropic steel decks. *Measurement*, 92, 06 2016. doi: 10.1016/j.measurement.2016.06.040.
- [21] Lukic M. Nussbaumer A. Günther H.-P. Helmerich R. Kolstein M. H. Walbridge S. Androic B. Dijkstra O. Kühn, B. and Ö Bucak. Assessment of Existing Steel Structures: Recommendations for Estimation of Remaining Fatigue Life. *JRC Scientific and Technical Reports*, 2008. ISSN 1018-5593.
- [22] M.H. Kolstein. Fatigue classification of welded joints in orthotropic steel bridge decks. *TU Delft*, 2007. URL <http://resolver.tudelft.nl/uuid:a7bb8daa-930b-405d-af60-8fbfb7c4119b>.
- [23] S.J. Maddox. Fatigue design rules for welded structures. 2011.
- [24] Google Maps. Suurhoffbrug. URL <https://www.google.com/maps/>.
- [25] Wim Nagy. *Fatigue assessment of orthotropic steel decks based on fracture mechanics*. PhD thesis, Ghent University, 2017.
- [26] *NEN-EN 1993-1-2*, 2011. NEN.
- [27] *NEN 8701*, 2011. NEN.
- [28] *NEN-EN 1993-1-9*, 2012. NEN.
- [29] P. Paris and F. Erdogan. A Critical Analysis of Crack Propagation Laws. *Journal of Fluids Engineering*, 85 (4):528–533, 12 1963. ISSN 0098-2202. doi: 10.1115/1.3656900. URL <https://doi.org/10.1115/1.3656900>.
- [30] Artem Pilipenko. Computer simulation of residual stress and distortion of thick plates in multi-electrode submerged arc welding. Their mitigation techniques. *Department of Machine Design and Materials Technology, Norwegian University of Science and Technology, N-7491 Trondheim, Norway*, July 2001. URL <http://hdl.handle.net/11250/231322>.
- [31] RWS. Inventarisatie kunstwerken. *Rijkswaterstaat*, 2007.
- [32] Vishnu Saseendran. *Fracture Characterization and Analysis of Debonded Sandwich Composites*. PhD thesis, 12 2017.
- [33] Matteo Schiaretti. Numerical Simulation of Fatigue Crack Growth in a Stiffened Plate. *TU Delft*, 2017. URL <http://resolver.tudelft.nl/uuid:9eda9105-2111-4c09-8b56-b894ca4ff008>.
- [34] Kallia Spyridoni. Prediction of residual stress of an orthotropic plate due to welding. *TU Delft*, 2019. URL <http://resolver.tudelft.nl/uuid:76087661-ed45-4df4-b7e6-8fc0cd6164da>.
- [35] Kallia Spyridoni, Haohui Xin, Marcel Hermans, and Milan Veljkovic. Calibration of welding simulation parameters of fillet welding joints used in an orthotropic steel deck. *ce/papers*, 3(3-4):49–54, 2019. doi: 10.1002/cepa.1089. URL <https://onlinelibrary.wiley.com/doi/abs/10.1002/cepa.1089>.
- [36] Thonnard. 1985.
- [37] N.J.H. van den Berg. Fatigue design of an orthotropic deck. Cie4125 case study: Steel, timber and frp, TU Delft, 2019.

- [38] Ying Wang, Zhen Wang, and Yuqian Zheng. Analysis of Fatigue Crack Propagation of an Orthotropic Bridge Deck Based on the Extended Finite Element Method. *Advances in Civil Engineering*, 2019:1–14, 07 2019. doi: 10.1155/2019/6319821.
- [39] G.A. Webster and A.N. Ezeilo. Residual stress distributions and their influence on fatigue life-times. *International Journal of Fatigue*, 23:375 – 383, 2001. ISSN 0142-1123. doi: [https://doi.org/10.1016/S0142-1123\(01\)00133-5](https://doi.org/10.1016/S0142-1123(01)00133-5). URL <http://www.sciencedirect.com/science/article/pii/S0142112301001335>.
- [40] P J Withers. Residual stress and its role in failure. *Reports on Progress in Physics*, 2007. URL <https://doi.org/10.1088%2F0034-4885%2F70%2F12%2F04>.
- [41] P.J. Withers and H.K.D.H. Bhadeshia. Residual stress. Part 2 – Nature and origins. *Materials Science and Technology*, 17(4):366–375, 2001. doi: 10.1179/026708301101510087.
- [42] Edward Ming-Yang Wu and Jr Robert C. Reuter. Crack extension in fiberglass reinforced plastics. 1965.
- [43] Q. Z. Xiao. Recent Developments of Hybrid Crack Element: Determination of Its Complete Displacement Field and Combination with XFEM. *III European Conference on Computational Mechanics*, 2008. URL <http://www.simulia.com/download/rum11/UK/Advanced-XFEM-Analysis.pdf>.
- [44] Haohui Xin and Milan Veljkovic. Fatigue crack initiation prediction using phantom nodes-based extended finite element method for S355 and S690 steel grades. *Engineering Fracture Mechanics*, 214: 164 – 176, 2019. ISSN 0013-7944. doi: <https://doi.org/10.1016/j.engfracmech.2019.04.026>. URL <http://www.sciencedirect.com/science/article/pii/S0013794419300177>.
- [45] Zhen zhong Du. eXtended Finite Element Method (XFEM) in Abaqus. *Dassault Systèmes Simulia Corp.* URL <http://www.simulia.com/download/rum11/UK/Advanced-XFEM-Analysis.pdf>.



# A

## Appendix A - Subroutine DFlux

```
SUBROUTINE DFLUX (FLUX, SOL, KSTEP, KINC, TIME, NOEL, NPT, COORDS,  
1 JLTYP, TEMP, PRESS, SNAME)  
C  
C INCLUDE 'ABA_PARAM.INC'  
C  
DIMENSION FLUX(2), TIME(2), COORDS(3)  
CHARACTER*80 SNAME  
  
PARAMETER (ZERO=0.D0, ONE=1.D0, TWO=2.D0, FOUR=4.D0, PI=3.1415926D0,  
1 THREE=3.D0)  
  
IF (TIME(2) .LE. 40.001 .AND. TIME(2) .GE. 0.001) THEN  
Rv = 10  
RU = 26  
RI = 600  
REta = 0.95  
RQ = 1000*REta*RU*RI  
Ra = 6.9  
Rb = 9.1  
RFb = 1.4  
RFf = 0.6  
Rc1 = 6.9  
Rc2 = 16  
RK = 3.0  
RL = 3.0  
RM = 3.0  
x0 = 0  
y0 = 0  
z0 = 0 - Rv*(TIME(2)-0.001)  
Rbeta = -38*PI/180  
XX = COORDS(1)  
YY = COORDS(2)  
ZZ = COORDS(3)  
RX = abs((XX-x0)*cos(Rbeta)+(YY-y0)*sin(Rbeta))  
RY = abs(-(XX-x0)*sin(Rbeta)+(YY-y0)*cos(Rbeta))  
RZ = abs(ZZ-z0)  
  
IF (ZZ-z0 .GE. ZERO) THEN  
!back
```

```

RQXY1 = -RK*RX**2.0/Ra**2.0-RL*RY**2.0/Rb**2.0-RM*RZ**2.0/Rc2**2.0
FLUX(1) =6.0*sqrt(3.0)*RFb*RQ*Exp(RQXY1)/Ra/Rb/Rc2/PI/Sqrt(PI)
ENDIF

IF (ZZ-z0 .LT. ZERO) THEN
!front
RQXY2 = -RK*RX**2.0/Ra**2.0-RL*RY**2.0/Rb**2.0-RM*RZ**2.0/Rc1**2.0
FLUX(1) = 6.0*sqrt(3.0)*RFf*RQ*Exp(RQXY2)/Ra/Rb/Rc1/PI/Sqrt(PI)
ENDIF
ELSEIF (TIME(2) .LE. 180.001 .AND. TIME(2) .GT. 140.001) THEN
Rv = 10
RU = 26
RI = 600
REta = 0.95
RQ = 1000*REta*RU*RI
Ra = 6.9
Rb = 9.1
RFb = 1.4
RFf = 0.6
Rc1 = 6.9
Rc2 = 16
RK = 3.0
RL = 3.0
RM = 3.0
x0 = -306.166779
y0 = 0
z0 = -400 + Rv*(TIME(2)-140.001)
Rbeta = -38*PI/180
XX = COORDS(1)
YY = COORDS(2)
ZZ = COORDS(3)
RX = abs((XX-x0)*cos(Rbeta)+(YY-y0)*sin(Rbeta))
RY = abs(-(XX-x0)*sin(Rbeta)+(YY-y0)*cos(Rbeta))
RZ = abs(ZZ-z0)

IF (ZZ-z0 .GE. ZERO) THEN
!back
RQXY1 = -RK*RX**2.0/Ra**2.0-RL*RY**2.0/Rb**2.0-RM*RZ**2.0/Rc2**2.0
FLUX(1) = 6.0*sqrt(3.0)*RFb*RQ*Exp(RQXY1)/Ra/Rb/Rc2/PI/Sqrt(PI)
ENDIF

IF (ZZ-z0 .LT. ZERO) THEN
!front
RQXY2 = -RK*RX**2.0/Ra**2.0-RL*RY**2.0/Rb**2.0-RM*RZ**2.0/Rc1**2.0
FLUX(1) = 6.0*sqrt(3.0)*RFf*RQ*Exp(RQXY2)/Ra/Rb/Rc1/PI/Sqrt(PI)
ENDIF
ELSE
FLUX(1) = 0
ENDIF
RETURN
END

```

# B

## Appendix B - Sequence birth and death principle

K.Spyridoni					N. van den Berg							
Thermal analysis		Mechanical analysis			Thermal analysis		Mechanical analysis		Predefined field (Mechanical)			
Weld element	Step	Time	Step	Time	Weld element	Step	Time	Step	Time	Step	Begin increment	End increment
Weld_total	Model Change	0.001	Model Change	0.001	Weld_total	Model Change	0.001	Model Change	0.001	Model Change	-	-
Weld1	Step2	1	Step2	1	Weld1	Step2	1	Step2	1	Step3	0	0
Weld2	Step3	1	Step3	1	Weld2	Step3	1	Step3	1	Step4	0	0
Weld3	Step4	1	Step4	1	Weld3	Step4	1	Step4	1	Step5	0	0
...	...	...	...	...	...	...	...	...	...	...	...	...
Weld37	Step38	1	Step38	1	Weld37	Step38	1	Step38	1	Step39	0	0
Weld38	Step39	1	Step39	1	Weld38	Step39	1	Step39	1	Step40	0	0
Weld39	Step40	1	Step40	1	Weld39	Step40	1	Step40	1	Step41	0	0
Weld40	Step41	1	Step41	1	Weld40	Step41	1	Step41	100	First cooling	0	0
First cooling	First cooling	100	First cooling	100	First cooling	First cooling	100	First cooling	1	Step 42	0	0
Weld41	Step 42	1	Step 42	1	Weld41	Step 42	1	Step 42	1	Step 43	0	0
Weld42	Step 43	1	Step 43	1	Weld42	Step 43	1	Step 43	1	Step 44	0	0
Weld43	Step 44	1	Step 44	1	Weld43	Step 44	1	Step 44	1	Step 45	0	0
...	...	...	...	...	...	...	...	...	...	...	...	...
Weld77	Step 78	1	Step 78	1	Weld77	Step 78	1	Step 78	1	Step 79	0	0
Weld78	Step 79	1	Step 79	1	Weld78	Step 79	1	Step 79	1	Step 80	0	0
Weld79	Step 80	1	Step 80	1	Weld79	Step 80	1	Step 80	1	Step 81	0	0
Weld80	Step 81	1	Step 81	1	Weld80	Step 81	1	Step 81	4000	Second cooling	37(Last 0 increment)	
Second cooling	Second Cooling	4000	Second Cooling	4000	Second cooling	Second Cooling	4000					

# C

## Appendix C - transversal DLOAD-subroutine

```
      SUBROUTINE DLOAD(F, KSTEP, KINC, TIME, NOEL, NPT, LAYER, KSPT,  
1COORDS, JLYP, SNAME)  
C  
      INCLUDE 'ABA_PARAM.INC'  
C  
      DIMENSION TIME(2), COORDS(3)  
      CHARACTER*80 SNAME  
C  
C  
C  
C define the load values  
C unit: m, N  
      rP0=0  
      rLoadA=80000/2!N  
      rLoadB=125000/2!N  
      rLoadC=90000/2!N  
C  
C the shape of local wheel  
      rwidthA=220!mm  
      rwidthB=540!mm  
      rwidthC=270!mm  
      rlength=320!mm  
C  
C initial position of the local wheel  
      rx0=-1000!mm  
      ry0=0  
      rz0=3890!mm  
C  
      raxle1=2000!mm  
      raxle2=3800!mm  
      raxle3=5600!mm  
      raxle4=1300!mm  
      rPwheelA=rLoadA/(rwidthA*rlength)  
      rPwheelB=rLoadB/(rwidthB*rlength)  
      rPwheelC=rLoadC/(rwidthC*rlength)
```

```

C
C define the moving speed
  rspeedx=50mm/s
  !rspeedy=0
  rspeedz=0mm/s
  rPositionx0=rx0-rspeedx
  !rPositiony0=ry0-rspeedy
  rPositionz0=rz0-rspeedz
C
C define the moving speed
  rDispx=TIME(1)*rspeedx
  !rDispy=TIME(1)*rspeedy
  rDispz=TIME(1)*rspeedz
C
  rxMinA=rDispx-0.5*rwidthA+rPositionx0
  rxMaxA=rDispx+0.5*rwidthA+rPositionx0

  rxMinB=rDispx-0.5*rwidthB+rPositionx0
  rxMaxB=rDispx+0.5*rwidthB+rPositionx0

  rxMinC=rDispx-0.5*rwidthC+rPositionx0
  rxMaxC=rDispx+0.5*rwidthC+rPositionx0

  rzMin1=rDispz-0.5*rlength+rPositionz0
  rzMax1=rDispz+0.5*rlength+rPositionz0

C define the moving load region , one local wheel loading
C
C axle 1 wheel 1 (Axle type A)
  IF ((COORDS(1)+0.5*raxle1) .ge. rxMinA .and.
    1((COORDS(1)+0.5*raxle1)
    1.lt. rxMaxA) .and.
    2 (COORDS(3).ge.rzMin1) .and. (COORDS(3).lt.rzMax1)) THEN
    F=rP0+rPwheelA
C axle 1 wheel 2
  ELSE IF ((COORDS(1)-0.5*raxle1) .ge. rxMinA) .and. (COORDS(1)
    1-0.5*raxle1
    1.lt. rxMaxA) .and.
    2 (COORDS(3).ge.rzMin1) .and. (COORDS(3).lt.rzMax1)) THEN
    F=rP0+rPwheelA
C
C
C
C axle 2 wheel 1 (Axle type B)
  ELSE IF ((COORDS(1)+0.5*raxle1) .ge. rxMinB) .and. (COORDS(1)
    1+0.5*raxle1
    1.lt. rxMaxB) .and.
    2 (COORDS(3)+raxle2.ge.rzMin1) .and. (COORDS(3)+raxle2.lt.rzMax1))
    3THEN
    F=rP0+rPwheelB
C axle 2 wheel 2

```

```

ELSE IF ((COORDS(1)-0.5*raxle1 .ge.rxMinB) .and. (COORDS(1)
1-0.5*raxle1
1.lt.rxMaxB) .and.
2 (COORDS(3)+raxle2 .ge.rzMin1).and. (COORDS(3)+raxle2.lt.rzMax1))
3THEN
    F=rP0+rPwheelB
C
C
C
C axle 3 wheel 1 (Axle type C)
    ELSE IF ((COORDS(1)+0.5*raxle1 .ge.rxMinC) .and. (COORDS(1)
1+0.5*raxle1
1.lt.rxMaxC) .and.
2 (COORDS(3)+raxle2+raxle3 .ge.rzMin1) .and. (COORDS(3)+raxle2+raxle3 .lt. rzMax1))
3THEN
    F=rP0+rPwheelC
C axle 3 wheel 2
    ELSE IF ((COORDS(1)-0.5*raxle1 .ge.rxMinC) .and.
1(COORDS(1)-0.5*raxle1
1.lt.rxMaxC) .and.
2 (COORDS(3)+raxle2+raxle3.ge.rzMin1) .and. (COORDS(3)+raxle2+raxle3 .lt. rzMax1))
3THEN
    F=rP0+rPwheelC
C
C
C
C axle 4 wheel 1 (Axle type C)
    ELSE IF ((COORDS(1)+0.5*raxle1 .ge.rxMinC) .and.
1(COORDS(1)+0.5* raxle1
1.lt.rxMaxC) .and.
2 (COORDS(3)+raxle2+raxle3+raxle4.ge.rzMin1) .and. (COORDS(3)+raxle2+
3raxle3+raxle4 .lt. rzMax1))
4THEN
    F=rP0+rPwheelC
C axle 4 wheel 2
    ELSE IF ((COORDS(1)-0.5*raxle1 .ge.rxMinC) .and.
1(COORDS(1)-0.5* raxle1
1.lt.rxMaxC) .and.
2 (COORDS(3)+raxle2+raxle3+raxle4.ge.rzMin1) .and. (COORDS(3)+raxle2+
3raxle3+raxle4 .lt. rzMax1))
4THEN
    F=rP0+rPwheelC
C
C
C
C
C axle 5 wheel 1 (Axle type C)
    ELSE IF ((COORDS(1)+0.5*raxle1 .ge.rxMinC) .and.
1(COORDS(1)+0.5* raxle1
1.lt.rxMaxC) .and.
2 (COORDS(3)+raxle2+raxle3+raxle4+raxle4.ge.rzMin1) .and. (COORDS(3)+raxle2+
3raxle3+raxle4+raxle4 .lt. rzMax1))
4THEN
    F=rP0+rPwheelC
C axle 5 wheel 2
    ELSE IF ((COORDS(1)-0.5*raxle1 .ge.rxMinC) .and.

```

```
1 (COORDS(1) - 0.5 * raxle1
1 .lt. rxMaxC) .and.
2 (COORDS(3) + raxle2 + raxle3 + 2 * raxle4 .ge. rzMin1) .and. (COORDS(3) + raxle2 +
3 raxle3 + 2 * raxle4 .lt. rzMax1))
4 THEN
    F = rP0 + rPwheelC

    ELSE
    F = 0
    END IF

    RETURN
    END
```